

**Top quark measurements and calibration of the Soft
Muon Tagger using the ATLAS detector at the Large
Hadron Collider.**

Jacobo Ezequiel Blanco

Department of Physics
Royal Holloway, University of London



A thesis submitted for the degree of Doctor of Philosophy

August 10, 2014

DECLARATION

I confirm that the work presented in this thesis is my own. Where information has been derived from other sources, I confirm that this has been indicated in the document. Jacobo Ezequiel Blanco

Abstract

This is an abstract

Acknowledgements

As it turns out, a doctoral thesis is the culmination of a few dozen people supporting and guiding a single person to the finish line. Here I name a few of my fellow backers. Firstly, I would like to thank my supervisor Dr. Veronique Boisvert for her support and guidance during tought times. To my fellow PhD students, Dr. Dan Hayden, Dr. Neil Cooper-Smith, Dr. Liam Duguid, Dr. Rob and Dr. Tim Brooks for their ROOT, C++ knowledge and most of all for making the office a wonderful place to be. To the other members of the ATLAS group who have at one time or another given me sage advice over the years and for your interest in me and my work, thank you for making me feel like a part of the team. A massive thank you must go to my brothers, sisters-in-law and nephews for all of their help, support and personal guidance during tough, emotional times and their positive, loud nature during happy times. Para mis padres, no hay palabras para describir la magnitud del apoyo que me habeis dado. No hubiera podido hacer nada sin ustedes, desde el fondo the mi corazon, los quiero mucho. Sin duda tengo los mejores padres que un hijo pudiera pedir. Last but not least, I want to thank my wonderful partner Ashton “booface” Turnbull for believing in me event when I did not believe in myself. Not a single page of this thesis could exist without you. Thank you.

Preface

This thesis describes various top measurements performed using a novel method, referred to as *soft muon tagging* (SMT), for identifying the decay of b -quarks by tagging the muons produced from the semileptonic decay of these quarks. The implementation of soft muon tagging used here relies on the quality of the match between tracks in the inner detector and muon systems of the ATLAS detector. In addition, the calibration of this methodology is also described here. Chapter 2 includes an introductory overview of the Standard Model of Particle physics. Chapter ?? includes a more detailed description of top quark physics, including the production mechanisms and decay modes; the experimental signature of top events at hadron colliders; and some of the latest results in the field of top quark measurements. Chapter ?? includes: a description of the ATLAS detector and all its components relevant to the study of the top quark, including the inner detector and muon systems; a short introduction to particle physics event simulation; and object reconstruction techniques used at ATLAS including the SMT tagger. The measurement of the data/simulation SMT efficiency scale-factor on 2012 ATLAS data is detailed in Chapter 5. The measurement of the top quark pair production cross-section using the SMT tagger was performed and is detailed in Chapter 6. Chapter 7 includes a feasibility study measuring the potential performance of the SMT tagger in the search for theoretical particles that produce pairs of top quarks with very high momentum.

The calibration presented in Chapter 5 is based on a standard method for calibration widely used in the ATLAS collaboration. The object selection used are based on a previous calibration performed by a former member of the RHUL top quark group. This selection was however adapted to work with 2012 ATLAS data and completely reimplemented by me using up-to-date software tools and a different type of data-sample. All results, plots and/or diagrams presented are my own unless otherwise noted. The cross-section measurement presented in Chapter 6

is the result of the joint RHUL-QMUL work group and includes contributions from current and past members of the group. The multijet background estimation in the electron channel using data-driven techniques was contributed by me and is described in more detail in Section 6.3.1. Finally, Chapter 7 includes a comparison between the SMT tagger and a lepton identification technique known as mini-isolation. This technique was devised and developed by other members of the ATLAS collaboration, however the performance measurement presented here are my own work. Once again all results, plots or diagrams in this chapter are my own unless stated otherwise.

Contents

1	Introduction and motivation	17
2	The Standard Model of Particle Physics	20
2.1	Quantum Electrodynamics	23
2.2	Quantum Chromodynamics	24
2.3	Weak Interactions	26
2.3.1	Electroweak Unification and the Englert-Brout-Higgs mechanism	30
3	Top-quark physics	33
3.1	Top quark production	34
3.2	Top quark decay modes	36
3.3	Latest developments in top physics	40
4	The LHC and the ATLAS Detector	45
4.1	The Large Hadron Collider	45
4.1.1	Pileup	48
4.2	The ATLAS detector	49
4.2.1	Inner Detector	51
4.2.2	Calorimetry	55
4.2.3	Muon spectrometer	59
4.2.4	Magnet system	62
4.2.5	Beam-pipe	64
4.2.6	Triggering and DAQ	64
4.3	Monte Carlo Simulation	65

4.3.1	Event Generation	65
4.3.2	Detector simulation	67
4.4	Object reconstruction	67
4.4.1	Electron reconstruction	68
4.4.2	Muon reconstruction	69
4.4.3	Jet Reconstruction	70
4.4.4	<i>b</i> -jet tagging techniques	72
5	Calibration of the Soft Muon Tagger	77
5.1	Tag and Probe Selection	78
5.1.1	Trigger requirements	79
5.1.2	Selection Cuts	80
5.2	Invariant mass fitting	82
5.2.1	Uncertainty Measurement	85
5.3	Efficiencies	86
5.3.1	2011 Calibration	86
5.3.2	Efficiency Binning	88
5.4	Results	88
5.5	Scale Factor Discrepancy	103
5.5.1	Future developments	106
6	Measurement of the $t\bar{t}$ cross-section	110
6.1	Data and Monte Carlo samples	110
6.2	Object selection and event selection	111
6.3	Background estimation	113
6.3.1	Multijet in the electron channel	115
6.3.2	Multijet background in the muon channel	122
6.3.3	$W+jets$ background	124
6.3.4	Background Shapes	125
6.4	Systematic uncertainties	128
6.5	Results and conclusion	128

7 Muon identification in a boosted $t\bar{t}$ environment	132
7.1 Data samples	133
7.2 Boosted event topology	134
7.3 Signal muon selection	137
7.4 Efficiency definition	138
7.5 Results	142
7.5.1 Background	145
7.6 B-tagging potential in boosted events	146
8 Conclusions	150
Appendices	151
A Electron identification criteria	152
B Muon identification criteria	154
C STACO Combined Covariance Matrix	155
D List of triggers used in calibration	156
E List of muon combined performance (MCP) cuts	159
F STACO CB reconstruction efficiency	160

List of Figures

2.1	The interaction vertex described by QED.	23
2.2	LO feynman diagrams of the process $e^+e^- \rightarrow e^+e^-$ allowed in QED. Additional vertices can be added to produce higher-order diagrams of the same process.	24
2.3	Diagrams of the fundamental interaction vertices described by quantum chromodynamics. Shown are (a) Gluon emission from a quark, (b) Gluon emission from a gluon and finally (c) the four-gluon vertex.	26
2.4	Diagrams of neutral current and charged current vertices described by the weak force. Where $f = e, \mu, \tau$ and ν_ℓ is the corresponding lepton neutrino of the same flavour.	26
2.5	Neutral current weak scattering vertex.	27
3.1	The leading order Feynman diagrams for $t\bar{t}$ production.	35
3.2	Example Feynman diagrams for single top quark at leading order.	36
3.3	Branching ratios of all possible $t\bar{t}$ decays. These probabilities are based on the branching ratios of W boson decay shown in Table 3.2.	38
3.4	Example event display of a dilepton $t\bar{t}$ event recorded by ATLAS.	39
3.5	The Feynman diagram of lepton plus jets channel including $t\bar{t}$ production via gluon fusion and decay with a leptonically decaying W^+ . Note that all other production mechanisms are also considered and the final state where the W^- is decayed leptonically is also taken into account.	39

3.6 A summary of all $t\bar{t}$ production cross section measurements performed at the LHC at $\sqrt{s} = 7$ TeV. The theory prediction shown as a dotted black line associated uncertainties as grey bands. The results shown above the black line have been statistically combined, producing the results labelled as combined . Many of these analyses have been superseded and the results are shown below the line. Other analyses performed but not included in the combination are also shown below the line, such as the analysis described in Chapter 6.	41
3.7 A summary of all $t\bar{t}$ production cross section measurements performed at the LHC at $\sqrt{s} = 8$ TeV. The theory prediction is shown as a dotted line with associated uncertainties as grey bands.	42
3.8 A summary of the most precise $t\bar{t}$ production cross section measurements performed at the LHC at $\sqrt{s} = 7$ and 8 TeV and the Tevatron at $\sqrt{s} = 1.96$ TeV compared to the theoretical prediction. The Tevatron results should be compared against the prediction for $p\bar{p}$ collisions while the LHC against the pp collision predictions.	43
3.9 Summary of all m_t measurement results per analysis at ATLAS. The statistical combination of these results are compared to the combination from Tevatron.	44
4.1 The layout of CERN complex of experiments, note the main four LHC experiments located at different points around the ring.	46
4.2 Shown in (a) is the number of bunches colliding at the LHC and (b) the peak luminosity per unit time.	47
4.3 Distribution of the total integrated luminosity delivered by the LHC and the recorded by ATLAS for the 2011 and 2012 pp collision period. Note the \sqrt{s} changing from 7 TeV to 8 TeV between 2011 and 2012 [1].	49
4.4 Number of interactions per bunch for the 2012 pp data-taking period at ATLAS per day. Both the average number of interactions for all bunches and the maximum number of interactions are shown [1].	50
4.5 An overview diagram of the ATLAS experiment. Shown are all detection and tracking systems and the toroid magnet which encompasses them. Note also the muon system on the outside of the detector.	51

4.6	Drawing of the ATLAS inner detector	52
4.7	An event-display of an event as reconstructed by the ATLAS inner detector. Shown are the results of the vertexing algorithm where each line represents a track. the purple tracks have been fitted to a secondary vertex.	53
4.9	A cut-away diagram of the ATLAS detector highlighting the calorimetry system. Shown are the ECal barrel and end-cap, the HCal barrel and end-cap and the FCal end-cap [2].	56
4.10	Cut-away diagram of the EM calorimeter barrel at $\eta = 0$. Shown are the three different layers with varying cell structures. The strip section is designed to enhance particle identification and position measurement in η	58
4.11	Cut-away drawing of the ATLAS muon system.	60
4.12	Plan view of quarter-section of the ATLAS muon spectrometer.	62
4.13	Transverse view of the muon system. Shown are the	62
4.14	Diagram of the ATLAS toroid magnet system. The red central solenoid is located closest to the beam surrounded by layers of tile calorimetry. The eight barrel toroid magnets are shown along with the offset end-cap toroids at each end.	63
4.15	Sketch of a proton-proton collision as modelled by the event generator [3]. Shown are the incoming protons beams as green arrows on the left and right sides of the diagram. The partons shown in blue, interact in the hard interaction (red blob) producing a parton shower, also depicted in red, which eventually hadronize (light green blobs) and finally decay into final state particles shown in dark green. The <i>underlying event</i> is shown at the bottom of the diagram as the purple blob, note also the beam remnants as light blue blobs that also form part of the underlying event. Photon emission is shown in yellow and occurs at all stages of the event generation.	66
4.16	Light jet rejection as a function of the b -jet tagging efficiency, comparing some of taggers used at ATLAS as measured in simulated $t\bar{t}$ events [4].	73
4.17	Feynman diagram of one of the mechanisms for lepton production via semileptonic b decay. Shown are the direct $b \rightarrow \mu$ and indirect $b \rightarrow c \rightarrow \mu$	75

5.1	The distribution of χ^2_{DoF} for all muon probes for ATLAS collision data (solid dots) and prompt J/ψ Monte Carlo simulation (solid line). Note that the collision data distribution includes sources of background.	82
5.2	A drawing of the various components of the fit procedure. The composite fit is shown along with the corresponding implied signal and background. The two variations of the background shape are also shown, these are exaggerated for illustration purposes.	83
5.3	Diagrams of crystal ball distributions. Modified from [5].	84
5.4	Invariant mass distributions of tag and probe pairs at a) probe, b) muon probe and c) SMT level in collision data for probes in barrel A with a p_T of 5 to 6 GeV. Note the components of the fit, the variations on the background and the 3σ and 5σ integration windows used for systematics. Fit parameters are shown with uncertainties.	87
5.5	Distribution of STACO CB reconstruction efficiencies and scale factor in side A of the detector for all detector regions.	90
5.6	Distribution of STACO CB reconstruction efficiencies and scale factor in side C of the detector for all detector regions.	91
5.7	Distribution of the χ^2_{match} efficiencies and scale factor with respect to the (a) azimuthal angle ϕ and (b) the pseudorapidity η of the muon probe passing the SMT requirements.	92
5.8	Distribution of the χ^2_{match} efficiencies and scale factor with respect to the transverse momentum of the muon probe passing the SMT requirements.	94
5.9	χ^2_{match} efficiencies and scale factors in the crack region of the detector for side (a) A and (b) C.	95
5.10	χ^2_{match} efficiencies and scale factors in the barrel region of the detector for side (a) A and (b) C.	96
5.11	χ^2_{match} efficiencies and scale factors in the transition region of the detector for side (a) A and (b) C.	97
5.12	χ^2_{match} efficiencies and scale factors in the endcap region of the detector for side (a) A and (b) C.	98

5.13	χ^2_{match} efficiencies and scale factors in the forward region of the detector for side (a) A and (b) C.	99
5.14	χ^2_{Dof} efficiencies and scale factor with respect to $\sum E_T$ for a muon probe that passes the SMT requirements.	100
5.15	χ^2_{Dof} efficiencies and scale factor with respect to $\sum p_T$ for a muon probe that passes the SMT requirements.	101
5.16	χ^2_{Dof} efficiencies and scale factor with respect to N_{tracks} for a muon probe that passes the SMT requirements.	102
5.17	Distribution of the χ^2_{match} efficiencies and scale factor with respect to impact parameter d_0 for muon probes with p_T in the ranges (a) 4 to 6 GeV, (b) 6 to 8 GeV and (c) 8 to 10 GeV. The measurement was carried out only on Period B of 2012 ATLAS collision data.	104
5.18	Distribution of pull (see 5.11) of components of χ^2_{Dof} as measured in the ID for muon probes in the barrel region for collision data (squares) and prompt J/ψ simulation (dotted). Shown are (a) θ , (b) ϕ , (c) d_0 , (d) z_0 and (e) q/p . These distributions are based on smaller samples and are normalized to unit area.	105
5.19	Distribution of χ^2_{Dof} of STACO CB muons from $Z \rightarrow \mu\mu$ with ideal detector alignment (dot-dashed), $Z \rightarrow \mu\mu$ with smeared alignment (solid), $J/\psi \rightarrow \mu\mu$ with smeared alignment at $\sqrt{s} = 8$ TeV (dotted) and $J/\psi \rightarrow \mu\mu$ with smeared at $\sqrt{s} = 7$ TeV as used in the 2011 analysis (dot-dashed). Distributions are normalized to unit area.	107
5.20	Distribution of the momentum imbalance of STACO CB muons from $Z \rightarrow \mu\mu$ with ideal detector alignment (double dot-dashed), $Z \rightarrow \mu\mu$ with smeared alignment (solid), $J/\psi \rightarrow \mu\mu$ with smeared alignment at $\sqrt{s} = 8$ TeV (dotted) and $J/\psi \rightarrow \mu\mu$ with smeared at $\sqrt{s} = 7$ TeV as used in the 2011 analysis (dot-dashed). Distributions are normalized to unit area.	109
6.1	Feynman diagrams of some $V + \text{jets}$ and diboson background processes to $t\bar{t}$ in the $\ell + \text{jets}$ channel.	114
6.2	Feynman diagrams of some single-top and multijet background processes to $t\bar{t}$ in the $\ell + \text{jets}$ channel.	115

6.3	A diagram of the E_T^{miss} -isolation phase space. Shown are the four regions as defined by the event selection.	117
6.4	Kinematic distributions in region B (high- E_T^{miss} + non-isolated electron) at pre-tag and tag level. These distributions are obtained by subtracting non-multijet contributions using simulation.	120
6.5	Distributions for tagged events in the $e+\text{jets}$ (left) and $\mu+\text{jets}$ (right) channels of, from top to bottom, lepton p_T , transverse W mass and missing transverse energy [6].	126
6.6	Distributions of SMT variables in the $e+\text{jets}$ (left) and $\mu+\text{jets}$ (right) of, from top to bottom, SMT muon p_T and SMT muon χ_{DoF}^2 [6].	127
7.1	Diagrams of the possible configurations of final-state objects in a (a) boosted and (b) non-boosted events.	135
7.2	The angular separation (ΔR) between the truth W muon and the corresponding b -quark for all examined Z' mass points and non-resonant $t\bar{t}$	135
7.3	The transverse momentum of the top/anti-top quarks in the event for all examined Z' mass points and non-resonant $t\bar{t}$	136
7.4	The angular separation (ΔR) between the b and \bar{b} in the event for all examined Z' mass points and non-resonant $t\bar{t}$	136
7.5	Distributions for all tested Z' mass points of (a) the transverse momentum and (b) pseudorapidity of muons which pass the χ_{match}^2 tagger selection, the (c) angular separation between those muons and the nearest jet in the event, and (d) the χ_{match}^2 used in the selection. All distributions normalized to unit area.	139
7.6	Distributions for all tested Z' mass points of (a) the transverse momentum and (b) pseudorapidity of muons which pass the MI10 selection, the (c) angular separation between those muons and the nearest jet in the event, and (d) the cone size used in the selection. All distributions normalized to unit area.	140
7.7	Structure of the efficiency measurement including both cutflows.	141

7.8	Efficiency of MI ($k_T = 10$) and χ_{match}^2 tagger as a function of the angular separation between the reconstructed muon and the nearest reconstructed jet. The dip in the MI efficiency at low ΔR is removed in the nominal analysis by cutting at $\Delta R < 0.1$	144
7.9	Efficiency of mini-isolation ($k_T = 10$) and the χ_{match}^2 muon tagger as a function of the transverse momentum of the muon.	144
7.10	149

List of Tables

2.1	A summary of all elementary particles described by the SM [7]. Note the various groupings and divisions including by spin, generation and particle type. For each particle the charge (q), mass and name are shown as per the legend on the bottom-right.	22
2.2	A summary of the four fundamental forces ordered by relative strength. These are approximate relative strengths for the purpose of demonstrating the hierarchy of forces as a function of their strength. A more accurate determination of the interaction strength depends on the details of the interaction itself. Note however the order-of-magnitude differences in the relative strengths of these forces. Note that the graviton is the theoretical boson responsible for mediating gravitational interactions, it is not part of the SM.	23
3.1	Summary of the predicted SM single top production [8] and top pair production [9] cross sections at the LHC for $\sqrt{s} = 7$ and 8 TeV.	36
3.2	Branching ratios for the decay of W boson. Here “Hadrons” refers to all possible combinations of $q\bar{q}'$ where \bar{q}' denotes the antiquark of a flavour different to that of the first quark [7].	37
4.1	Design energy resolution of all ATLAS calorimeter components. The resolution is made of a sampling term ($1/\sqrt{E}$) associated with the choice of passive and active materials and the construction of the layers, and a constant term associated with the depth of the detector, cracks and dead material.	57
4.2	Main parameters of the muon system [2].	61

4.3	Summary of spatial and temporal resolutions per chamber for all chamber types used in the ATLAS muon spectrometer. Adapted from [2].	63
4.4	Branching ratio for the production of a muon from a b -quark in both direct and indirect modes [7].	75
5.1	Tag selection criteria.	80
5.2	Pairing criteria.	81
5.3	SMT criteria.	81
5.4	Data/MC Scale Factors for 2011 Data in all five regions of the detector as a function of p_T . The uncertainties include systematic and statistical components as described in [10].	88
5.5	Pseudorapidity regions of the ATLAS detector.	89
5.6	Data/MC Scale Factors for 2012 Data in all five regions of the detector as a function of p_T . The uncertainties include systematic and statistical components as described in Section 5.2.1.	93
5.7	Summary of χ^2_{match} tagger efficiencies as measured in all tested samples	106
5.8	Summary of momentum imbalance efficiencies as measured in all tested samples	108
6.1	List of branching ratios as used in HERWIG and PYTHIA generators compared to the reference PDG values [7].	111
6.2	Summary of contamination in all control regions at pretag level. The contamination here is shown out of the total number of events in data. The uncertainties shown include statistical and systematic contributions.	118
6.3	Summary of contamination in all control regions at tagged level. The contamination here is shown out of the total number of events in data. The uncertainties shown include statistical and systematic contributions.	119
6.4	Multijet SMT event tagging-rate in regions A) inverted- E_T^{miss} , non-isolated, B) High- E_T^{miss} , non-isolated and C) low- E_T^{miss} , isolated.	121
6.5	Multijet estimates in the $e+jets$ channel. The uncertainties are combined statistical and systematics. A systematic uncertainty of 50 % is used on the matrix method pretag event yields in addition to the uncertainties obtained on the tagging rate.	122

6.6	Multijet estimates obtained using the ABCD method. The uncertainty contains statistical and systematic components.	123
6.7	Summary of tagging-rates as measured in data in the two multijet-dominated regions. The uncertainty quoted includes statistical and systematic contributions. The uncertainty on the unweighted average is set as half of the difference between control regions [6].	124
6.8	Summary of the $W + \text{jets}$ background estimates for the electron and muon channels [6].	125
6.9	List of cross-section uncertainty sources for the three-jets inclusive selection [6].	129
6.10	Event yields for signal and background events, as well as the yield measured in data [6].	130
6.11	Summary of event selection efficiencies for the muon, electron and combined channels as measured on the signal $t\bar{t}$ sample [6].	130
7.1	Results of constructing the muon sample used to estimate the efficiency of the χ^2_{match} tagger. Uncertainty is statistical only.	142
7.2	Results of constructing the muon sample used to estimate the efficiency of mini-isolation. Uncertainty is statistical only.	143
7.3	Efficiency of selecting a muon by using the χ^2_{match} tagger against MI, including the additional acceptance provided by the χ^2_{match} tagger. Uncertainty is statistical only.	145
7.4	Fake rate of χ^2_{match} tagger, mini-isolation and mini-isolation including overlap removal as measured using all Z' mass points.	146
7.5	Summary of b -quark to jet matching efficiencies for all tested Z' masses. The sample for $m_{Z'} = 2500 \text{ GeV}$ contains a smaller integrated luminosity, than the other samples, hence the lower number of jets.	147
7.6	Results of the muon to jet association in MC simulated inclusive Z' samples. .	148
7.7	Summary of the jet tagging results. The values represent the tagged jets out of the pool of jets matched to b -quarks.	148

7.8 Summary of the jet tagging efficiencies. The amount of overlap is shown out of the SMT tagged jets. The added acceptance is the additional number of jets added by using SMT plus MV1 over MV1 only. The uncertainties are statistical only.	149
A.2 caption	153

¹ Chapter 1

² Introduction and motivation

³ The Large Hadron Collider or LHC, is the most powerful collider in the world and gives scien-
⁴ tists a probe to study the universe at an unprecedented energy level. The ATLAS experiment
⁵ is a general-purpose detector serviced by the LHC designed to record and measure every as-
⁶ pect of the outgoing spray of particles resulting from the colliding LHC beams. High energy
⁷ research can be divided into several categories: testing the established theory known as the
⁸ Standard Model of particle (SM), improvement of previously measured parameters and the
⁹ search for new physics. The SM has stood the test of time and rigorous experimental testing.
¹⁰ A crucial part of the theory, the Higgs mechanism, was experimentally validated in 2012 when
¹¹ the ATLAS and CMS experiments independently confirmed the production of Higgs boson in
¹² LHC collisions.

¹³ Top quark physics concerns itself with the study of the heaviest known quark described by
¹⁴ the SM. Due to its large mass the top quark does not bind to other quarks to form a composite
¹⁵ particle known as a hadron. The top is the only quark that can therefore be studied directly
¹⁶ on its own. In addition, the mass of the top quark is a parameter the SM and many Beyond the
¹⁷ Standard Model (BSM) theories.

¹⁸ Due to the large center of mass energy at the LHC, top quarks are produced in large quan-
¹⁹ tities allowing for detailed studies of many top quark properties. Top quarks can be produced
²⁰ either in single-top events or, more likely at the LHC, into a pair with one top and one antitop
²¹ ($t\bar{t}$ pair). The top quark decays overwhelmingly into a W boson and a b -quark. Subsequently
²² the W can decay leptonically, into a lepton and lepton neutrino; or hadronically, into a pair

23 of quarks. Top quark pair events are classified into three groups depending on the manner in
24 which the W bosons decay: “all-hadronic”, where both W bosons decay hadronically; “dilep-
25 ton”, where both bosons decay into leptons; and finally, “lepton plus jets” where one boson
26 decays leptonically and the other hadronically.

27 The b -quark binds with other quarks to form hadrons. This hadron then decays into a col-
28 limated shower of particles known as a jet. Identification of these b -jets is an important part
29 of any top quark analysis and there are several methods of b -tagging in use. The soft muon
30 tagger (SMT tagger), with which this thesis concerns itself, is one such b -tagger. b -hadrons
31 can decay so as to produce a low momentum muon (also known as a soft muon) which then
32 emerges buried within the subsequent jet. The SMT tagger uses the quality of the reconstruc-
33 tion of so-called combined muons, which rely on both inner detector and muon spectrometer
34 information for reconstruction. The quality of the matching between the inner detector and
35 muon spectrometer tracks is encapsulated in the χ^2 of the match. Muon reconstruction and
36 the SMT tagger are described in more detail in Section 4.4.4.

37 Measurement of the top quark pair production probability, denoted by the cross-section
38 $\sigma_{t\bar{t}}$, is an important early measurement to make. In particular as the cross-section depends
39 on the center of mass energy of the collision, such a measurement tests the predictive power of
40 the Standard Model at an energy level never studied before. Any new physics processes which
41 share the same signature as $t\bar{t}$ production will result in an excess in the cross-section above
42 the theoretically measured value.

43 An example of new physics include theories that posit the existence of a very heavy boson
44 known as the Z' . This boson would preferentially decay to a $t\bar{t}$ pair where each top quark has
45 a large amount of momentum.

46 In this thesis the SMT tagger is calibrated and used as part of a cross-section measurement
47 and its performance is evaluated in searching for high momentum tops emerging from Z'
48 decays. Measuring the top quark pair production cross-section using the SMT tagger is of
49 interest as it tests a different aspect of theory, namely the description of semileptonic b -decays,
50 compared to lifetime-based taggers. Such a measurement was carried out and is detailed in
51 Chapter 6.

52 Other soft muon tagging techniques exist, these however depend on the presence of a jet
53 in the event to work. The SMT tagger, in its χ^2_{match} form, only relies on the presence of a muon

54 to measure its performance. The calibration of the tagger on 2012 ATLAS data is presented in
55 Chapter 5.

56 In addition, this means that the tagger can be used to identify muons emerging from the
57 W rather than from semileptonic b -decays. The performance of such a technique is studied in
58 Chapter 7 where the tagger is tested in two ways. Firstly, the tagger is used to identify the muon
59 emerging from the W boson decay. Its performance is compared to the nominal approach, as
60 well as a novel method specifically designed for boosted top searches known as mini-isolation.
61 Secondly, the tagger is used to identify the b -jets in the event and its performance in this regime
62 is compared to the standard MV1 tagger.

⁶³ **Chapter 2**

⁶⁴ **The Standard Model of Particle**
⁶⁵ **Physics**

⁶⁶ Particle physics, or high-energy physics, is the study of the fundamental constituents of matter and their interactions. The best current description of these interactions is known as The Standard Model of Particle Physics (SM); a group of theories that cover all currently known particles and their interactions. The SM was developed through-out the latter half of the 20th century and has stood the test of time and rigorous examination by numerous experiments.

⁷¹ Additionally, many of its parameters have been measured with great precision e.g. the electron magnetic moment g is known to 10^{-13} [11]. The last piece to be confirmed was the existence of the Higgs boson, which in turn points to the existence of the so-called Higgs field. Evidence of the elusive Higgs was observed by the ATLAS and CMS experiments at CERN [12,13]. Despite its tremendous success, the SM cannot account and explain for all observed phenomenon in the universe. Firstly, the theory requires many of its parameters to be measured empirically. The theory does not a priori provide a value for these parameters such as the number of particle generations. Additionally, the theory does not describe the most familiar of the forces, gravity. Furthermore, the SM does not provide a candidate for dark matter or dark energy, which according to recent measurements accounts for more than 90 % of the total energy density in the universe [14]. The asymmetry between matter and antimatter is also not fully explained by the SM.

⁸³ As such there is a strong focus on developing theories which go beyond the standard model

84 (BSM) to provide an answer to these open questions. The discussion in this chapter is largely
85 based on [15] and [16].

86 The SM describes the nature of the interactions of the fundamental constituents of our
87 universe in terms of the three different fundamental forces: strong, weak and electromagnetic
88 (EM), each described by a specific theory. As mentioned before, the most familiar of the forces,
89 gravity, is not described by the SM. The SM classifies particles into several categories depend-
90 ing on their properties and allowed interactions. Particles which have a half-integer spins (e.g.
91 $S = \frac{1}{2}, \frac{3}{2}, \dots$) are known as *fermions*, these are the basic constituents of matter. Particles with
92 integer spins (e.g. $S = 0, 1, \dots$) are known as *bosons*, these mediate interactions between
93 fermions and other bosons.

94 Fermions can be divided into two subgroups: quarks, which can interact via the strong,
95 weak and electromagnetic forces and leptons which can only interact by the weak and elec-
96 tromagnetic forces. There are six known leptons: electron e , muon μ and tau τ , which all
97 have electric charge¹ $Q = 1$, and the corresponding electrically neutral neutrino ν_e , ν_μ and
98 ν_τ . Analogously, six quark *flavours* are known: u , c and t , with electric charge $Q = +2/3$ and
99 d , s and b , with electric charge $Q = -1/3$.

100 Quarks and leptons are divided into three generations, which differ only by the mass and
101 flavour of their constituent fermions, each generation being heavier than the previous. A
102 summary of all elementary particles described by the SM can be found in Table 2.1.

103 For every matter fermion (f) there is an equivalent antimatter partner (\bar{f}) which possesses
104 the same characteristics as its matter companion but is opposite in electric charge. Thus 12
105 matter particles are combined with 12 antimatter partners for a total of 24 elementary particles
106 which form all visible matter in the universe.

107 The interaction between fermions occur via the exchange of spin one particles known as
108 bosons. Each force is mediated by one or more bosons (Table 2.2). The strong force is mediated
109 by a set of massless bosons known as the gluons. The weak force is mediated by a neutral
110 massive boson known as the Z boson and a pair of charged massive bosons known as the
111 W bosons. Finally, the electromagnetic force is mediated by a massless boson known as the
112 photon. Note that each boson has an antimatter partner however some are indistinguishable
113 from their matter partner. A summary of their properties is shown in Table 2.1.

¹The electric charge is always stated in units of elementary charge e

114 Each fermion has a set of so-called quantum numbers which dictate the type of interactions
 115 that can occur. For example each lepton has a lepton number associated with it, electrons have
 116 an electron lepton number (L_e) of +1, while the positron has $L_e = -1$. Muons and taus have
 117 their own respective lepton number (L_μ and L_τ). Each neutrino has lepton number $L_f = 1$ and
 118 their anti-matter counterpart have $L_f = -1$. Each of these lepton numbers is approximately
 119 conserved separately across interaction vertices. The conservation is only approximate due
 120 to the non-zero mass of neutrinos. Another example of a quantum number is baryon number
 121 (B), each quark has $B = \frac{1}{3}$ and anti-quarks have $B = -\frac{1}{3}$.

	Fermions ($s = \frac{1}{2}$)	Bosons ($s = 0$)	Higgs ($s = 1$)													
	I II III															
Quarks	<table border="1" style="width: 100%; border-collapse: collapse;"> <tr> <td style="padding: 5px;">$+\frac{2}{3}$ u Up</td><td style="padding: 5px;">$+\frac{2}{3}$ c Charm</td><td style="padding: 5px;">$+\frac{2}{3}$ t Top</td><td></td></tr> <tr> <td></td><td></td><td></td><td style="text-align: center; padding: 5px;">0 0 MeV γ Photon (EM)</td></tr> </table> <table border="1" style="width: 100%; border-collapse: collapse;"> <tr> <td style="padding: 5px;">$-\frac{1}{3}$ d Down</td><td style="padding: 5px;">$-\frac{1}{3}$ s Strange</td><td style="padding: 5px;">$-\frac{1}{3}$ b Bottom</td><td style="text-align: center; padding: 5px;">± 1 80.4 GeV W^\pm W boson (Weak)</td></tr> </table>	$+\frac{2}{3}$ u Up	$+\frac{2}{3}$ c Charm	$+\frac{2}{3}$ t Top					0 0 MeV γ Photon (EM)	$-\frac{1}{3}$ d Down	$-\frac{1}{3}$ s Strange	$-\frac{1}{3}$ b Bottom	± 1 80.4 GeV W^\pm W boson (Weak)	<table border="1" style="width: 100%; border-collapse: collapse;"> <tr> <td style="padding: 5px;">0 H^0 Higgs boson</td><td></td></tr> </table>	0 H^0 Higgs boson	
$+\frac{2}{3}$ u Up	$+\frac{2}{3}$ c Charm	$+\frac{2}{3}$ t Top														
			0 0 MeV γ Photon (EM)													
$-\frac{1}{3}$ d Down	$-\frac{1}{3}$ s Strange	$-\frac{1}{3}$ b Bottom	± 1 80.4 GeV W^\pm W boson (Weak)													
0 H^0 Higgs boson																
Leptons	<table border="1" style="width: 100%; border-collapse: collapse;"> <tr> <td style="padding: 5px;">-1 e Electron</td><td style="padding: 5px;">-1 μ Muon</td><td style="padding: 5px;">-1 τ Tau</td><td style="text-align: center; padding: 5px;">0 91.2 GeV Z Z boson (Weak)</td></tr> <tr> <td></td><td></td><td></td><td style="text-align: center; padding: 5px;">0 0 MeV g Gluon (Strong)</td></tr> </table>	-1 e Electron	-1 μ Muon	-1 τ Tau	0 91.2 GeV Z Z boson (Weak)				0 0 MeV g Gluon (Strong)	<table border="1" style="width: 100%; border-collapse: collapse;"> <tr> <td style="padding: 5px;">0 ν_e Electron Neutrino</td><td style="padding: 5px;">0 ν_μ Muon Neutrino</td><td style="padding: 5px;">0 ν_τ Tau Neutrino</td><td style="text-align: center; padding: 5px;">q mass symbol name (force)</td></tr> </table>	0 ν_e Electron Neutrino	0 ν_μ Muon Neutrino	0 ν_τ Tau Neutrino	q mass symbol name (force)		
-1 e Electron	-1 μ Muon	-1 τ Tau	0 91.2 GeV Z Z boson (Weak)													
			0 0 MeV g Gluon (Strong)													
0 ν_e Electron Neutrino	0 ν_μ Muon Neutrino	0 ν_τ Tau Neutrino	q mass symbol name (force)													

Table 2.1: A summary of all elementary particles described by the SM [7]. Note the various groupings and divisions including by spin, generation and particle type. For each particle the charge (q), mass and name are shown as per the legend on the bottom-right.

Name	Relative Strength	Boson
Strong	10^{38}	Gluons
Electromagnetic	10^{36}	Photon
Weak	10^{25}	W^\pm and Z^0
Gravity	1	Graviton*

Table 2.2: A summary of the four fundamental forces ordered by relative strength. These are approximate relative strengths for the purpose of demonstrating the hierarchy of forces as a function of their strength. A more accurate determination of the interaction strength depends on the details of the interaction itself. Note however the order-of-magnitude differences in the relative strengths of these forces. Note that the graviton is the theoretical boson responsible for mediating gravitational interactions, it is not part of the SM.

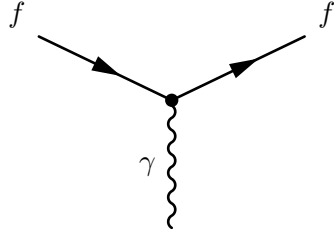


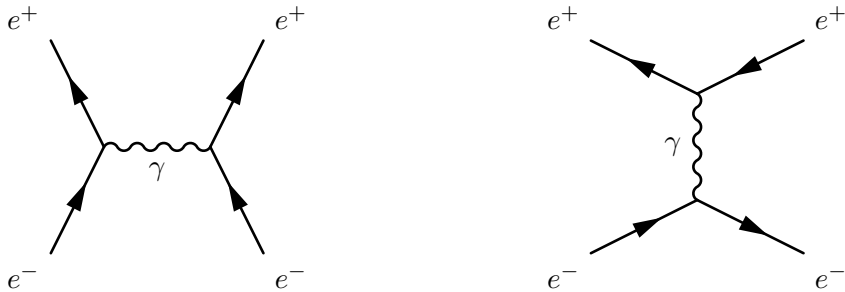
Figure 2.1: The interaction vertex described by QED.

122 2.1 Quantum Electrodynamics

123 The interaction of particles via the electromagnetic force is described by Quantum Electrodynamics or QED. These interactions are mediated by the massless neutral boson known as the 124 photon and the strength of the interaction is characterized by the fine-structure constant α . All 125 electrically charged fermions are allowed to interact, since the photon itself is not charged, no 126 self-interaction is allowed within QED. Figure 2.1 shows the single vertex described by QED, 127 where two fermions interact via a photon. Note that the electric charge is conserved across 128 the vertex, so for example $\gamma \rightarrow e^+e^-$ is not allowed within QED.
129

130 By combining different forms of this vertex one can build every possible QED interaction.
131 The interaction $e^+e^- \rightarrow e^+e^-$ is known as Bhabha scattering. Two leading order (LO)² dia-
132 grams contribute to this interaction, annihilation (Figure 2.2a) and scattering (Figure 2.2b).

²The simplest diagram with the least vertices



(a) Electron-positron pair annihilation mediated by a photon.
 (b) Electron-positron pair scattering mediated via the emission of a photon.

Figure 2.2: LO Feynman diagrams of the process $e^+e^- \rightarrow e^+e^-$ allowed in QED. Additional vertices can be added to produce higher-order diagrams of the same process.

¹³³ 2.2 Quantum Chromodynamics

¹³⁴ Interactions via the strong force are described in the theory of Quantum Chromodynamics
¹³⁵ (QCD). These interactions are mediated by a set of massless neutral bosons known as gluons.
¹³⁶ QCD introduces the concept of colour, which similarly to electrical charge, determines the
¹³⁷ possible interactions that can occur via the strong force. Colour can take three states, red
¹³⁸ (antired), blue (antiblue), green (antigreen):

$$r = \begin{pmatrix} 1 \\ 0 \\ 0 \end{pmatrix}, \quad g = \begin{pmatrix} 0 \\ 1 \\ 0 \end{pmatrix}, \quad b = \begin{pmatrix} 0 \\ 0 \\ 1 \end{pmatrix} \quad (2.1)$$

$$\bar{r} = \begin{pmatrix} 1 & 0 & 0 \end{pmatrix}, \quad \bar{g} = \begin{pmatrix} 0 & 1 & 0 \end{pmatrix}, \quad \bar{b} = \begin{pmatrix} 0 & 0 & 1 \end{pmatrix} \quad (2.2)$$

¹³⁹ Both quarks and gluons possess colour and as a result gluons, unlike photons, can self-
¹⁴⁰ interact in a three gluon vertex (Figure 2.3b) or a four gluon vertex (Figure 2.3c). As with
¹⁴¹ electrical charge, colour-charge must also be conserved. Thus in the scattering process $q \rightarrow q +$
¹⁴² g shown in Figure 2.3a the flavour of the quark may not change but the colour-charge does and
¹⁴³ the gluon carries away the difference in colour. Thus each gluon has a colour-anticolour charge
¹⁴⁴ associated with it. Naively one would expect nine different types of gluon that participate in
¹⁴⁵ interaction, owing to the nine possible combinations of colour and anticolour, however the

¹⁴⁶ SU(3) symmetry on which QCD is based results in a colour octet:

$$\begin{array}{ll}
 (r\bar{b} + b\bar{r})/\sqrt{2} & -i(r\bar{g} - g\bar{r})/\sqrt{2} \\
 -i(r\bar{b} - b\bar{r})/\sqrt{2} & (b\bar{g} + g\bar{b})/\sqrt{2} \\
 (r\bar{r} + b\bar{b})/\sqrt{2} & -i(b\bar{g} - g\bar{b})/\sqrt{2} \\
 (r\bar{g} + g\bar{r})/\sqrt{2} & (r\bar{r} + b\bar{b} - 2g\bar{g})/\sqrt{6}
 \end{array} \tag{2.3}$$

¹⁴⁷ and a “colour singlet”:

$$(r\bar{r} + g\bar{g} + b\bar{b})/\sqrt{3} \tag{2.4}$$

¹⁴⁸ which is overall colourless.

¹⁴⁹ There are then eight different gluons that can participate in QCD interactions each with
¹⁵⁰ a different colour-charge combination. Additionally there is a ninth combination which is
¹⁵¹ overall colourless so it cannot take part in interactions.

¹⁵² In an analogous fashion to screening which occurs with electric charges, quark-antiquark
¹⁵³ pairs act like dipoles which screen the true colour charge of the central quark. However since
¹⁵⁴ gluons also carry colour, they cause the opposite effect (anti-screening) to amplify and change
¹⁵⁵ the observed colour of the quark. Which effect wins out depends on the number of colours in
¹⁵⁶ the theory and the number of quark flavours. As it is with three colour states and six different
¹⁵⁷ quark flavours, anti-screening is the overall dominant effect. As a result the colour potential
¹⁵⁸ decreases with distance and quarks experience very little potential when very near to each
¹⁵⁹ other. This effect is known as asymptotic freedom and results in quarks only existing within
¹⁶⁰ colourless bound states known as *hadrons*.

¹⁶¹ Hadrons can be divided into two categories: *mesons*, which contain a quark and an anti-
¹⁶² quark ($q\bar{q}$); and *baryons* which are made of three quarks (or antiquarks) each with a different
¹⁶³ (anti)colour-charge to result in a colourless composite particle. Common examples of baryons
¹⁶⁴ are protons (uud) and neutrons (udd) which are the building blocks of atomic nuclei. While
¹⁶⁵ π^0 ($u\bar{u}/d\bar{d}$) is a commonly produced meson in hadron colliders. Note that due to the quark
¹⁶⁶ configuration, baryons have baryon number $B = +1$ while mesons have $B = 0$.

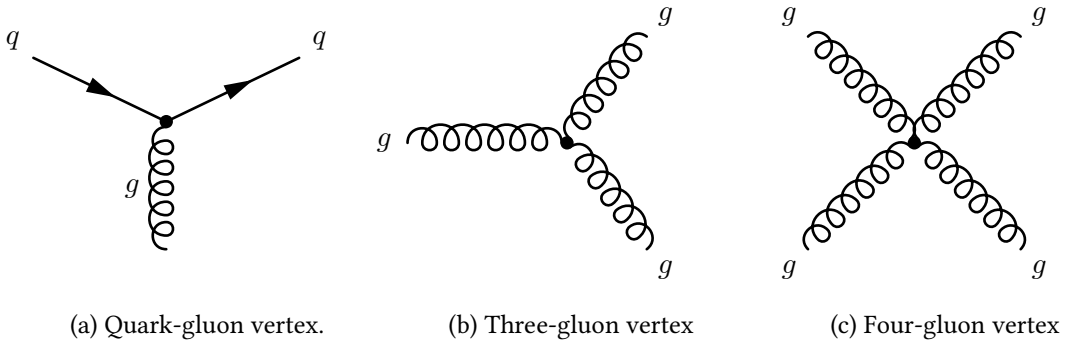


Figure 2.3: Diagrams of the fundamental interaction vertices described by quantum chromodynamics. Shown are (a) Gluon emission from a quark, (b) Gluon emission from a gluon and finally (c) the four-gluon vertex.

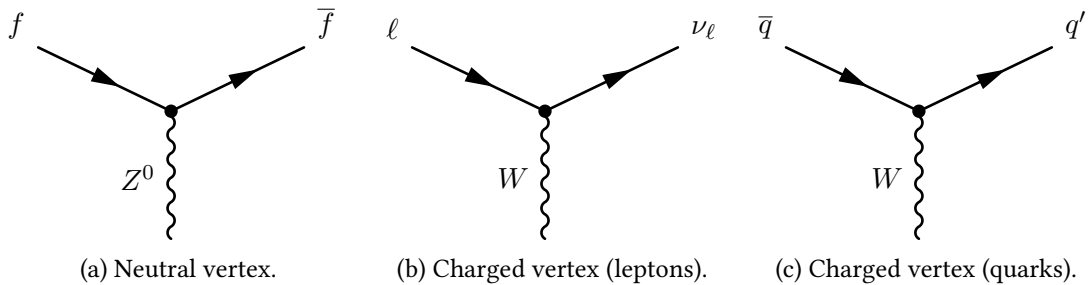


Figure 2.4: Diagrams of neutral current and charged current vertices described by the weak force. Where $f = e, \mu, \tau$ and ν_ℓ is the corresponding lepton neutrino of the same flavour.

¹⁶⁷ 2.3 Weak Interactions

¹⁶⁸ The final type of interaction involves the so-called weak force. The weak force is responsible
¹⁶⁹ for β^- decay ($n \rightarrow p + e^- + \bar{\nu}_e$) and β^+ decay. Interactions via the weak force are mediated by
¹⁷⁰ a single neutral massive boson and two charged massive bosons. Since the bosons responsible
¹⁷¹ for weak interactions are massive, the range of interaction is very short, unlike electromagnetic
¹⁷² interactions via a massless photon.

¹⁷³ All fermions can take part in interactions via the weak force. Let us consider weak interac-
¹⁷⁴ tions involving only leptons. The weak neutral vertex is very similar to the basic vertex seen
¹⁷⁵ in QED (Figure 2.1). A valid interaction via the weak force is then formed by combining these
¹⁷⁶ simple vertices (Figure 2.4) while taking care to conserve electric charge and lepton flavour.
¹⁷⁷ An example of a leptonic weak interaction is muon decay ($\mu \rightarrow \nu_\mu e^- \bar{\nu}_e$) shown in Figure 2.5.

¹⁷⁸ Let us consider weak interactions involving quarks. The neutral vertex is similar to that of
¹⁷⁹ the leptonic version, a quark can emit a Z boson or a Z can decay to a quark-antiquark pair.

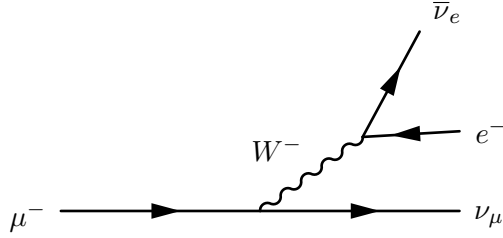


Figure 2.5: Neutral current weak scattering vertex.

180 The charged current then changes the flavour of an up-type quark into a down-type quark
 181 (or vice-versa) with a W boson of the appropriate charge (Figure 2.4c). Weak interactions
 182 can also change the flavour of a quark across generations. A well-known example of such an
 183 interaction is Kaon decay ($K^+ \rightarrow \mu^+ \nu_\mu$). In order to account for this interaction and preserve
 184 the universality of weak interactions, Nicola Cabibbo postulated [17] that the states that couple
 185 to the charged current are really a mixture of 'rotated' quark states:

$$\begin{pmatrix} u \\ d' \end{pmatrix} \begin{pmatrix} c \\ s' \end{pmatrix} \quad (2.5)$$

186 where

$$d' = d \cos \theta_c + s \sin \theta_c \quad (2.6a)$$

187

$$s' = -d \sin \theta_c + s \cos \theta_c \quad (2.6b)$$

188 This introduces an arbitrary parameter into the theory known as the quark mixing angle
 189 or the Cabibbo angle θ_c . The introduction of quark mixing has the effect of attenuating the
 190 interaction strength at vertices involving multiple quark generations. Interactions which cross
 191 one generation are said to be Cabibbo Suppressed while those that cross two generations are
 192 Doubly Cabibbo suppressed.

193 Taking into account the three quark generations, quark mixing can be expressed in matrix
 194 notation as shown in Equation 2.7. This unitary matrix is known as the Cabibbo-Kobayashi-
 195 Maskawa matrix (CKM matrix) after Cabibbo which initially postulated quark mixing and
 196 Makoto Kobayashi and Toshihide Maskawa who later added an additional generation, con-

¹⁹⁷ taining the top and bottom quarks, to the matrix [18].

$$\begin{pmatrix} d' \\ s' \\ b' \end{pmatrix} = V_{CKM} \begin{pmatrix} d \\ s \\ b \end{pmatrix} = \begin{pmatrix} V_{ud} & V_{us} & V_{ub} \\ V_{cd} & V_{cs} & V_{cb} \\ V_{td} & V_{ts} & V_{tb} \end{pmatrix} \begin{pmatrix} d \\ s \\ b \end{pmatrix} \quad (2.7)$$

¹⁹⁸ Several parametrizations of the CKM matrix exist, the Chau-Keung parametrization [19]
¹⁹⁹ uses angles θ_{12} , θ_{23} , θ_{13} and a phase δ_{13} :

$$V_{CKM} = \begin{pmatrix} c_{12}c_{13} & s_{12}c_{13} & s_{13}\exp(-i\delta) \\ -s_{12}c_{23} - c_{12}s_{23}s_{13}\exp(i\delta) & c_{12}c_{23} - s_{12}s_{23}s_{13}\exp(i\delta) & s_{23}c_{13} \\ s_{12}s_{23} - c_{12}c_{23}s_{13}\exp(i\delta) & -c_{12}s_{23} - s_{12}c_{23}s_{13}\exp(i\delta) & c_{23}c_{13} \end{pmatrix} \quad (2.8)$$

²⁰⁰ where $c_{ij} = \cos \theta_{ij}$ and $s_{ij} = \sin \theta_{ij}$ for $i = 1, 2, 3$. This parametrization has the advantage that
²⁰¹ each angle θ_{ij} relates to a specific transition from one generation to the other. If $\theta_{13} = \theta_{23} = 0$
²⁰² the third generation is not coupled to the other two and the matrix reduces to the original
²⁰³ matrix postulated by Cabibbo. Note that θ_{12} is the Cabibbo angle, θ_c , described earlier.

²⁰⁴ Another parametrization due to Wolfenstein [20] expresses all elements in terms of the
²⁰⁵ Cabibbo angle by defining $\lambda \equiv s_{12} = \sin \theta_{12}$ and then expressing the other elements in terms
²⁰⁶ of powers of λ

$$V_{CKM} \approx \begin{pmatrix} 1 - \lambda^2/2 & \lambda & A\lambda^3(\rho - i\eta) \\ -\lambda & 1 - \lambda^2/2 & A\lambda^2 \\ A\lambda^3(1 - \rho - i\eta) & -A\lambda^2 & 1 \end{pmatrix} \quad (2.9)$$

²⁰⁷ where A , ρ and η are all real numbers intended to express the order of magnitude differences
²⁰⁸ between s_{12} and the other elements in the matrix. Of course, all the elements should be the
²⁰⁹ same irrespective of which parametrization is used.

²¹⁰ The elements of the CKM matrix have been measured and the latest accepted results are
²¹¹ summarized in 2.11 [7]. The interaction strength is then proportional to $|V_{ij}|^2$. The unitarity

212 of the CKM matrix implies that the probability of transition from any up-type quark to any
213 down-type is the same,

$$\sum_k |V_{ik}|^2 = \sum_i |V_{ik}|^2 = 1 \quad (2.10)$$

214 for all i quark generations [21]. The term V_{tb} is approximately unity and by far dominates
215 over the other V_{tj} terms. This means that the top-quark transitions almost exclusively into a
216 b -quark ($t \rightarrow Wb$) with transitions $t \rightarrow Ws$ and $t \rightarrow Wd$ having a probability of less than 1%.
217 The soft muon tagger which is the focus of this thesis relies on weak semileptonic decays of
218 b -quarks. From 2.11 one can see that the transition $b \rightarrow c$ dominates over $b \rightarrow u$. Additionally,
219 the focus of this thesis is on $t\bar{t}$ events in the lepton plus jets channel where one W boson
220 decays hadronically governed by V_{ij} .

$$V_{CKM} = \begin{pmatrix} 0.97427 \pm 0.00015 & 0.22534 \pm 0.00065 & 0.00351^{+0.00015}_{-0.00014} \\ 0.22520 \pm 0.00065 & 0.97344 \pm 0.00016 & 0.0412^{+0.0011}_{-0.0005} \\ 0.00867^{+0.00029}_{-0.00031} & 0.0404^{+0.0011}_{-0.0005} & 0.999146^{+0.000021}_{-0.000046} \end{pmatrix} \quad (2.11)$$

221 An additional unique feature of weak interactions is that the charge conjugation-parity
222 (CP) symmetry is violated. The operator C denotes the change of a particle by its antiparticle
223 partner and P denotes a reversal of helicity (the projection of spin onto the momentum of a par-
224 ticle). A clear violation of C and P was observed in the radioactive decay of Cobalt-60, where
225 the resulting electrons were preferentially emitted in the opposite direction of the nuclear spin
226 of the Cobalt [22]. Thus weak currents only couple to left-handed neutrinos (or right-handed
227 antineutrinos) which is a violation of parity. Additionally charge symmetry is also violated
228 since a left-handed neutrino is preferentially picked over a left-handed antineutrino. Finally
229 in 1964 CP violation was observed in the decay of neutral kaon [23].

230 Thus the probability of $\bar{a} \rightarrow \bar{b}$ is not equal to that of $a \rightarrow b$. The existence of CP vio-
231 lation has interesting consequences for the formation of the early universe. The preferential
232 production of matter over antimatter in CP violating interactions would shift the balance
233 in favour of matter resulting in a universe similar to our own. In terms of the Wolfenstein
234 parametrization of the CKM matrix, if $\eta = 0$ there is no CP violation.

²³⁵ Finally as with QCD, weak interactions couple weak bosons to each other. Thus the vertex
²³⁶ $Z \rightarrow W^- W^+$ is allowed via the weak force.

²³⁷ 2.3.1 Electroweak Unification and the Englert-Brout-Higgs mechanism

²³⁸ The unification of the electromagnetic and weak theories was first proposed by Glashow and
²³⁹ later developed by Weinberg and Salam into the electroweak theory [24–26]. The theory pos-
²⁴⁰ tulates that while at low energies the two forces are to be treated separately, at higher the
²⁴¹ two can be seen as a single force. Thus the two forces are different manifestation of the same
²⁴² “electroweak” interaction. There were several stumbling blocks to the unification of the forces.
²⁴³ Firstly, the boson which drives the electromagnetic interaction, the photon, is massless while
²⁴⁴ the weak bosons are both massive. Evidence for the massive nature of these bosons has been
²⁴⁵ established by experimental results from the UA1 experiment at CERN [27].

²⁴⁶ Thus the symmetry of the theory must be spontaneously broken in some way. A mecha-
²⁴⁷ nism for electroweak symmetry breaking (EWSB) was postulated by Higgs, Brout, Englert and
²⁴⁸ others which introduces masses to the weak bosons and posits the existence of an additional
²⁴⁹ scalar (spin $S = 0$) boson known as the Higgs boson.

²⁵⁰ Gauge Theories

²⁵¹ Gauge invariance is one of the underlying invariances which underpins the Standard Model.
²⁵² Given the so-called Dirac Lagrangian³

$$\mathcal{L} = i\hbar c\bar{\psi}\gamma^\mu\partial_\mu\psi - mc^2\bar{\psi}\psi \quad (2.12)$$

²⁵³ which describes a free particle of spin- $\frac{1}{2}$ with mass m [16]. Note that it is invariant under the
²⁵⁴ transformation

$$\psi \rightarrow e^{i\theta}\psi \quad (2.13)$$

²⁵⁵ where θ is a real number, since the adjoint $\bar{\psi} \rightarrow e^{-i\theta}\bar{\psi}$ and the two terms cancel out. This is
²⁵⁶ known as a (*global*) gauge transformation since θ is the same at all points of space-time. A (*local*)

³A Lagrangian is a mathematical function that describes the underlying dynamics of a system as a function of time and space coordinates (x^μ) and their time derivatives.

257 *gauge transformation* occurs when the phase is different for different points in space-time

$$\psi \rightarrow e^{i\theta(x)}\psi \quad (2.14)$$

258 The Dirac Lagrangian (Equation 2.12) is not invariant under a local gauge transformation
 259 since extra terms are created by the derivative. This then implies that the underlying physics of
 260 such a theory depends on position in space-time. Thus local gauge invariance must be imposed.
 261 In the case of the Dirac Lagrangian, this is done by introducing additional terms to the Dirac
 262 Lagrangian which will cancel the extra terms introduced by the local gauge transformation.
 263 As it turns out this results in the introduction of a new massless vector field that couples to ψ .

264 The new Lagrangian then describes a spin- $\frac{1}{2}$ particle with mass m that interacts with a
 265 free massless field. This new field can be identified as the electromagnetic field and the spin- $\frac{1}{2}$
 266 particles are electrons and positrons. Thus the resulting Lagrangian describes all interactions
 267 that form part of quantum electrodynamics.

268 A similar procedure can be applied to the colour quark model and obtain a description of
 269 all QCD interactions. However requiring that the weak theory be a gauge theory (invariant
 270 under local gauge transformation) encounters a problem since the weak bosons are known to
 271 be massive. There must be some mechanism via which the W^\pm and Z^0 obtain mass.

272 The Englert-Bourt-Higgs mechanism

273 The Englert-Bourt-Higgs (EBH) mechanism posits the existence of a complex scalar field dou-
 274 blet that when introduced into the electroweak Lagrangian results in the weak fields acquiring
 275 a mass term. In other words the W^\pm and Z^0 interact with the Higgs field and obtain a mass.
 276 An additional consequence of introducing the Higgs field is the inclusion of a scalar boson
 277 particle, the so-called “Higgs boson”. Finally the Higgs field also couples to fermions via the
 278 Yukawa coupling generating gauge invariant mass terms for the fermions as well.⁴

279 The SM Lagrangian in its current form including the Higgs potential is shown in Equa-
 280 tion 2.15. This expression describes all possible particle interactions that form part of the SM,
 281 of particular interest are the fermion mass term which couples the fermion field (ψ) to the
 282 scalar Higgs field (ϕ) and the Higgs kinetic and potential terms.

⁴For a more complete description of the mathematical procedure see [16].

$$\begin{aligned}
 \mathcal{L} = & -\underbrace{\frac{1}{4}W_{\mu\nu}^a W^{\mu\nu a}}_{\text{Weak Field}} - \underbrace{\frac{1}{4}B_{\mu\nu} B^{\mu\nu}}_{\text{EM Field}} - \underbrace{\frac{1}{4}G_{\mu\nu}^a G^{\mu\nu a}}_{\text{Strong Field}} \\
 & + \underbrace{\bar{\psi} \not{D}_\mu \psi}_{\text{Fermion Kinetic}} + \underbrace{\lambda \bar{\psi} \psi \phi}_{\text{Fermion Mass}} \\
 & + \underbrace{|D_\mu \phi|^2}_{\text{Higgs Kinetic}} - \underbrace{V(\phi)}_{\text{Higgs Potential}}
 \end{aligned} \tag{2.15}$$

283 **Chapter 3**

284 **Top-quark physics**

285 The third generation of quarks was first proposed by Kobayashi and Maskawa in a paper pub-
286 lished in 1973 [18] as a way to explain the CP violation observed in Kaon decays. The existence
287 of the third generation was confirmed when the lighter of the two constituents, the b -quark,
288 was discovered in 1977 [28].

289 Due to its large mass, direct confirmation of the existence of the top quark required the
290 construction of very powerful accelerators. The top quark was discovered by the CDF and D0
291 experiments at Fermilab in 1995 [29, 30] and then observed at CERN in 2010 [31, 32].

The large mass of the top quark makes it a very interesting object of study. The current world average for the mass of the top quark, based on results from Tevatron and the LHC [7], is

$$m_t = 173.07 \pm 0.52 \text{ (stat.)} \pm 0.72 \text{ (syst.) GeV}$$

292 Due to its mass the top quark has an extremely short lifetime $\tau \approx 0.5 \times 10^{-24}$ s, too
293 short to interact via the strong force and hadronize into a bound state [33]. Instead the top
294 quark decays weakly producing a W boson and a b -quark almost exclusively. This allows
295 experimentalist to directly study the properties of a bare quark. An impossibility with the other
296 quarks which bind with other quarks to form hadrons. Measurement of top quark properties
297 (mass, charge, forward-backward asymmetry, couplings, etc...) forms a large part of high
298 energy physics research. Measurement of these properties provide rigorous tests of the SM,
299 point towards the existence of new physics or exclude some BSM theories.

300 From an experimental perspective, top quark decays can produce a very interesting sig-

301 nature which includes leptons, jets and transverse missing energy E_T^{miss} due to the escaping
 302 neutrino¹. The study of top quark decays relies on all parts of a general purpose detector such
 303 as ATLAS or CMS. In additional $t\bar{t}$ pair production constitutes a background for many other
 304 SM and BSM searches, as such understanding this process well is fundamental for almost all
 305 areas of HEP research.

306 3.1 Top quark production

307 Top quarks can be produced in two manners, single top production and $t\bar{t}$ pair production. In
 308 the SM, the dominant top quark pair production mechanism proceeds via the strong force. The
 309 production cross-section of $pp \rightarrow t\bar{t}$ depends on the mass of the top m_t , the centre-of-mass
 310 energy $s = 4E_{\text{beam}}^2$ and the fraction of the momentum taken by the partons² of the colliding
 311 protons.

312 In order to produce a $t\bar{t}$ pair the total energy carried by the interacting partons must be
 313 larger than twice the mass of the top. Let us define the effective centre of mass energy \hat{s}
 314 which reflects the true amount of energy available for interaction. Given two colliding partons,
 315 denoted i and j carrying x_i and x_j fractions of the centre of mass energy \sqrt{s} , then

$$\hat{s} = x_i \sqrt{s} x_j \sqrt{s} = x_i x_j s \quad (3.1)$$

316 assuming that both partons carry the same fraction of the total energy, i.e. $x_i \approx x_j$ then the
 317 minimum value of x required for $t\bar{t}$ production is

$$x \approx \frac{2m_t}{\sqrt{s}} \quad (3.2)$$

318 At the LHC the minimum threshold at $\sqrt{s} = 7 \text{ TeV}(14 \text{ TeV})$ is approximately 0.05(0.025).
 319 At such low values of x the fraction of proton momentum carried by the gluons is large [34]
 320 and thus gluon fusion interactions dominate. Gluon fusion processes represent 80(90)% of the
 321 total cross section, with the remainder contribution coming from quark pair annihilation. The
 322 Feynman diagrams for these interactions are shown in Figure 3.1. The theoretical inclusive

¹Neutrinos do not interact with the detector material and thus escape without being detected, missing energy is described in more detail in Chapter ??

²Constituents of the hadrons, so quarks and gluons

³²³ $t\bar{t}$ production cross section at the LHC has been calculated at next-to-next-to-leading order
³²⁴ (NNLO) to be $\sigma_{t\bar{t}} = 158^{-12.2}_{+13.5}$ pb [35] at $\sqrt{s} = 7$ TeV and at next-to-leading order (NLO)
 (246 \pm 10) pb for $\sqrt{s} = 8$ TeV.

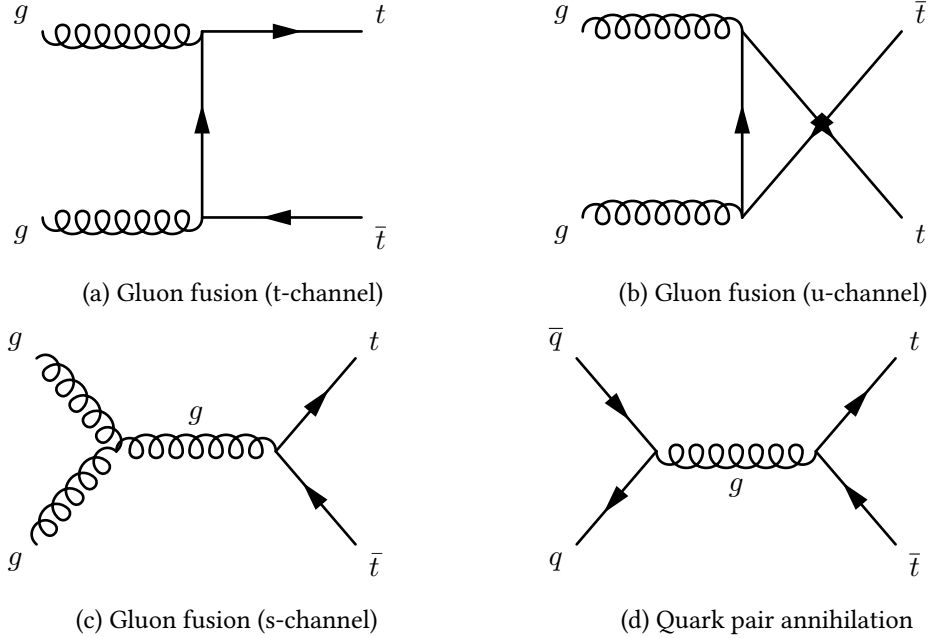


Figure 3.1: The leading order Feynman diagrams for $t\bar{t}$ production.

³²⁵
³²⁶ Single top production occurs via the weak force almost exclusively through the Wtb vertex
³²⁷ since $|V_{tb}| \gg |V_{ts}|, |V_{td}|$. At LO there are several production mechanisms for single-top events:

- ³²⁸ • Weak quark-antiquark annihilation forming a W which subsequently decays into a $t\bar{b}$
³²⁹ (Figure 3.2a).
- ³³⁰ • The so-called tW production, where a b -quark absorbs a gluon and decays to a top quark
³³¹ and W boson (Figure 3.2b).
- ³³² • b -quark scattering off a W boson, where the b comes from gluon splitting (Figure 3.2c)
³³³ or from the proton (Figure 3.2d).

³³⁴ As top quark pair production can proceed via the strong force it occurs overwhelmingly
³³⁵ more often than single top production. The inclusive cross-sections for $pp \rightarrow t\bar{t}$ and $pp \rightarrow$
³³⁶ $t + X$ at the LHC have been estimated at NLO [8, 9]. As can be seen from Table 3.1 the

³³⁷ production cross section of $t\bar{t}$ is approximately two times larger than the single-top cross-section.

Process	cross-section at [pb]	
	$\sqrt{s} = 7 \text{ TeV}$	$\sqrt{s} = 8 \text{ TeV}$
Single top $\sigma(t\text{-chan})$	66 ± 2	87 ± 3
Single top $\sigma(Wt)$	15.6 ± 1.2	22.2 ± 1.5

Table 3.1: Summary of the predicted SM single top production [8] and top pair production [9] cross sections at the LHC for $\sqrt{s} = 7$ and 8 TeV.

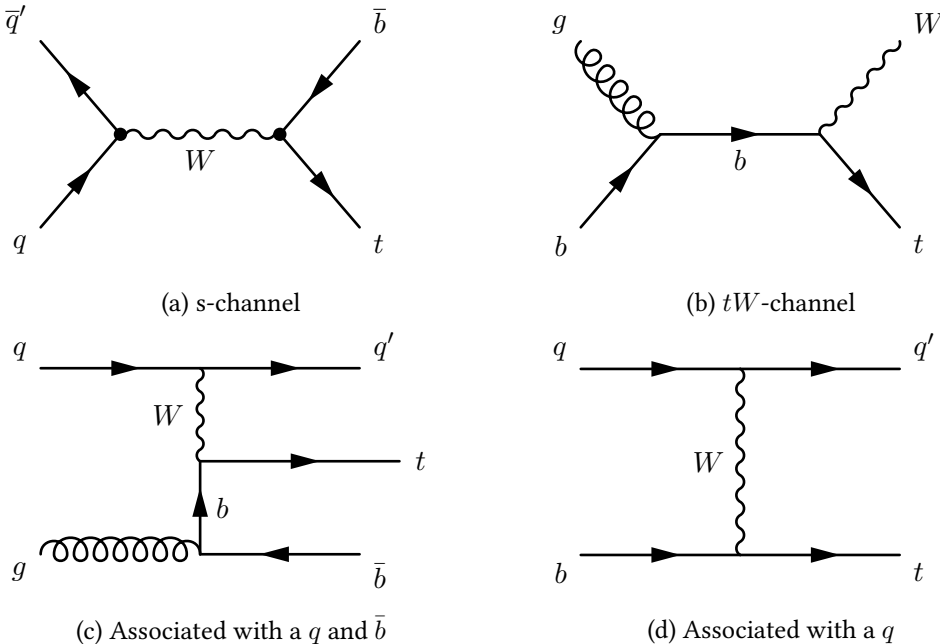


Figure 3.2: Example Feynman diagrams for single top quark at leading order.

³³⁸

3.2 Top quark decay modes

³⁴⁰ The top quark decays almost exclusively into a W boson and a b -quark. The ratio of branching
³⁴¹ ratios $\Gamma(t \rightarrow Wb)/\Gamma(t \rightarrow Wq(q = b, s, d))$ is 0.91 ± 0.04 [7].

³⁴² As the LHC collides proton-proton beams, the overwhelming majority of events produced
³⁴³ will feature multiple hadronic jets, a stream of particles resulting from the hadronization of

Decay	Branching ratio [%]
$W \rightarrow e + \nu$	10.75 ± 0.13
$W \rightarrow \mu + \nu$	10.57 ± 0.15
$W \rightarrow \tau + \nu$	11.25 ± 0.20
Hadrons	67.60 ± 0.27

Table 3.2: Branching ratios for the decay of W boson. Here “Hadrons” refers to all possible combinations of $q\bar{q}'$ where \bar{q}' denotes the antiquark of a flavour different to that of the first quark [7].

344 quarks in the detector, most of which will originate from “light” quarks³. Unlike light hadrons,
 345 b -hadrons have a sufficiently large lifetime that they travel a certain distance within a before
 346 decaying. Additional features such as the semileptonic decay of b -quarks can be exploited
 347 to determine the presence of such a quark in the detector. Collectively analysis techniques
 348 that permit the detection of b -jets are known as *b-tagging*. Top quark pairs will produce two
 349 b -quarks, making b-tagging techniques a central part of any $t\bar{t}$ analysis.

350 The other part of the top decay, the W boson is used to classify $t\bar{t}$ events. As discussed in
 351 Section ??, The W boson can decay leptonically ($\ell\nu_\ell$) or hadronically ($W \rightarrow q\bar{q}'$) driven by the
 352 CKM vertex element, since $\Gamma \propto |V_{ij}|^2$. The branching ratios of W boson decays are presented
 353 in Table 3.2.

354 Thus $t\bar{t}$ events are labelled as “dilepton”, “all-hadronic” or “lepton + jets” depending on the
 355 combination of W boson decays present. The probability for $t\bar{t}$ event to be of a given type is
 356 dependent on the branching-ratios of W boson decays shown a priori. As can be seen from
 357 Figure 3.3 the all-hadronic events dominate, followed by the lepton plus jets and dilepton. Each
 358 of these types requires a very different analysis approach due to their distinct backgrounds,
 359 branching-ratio, detector signature and reconstruction requirements.

360 The all-hadronic final state includes four light quarks which will hadronize to form four
 361 Light Flavour (LF) jets and two b -quarks leading to two b -jets. Due to the large hadronic activity
 362 the all-hadronic channel is very challenging. As mentioned before, hadronic collisions produce
 363 events with a large number of quarks - and thus jets - in the final state. The background to the
 364 all-hadronic channel are therefore very high. As shown in Figure 3.3, the all-hadronic channel

³The term light quarks usually refers to quarks in the first two generations. Light jets are those originating from those quarks

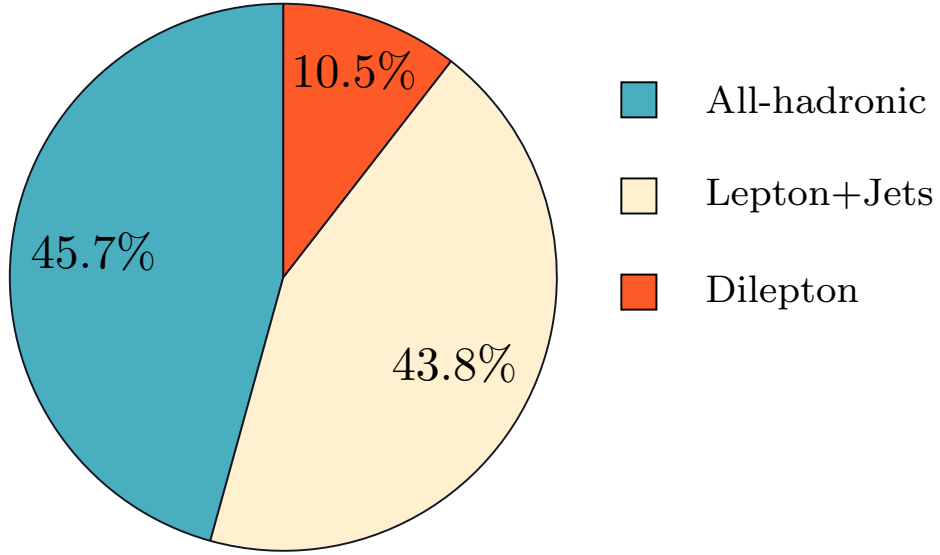


Figure 3.3: Branching ratios of all possible $t\bar{t}$ decays. These probabilities are based on the branching ratios of W boson decay shown in Table 3.2.

³⁶⁵ has the largest branching ratio of the three.

³⁶⁶ The dilepton final state includes two leptons, large E_T^{miss} from two neutrinos which escape
³⁶⁷ the detector and two b -jets. In contrast to the all-hadronic channel, dilepton events are very
³⁶⁸ clean due to the presence of leptons and E_T^{miss} , however the branching ratio is very small and
³⁶⁹ reconstruction of the top is challenging due to the presence of two neutrinos which escape the
³⁷⁰ detector without interacting.

³⁷¹ Finally, the lepton plus jets channel has a larger branching ratio than the dilepton while
³⁷² having a distinct signature with a lepton and E_T^{miss} as well as LF jets and b -jets. Lepton plus jets
³⁷³ analyses usually do not directly treat τ leptons as the signal lepton. The τ lepton is unstable and
³⁷⁴ decays primarily via the weak force producing hadrons in the final state. The reconstruction of
³⁷⁵ τ leptons is a complex task and τ plus jet events are treated separately as dedicated analyses.
³⁷⁶ An example of the full lepton plus jets chain is shown in Figure 3.5.

³⁷⁷ The lepton plus jets channel has the advantage of a more distinct signature than the all-
³⁷⁸ hadronic event as well as a suffering from less background. Additionally the branching ratio
³⁷⁹ of lepton plus jets event is approximately twice that of the dilepton channel. As a result the
³⁸⁰ lepton plus jets channel has been chosen as the focus of this thesis.

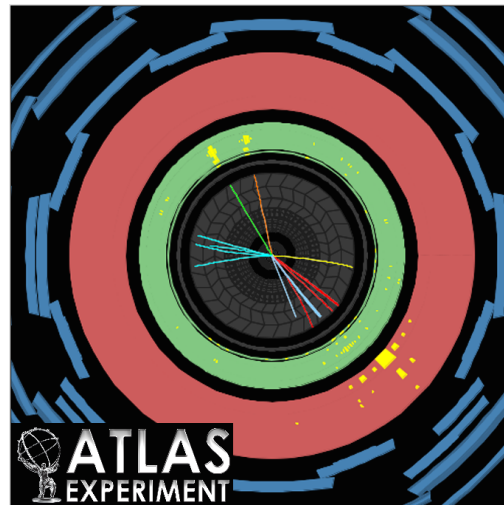


Figure 3.4: Example event display of a dilepton $t\bar{t}$ event recorded by ATLAS.

Figure 3.5: The Feynman diagram of lepton plus jets channel including $t\bar{t}$ production via gluon fusion and decay with a leptonically decaying W^+ . Note that all other production mechanisms are also considered and the final state where the W^- is decayed leptonically is also taken into account.

381 3.3 Latest developments in top physics

382 This section discusses a few of the latest measurements in the area of top quark pair production
383 with a focus on LHC results. As discussed top quark decays provide the only probe to study
384 the properties of a bare quark. Measurements of its properties provide a stringent test of
385 the SM and could show hints of new physics from BSM theories. Moreover, due to its final
386 state signature, top quark pair production, particularly in the lepton plus jets channel, form
387 the background to many searches for new physics. Additionally all parts of the detector are
388 utilized in the reconstruction of $\ell + \text{jets}$ events and as such it is possible to use these events to
389 tune or *calibrate* many analysis and reconstruction techniques.

390 Cross-section measurement

391 Measurement of the cross-section of the top quark is a benchmark test of the SM. Any statisti-
392 cally significant deviation from the predicted value could point to the presence of new physics.
393 Some BSM theories posit the existence of particles which could decay to produce a $t\bar{t}$ pair. If
394 such theory is correct this would be observed in an increase in the cross section measured
395 away from the predicted SM value.

396 Experimentally measurement of the cross-section is vital when attempting to reduce and
397 estimate the amount of top quark background present in other analyses. Searches for the
398 Higgs boson exploit many different channels such as $t\bar{t}H \rightarrow t\bar{t}b\bar{b}$ which have $t\bar{t}$ events as a
399 background. The type of events predicted by the BSM theory, Supersymmetry (SUSY) include
400 a large amount of E_T^{miss} , leptons and jets in the final state. Top quark pair events mimic these
401 processes and constitute a large background.

402 A summary of all $t\bar{t}$ cross section measurements from the LHC at $\sqrt{s} = 7 \text{ TeV}$ is shown in
403 Figure 3.6 and a comparison against the Tevatron measurement at $\sqrt{s} = 1.96 \text{ TeV}$ is shown in
404 Figure 3.8. Early results at $\sqrt{s} = 8 \text{ TeV}$ are shown in Figure 3.7.

405 Top mass measurement

The mass of the top m_t is a fundamental parameter of the SM. Measurements of the top mass
have been carried out in all $t\bar{t}$ channels at both ATLAS and CMS [36]. These results are sum-

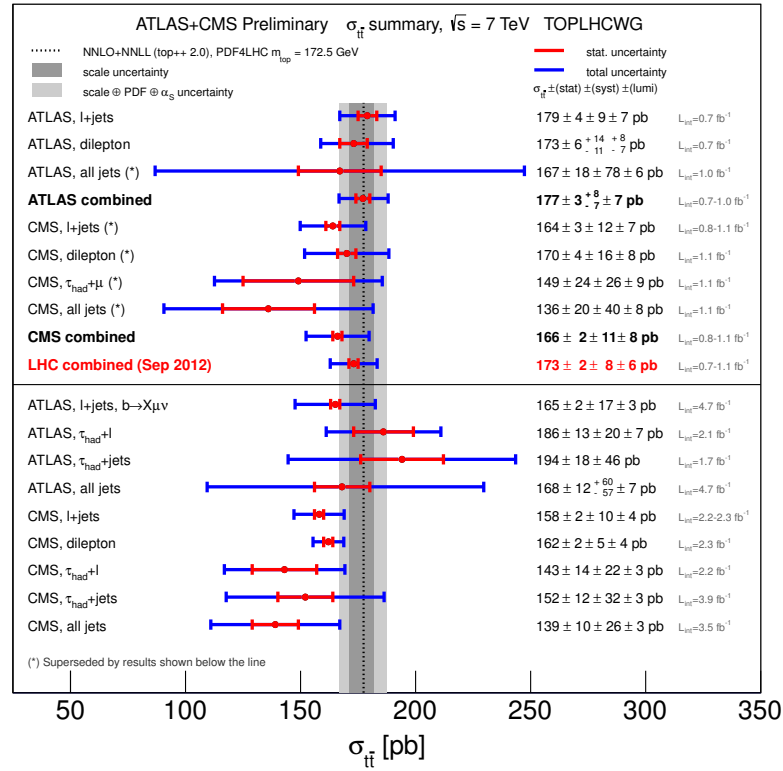


Figure 3.6: A summary of all $t\bar{t}$ production cross section measurements performed at the LHC at $\sqrt{s} = 7 \text{ TeV}$. The theory prediction shown as a dotted black line associated uncertainties as grey bands. The results shown above the black line have been statistically combined, producing the results labelled as **combined**. Many of these analyses have been superseded and the results are shown below the line. Other analyses performed but not included in the combination are also shown below the line, such as the analysis described in Chapter 6.

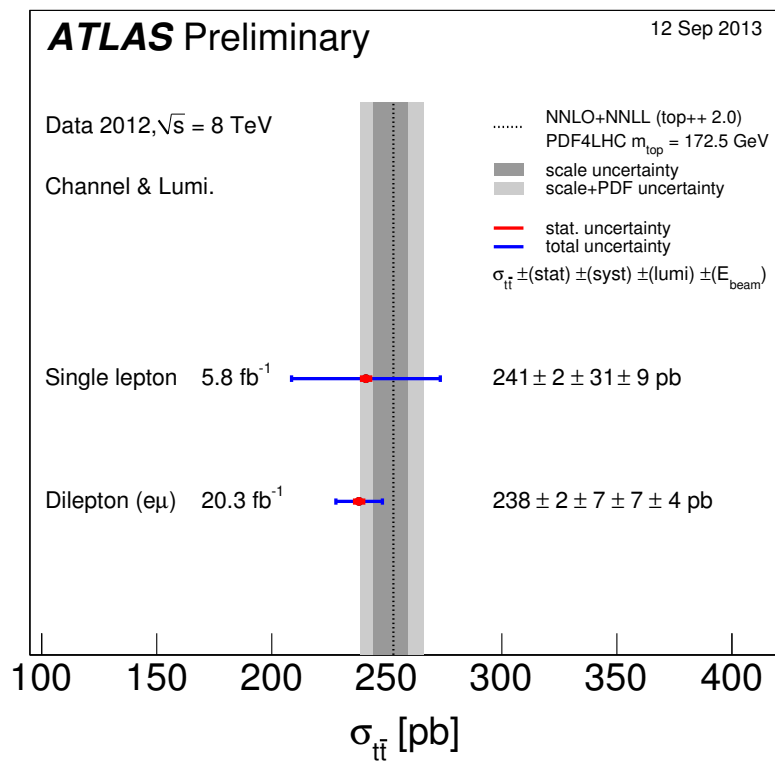


Figure 3.7: A summary of all $t\bar{t}$ production cross section measurements performed at the LHC at $\sqrt{s} = 8 \text{ TeV}$. The theory prediction is shown as a dotted line with associated uncertainties as grey bands.

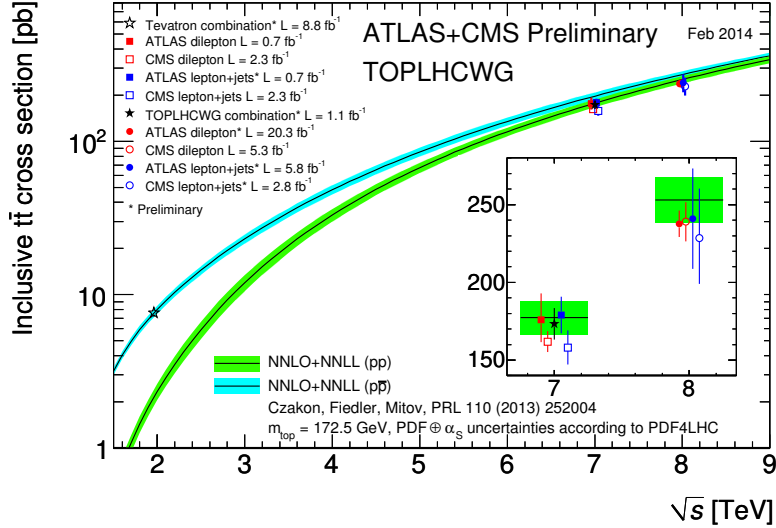


Figure 3.8: A summary of the most precise $t\bar{t}$ production cross section measurements performed at the LHC at $\sqrt{s} = 7$ and 8 TeV and the Tevatron at $\sqrt{s} = 1.96$ TeV compared to the theoretical prediction. The Tevatron results should be compared against the prediction for $p\bar{p}$ collisions while the LHC against the pp collision predictions.

marized in Figure 3.9, which includes the combined LHC measurement:

$$m_t = 173.29 \pm 0.23 \text{ (stat.)} \pm 0.92 \text{ (syst.) GeV}$$

406 Mass asymmetry measurement

As discussed in Section 2.3, the charge (C) and parity (P) symmetries are both violated in weak interactions. The CPT symmetry which includes time reversal (T) is the last remaining symmetry which no interaction appears to violate. Any deviations from this symmetry would have major implications on particles physics [37] and could manifest itself as differences between matter and antimatter particles. As the only quark which can be studied directly, measurement of $\Delta m \equiv m_t - m_{\bar{t}}$ could hint at any such deviation produced by new physics. Such a measurement was conducted by the ATLAS [38] experiment yielding the result:

$$\Delta m_t = -0.44 \pm 0.46 \text{ (stat.)} \pm 0.27 \text{ (syst.) GeV}$$

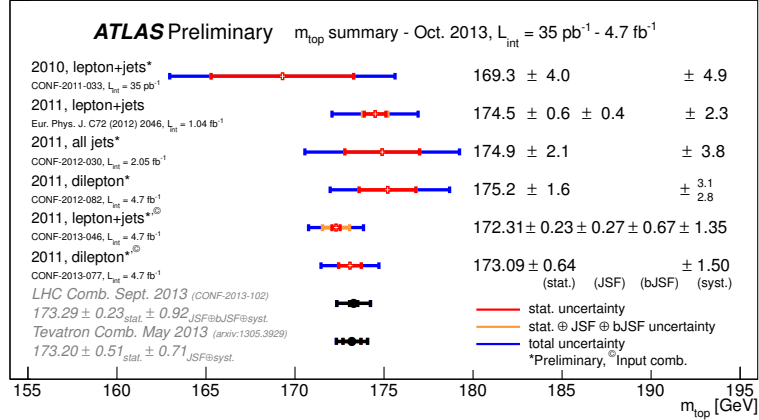


Figure 3.9: Summary of all m_t measurement results per analysis at ATLAS. The statistical combination of these results are compared to the combination from Tevatron.

and by the CMS [39] experiment yielding the result:

$$\Delta m_t = 0.67 \pm 0.61 \text{ (stat.)} \pm 0.41 \text{ (syst.) GeV}$$

407 which are both consistent with the SM prediction and imply CPT invariance.

408 **Boosted top resonance searches**

409 Some BSM theories predict the existence of additional particles with large masses which can
 410 decay into a pair of top quarks with very large transverse momenta. The decay products
 411 of these highly boosted tops emerge in a collimated “fat” cone. Boosted top searches have
 412 been carried out at ATLAS, looking for the decay products of a heavy boson known as the Z'
 413 and Kaluza-Klein gluons [40]. A narrow leptophobic Z' with a mass of less than 1.74 TeV is
 414 excluded and a Kaluza-Klein gluon is excluded for masses below 2.07 TeV.

⁴¹⁵ **Chapter 4**

⁴¹⁶ **The LHC and the ATLAS Detector**

⁴¹⁷ The Large Hadron Collider (LHC) [41] is a proton-proton ring collider located at the European
⁴¹⁸ Centre for Nuclear Research (CERN). The main LHC ring is housed in the tunnel which previ-
⁴¹⁹ ously contained the Large Electron-Positron collider. The LHC ring is 27 km in circumference
⁴²⁰ and located as deep as 175 m underground. The LHC services seven different experiments
⁴²¹ located around the beam-pipe (Figure 4.1). The four main experiments are: A toroidal LHC
⁴²² apparatus (ATLAS, the experiment used for this thesis), the compact muon solenoid (CMS), a
⁴²³ large ion collider (ALICE) experiment and the LHC beauty (LHCb) experiment.

⁴²⁴ ATLAS and CMS are general purpose detectors designed to support a varied physics pro-
⁴²⁵ gramme, from SM physics like top quark measurements to BSM searches such as supersym-
⁴²⁶ metry. ALICE and LHCb are more specialized experiments which focus on heavy ions and
⁴²⁷ B -physics, respectively.

⁴²⁸ **4.1 The Large Hadron Collider**

⁴²⁹ The LHC accelerates two beams of protons in opposite directions and then collides the two
⁴³⁰ beams at the four interaction points where the experiments are located. The protons come
⁴³¹ from hydrogen gas where the orbiting electron is removed by an electric field, leaving behind
⁴³² a bare proton. The beam acceleration occurs in several stages exploiting smaller experiments
⁴³³ present at CERN. During 2010 and 2011 protons were accelerated to a beam energy of 3.5 TeV,
⁴³⁴ creating a centre-of-mass energy of 7 TeV and then 4 TeV per beam in 2012 for a centre-of-mass
⁴³⁵ energy of 8 TeV. Each beam is made of multiple bunches of protons, with as many as hundreds

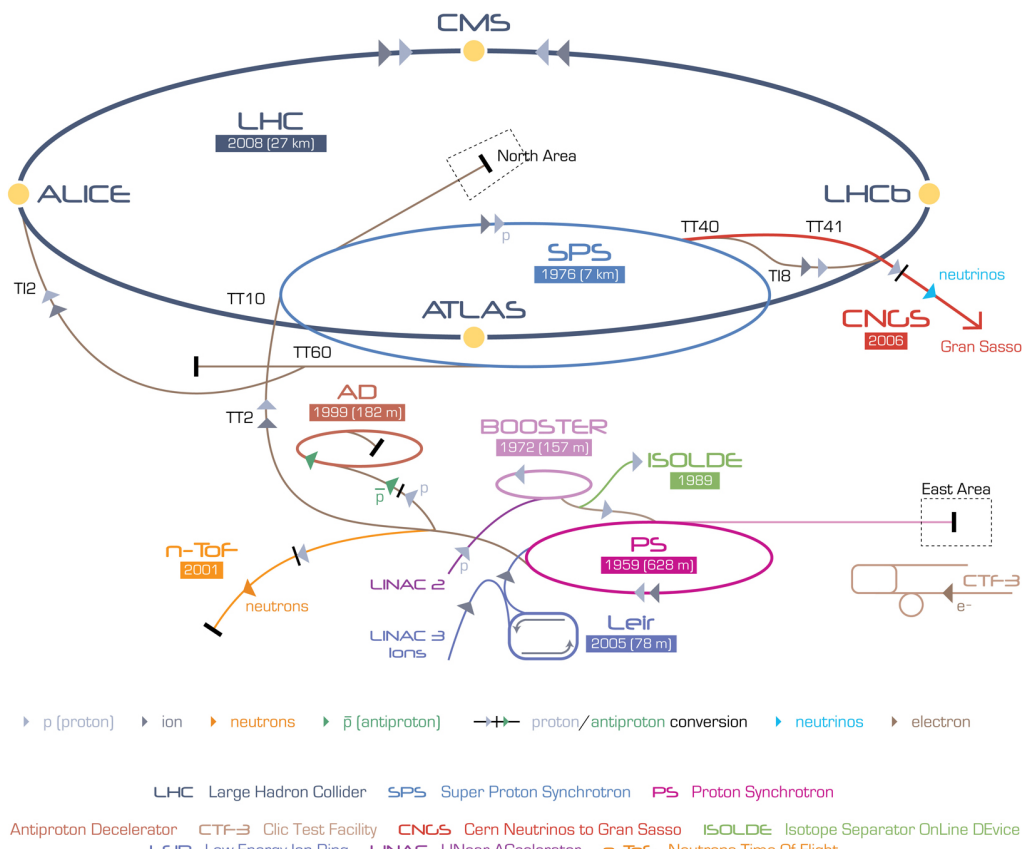
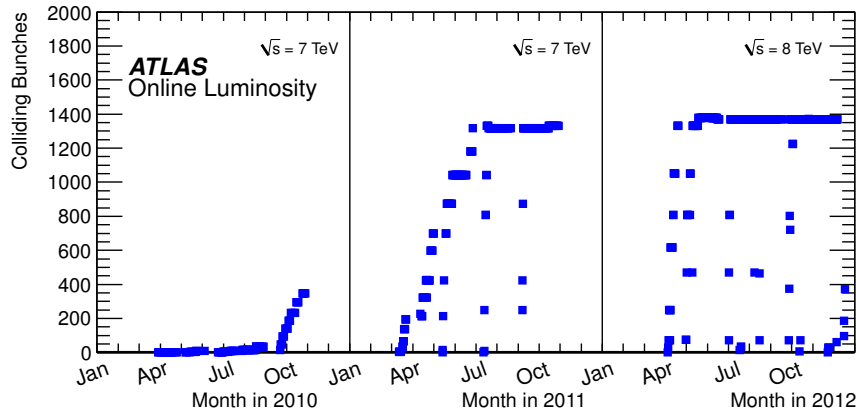
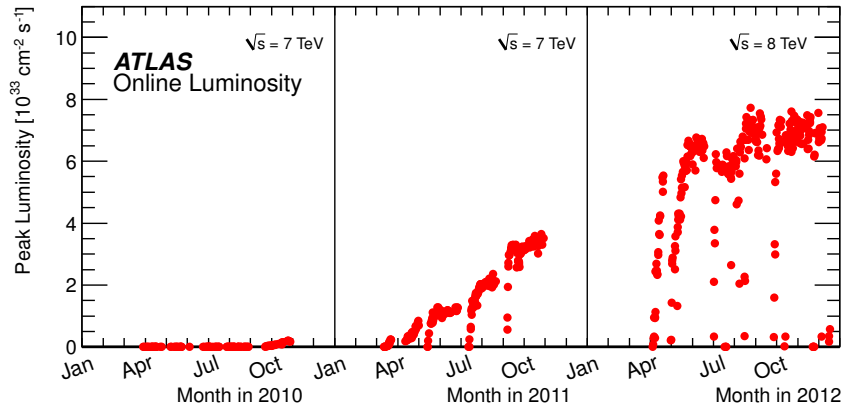


Figure 4.1: The layout of CERN complex of experiments, note the main four LHC experiments located at different points around the ring.

436 of billions of protons in each bunch. Bunches are grouped into *bunch trains* with a designed
 437 *bunch spacing* of 25 ns between each of the bunches that compose a single train. The bunch
 438 spacing and size of the bunch can be altered to adjust the amount of collisions and the time
 439 between collisions. During 2011 a 50 ns bunch spacing to allow for low pile-up analyses to be
 440 performed. The variation in the number of colliding bunches is shown in Figure 4.2a.



(a) The number of bunches colliding per unit time at the LHC for the 2010, 2011 and 2012 pp collision periods.



(b) The peak luminosity per unit time at the LHC for the 2010, 2011 and 2012 pp collision periods [1].

Figure 4.2: Shown in (a) is the number of bunches colliding at the LHC and (b) the peak luminosity per unit time.

441 The acceleration of the proton beams occurs in several stages, within several different
 442 accelerators. The beams are first accelerated in a linear collider (LINAC 2) to an energy of
 443 50 MeV before being injected into the proton synchrotron booster (PSB). The beams are then
 444 boosted to 1.4 GeV by a varying magnetic field in the circular PSB. The beams are then passed

445 into the proton synchrotron (PS) and then the super proton synchrotron (SPS) where the beam
 446 energy increases to 26 GeV and then 450 GeV. At this stage the beam is injected into the LHC
 447 and then accelerated to the final desired energy. The design energy is 7 TeV per beam for a
 448 total of 14 GeV centre-of-mass energy. From injection of the protons into LINAC 2 to stable
 449 beam conditions in the LHC, the whole process can take a couple of hours.

450 As bunches overlap the protons that make up the bunches interact, these interactions are
 451 known as events. The number of events is proportional to the instantaneous luminosity \mathcal{L} of
 452 the collider. \mathcal{L} is a measure of the flux of particles per unit area per unit time can be defined
 453 as:

$$\mathcal{L} = f n_b \frac{N_1 N_2}{A} \quad (4.1)$$

454 where f is the frequency of revolution of the beam, n_b the number of colliding pairs of bunches
 455 in the beam, N_1 and N_2 are the number of particles in each colliding bunch and A is the cross-
 456 section of the beam [42]. The peak luminosity evolution at the LHC is shown in Figure 4.2b.

457 Note that the operational \sqrt{s} of the LHC was 7 TeV for 2010/11 and 8 TeV for 2012.

458 The total amount of data collected is measured by the integrated luminosity \mathcal{L}_{int} defined
 459 as the time integral of \mathcal{L} . Integrated luminosity has units of inverse area, usually expressed
 460 in terms of barns (b)¹. The probability for a given process to occur is expressed as the cross-
 461 section σ and the total number of events which proceed via said process is defined as:

$$\sigma \int \mathcal{L} dt \quad (4.2)$$

462 The integrated luminosity delivered by the LHC and collected by the ATLAS detector in
 463 2011 and 2012 is shown in Figure 4.3. The ATLAS detector does not record all data delivered
 464 by the LHC; approximately 6.5% was not recorded.

465 4.1.1 Pileup

466 Due to the large number of interactions and the short time between collisions, multiple events
 467 can overlap into a single event. This has detrimental effects on physics analyses and is a de-
 468 termining factor in setting the instantaneous luminosity with which to perform data collec-

¹1 b⁻¹=10⁻²⁸ m⁻²

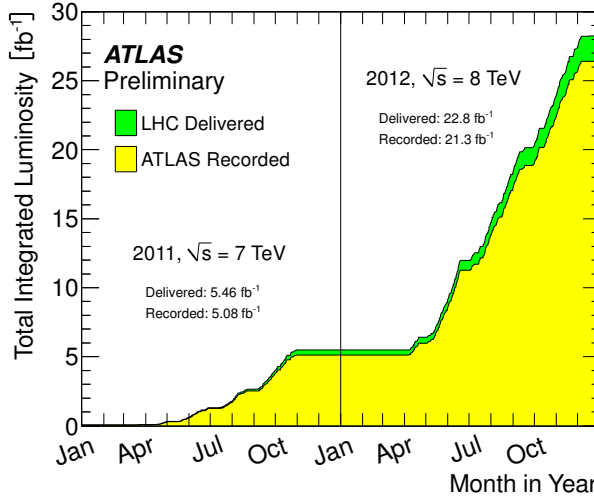


Figure 4.3: Distribution of the total integrated luminosity delivered by the LHC and the recorded by ATLAS for the 2011 and 2012 pp collision period. Note the \sqrt{s} changing from 7 TeV to 8 TeV between 2011 and 2012 [1].

469 tion. This overlapping effect is collectively known as pileup and is categorized into two types:
 470 in-time pileup, where multiple pp collisions occur during the same bunch crossing; and out-
 471 of-time pileup, where the electric signals produced by previous collisions still remain to be
 472 read-out. This occurs when the time spacing between interactions is smaller than the read-out
 473 speed of the electronics. The number of interactions per crossing μ is shown in Figure 4.4,
 474 note that on average approximately thirty interactions occurred per bunch crossing in 2012.
 475 In comparison, in 2011 the average interactions per bunch crossing $\langle \mu \rangle$ varied from 5 in early
 476 2011 to 15 at the end of the year.

477 4.2 The ATLAS detector

478 The ATLAS [2] experiment is a general-purpose detector which wraps around the IP providing
 479 large angular coverage. ATLAS is approximately cylindrical with a diameter of 25 m, a total
 480 length of 44 m and weighs 7000 t. The detector is made of several layers of instrumentation
 481 located at successively increasing radii as shown in Figure 4.5:

- 482 1. **Inner Detector:** Located nearest to the beam-pipe and designed to measure the track
 483 of charged-particles.
- 484 2. **EM Calorimeter:** Used for identification and measurement of electrons and photons.

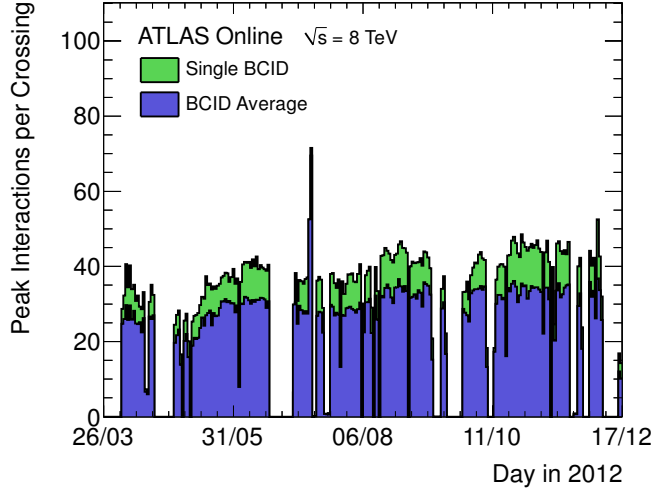


Figure 4.4: Number of interactions per bunch for the 2012 pp data-taking period at ATLAS per day. Both the average number of interactions for all bunches and the maximum number of interactions are shown [1].

485 3. **Hadronic Calorimeter:** Used for the measurement of hadronic activity from hadronizing
486 partons and missing transverse energy.

487 4. **Muon Spectrometer:** The outermost detection layer, used for muon identification and
488 measurement.

489 Between these detection layers are magnets responsible for bending the path of the charged
490 particles for the purpose of momentum measurement and particle identification. Additionally
491 triggering and data acquisition (DAQ) systems form part of the detector for the purposes of
492 recording the data signals coming from the aforementioned tracking and measurement sys-
493 tems. A brief description of these systems is provided in the coming sections. For a more
494 detailed technical description of the detector and all subsystems see [43].

495 Lepton plus jets $t\bar{t}$ events produce a final state that includes hadronic activity, electrons,
496 muons and missing energy and thus all elements of the detector are used in the reconstruction
497 of such events. Additionally the match χ^2_{match} tagger which is central to this thesis, relies on the
498 reconstruction and fitting of ID tracks and MS tracks. A detailed description of this algorithm
499 is provided in Section 4.4.2.

500 A cylindrical coordinate system as used by all ATLAS publications has been adopted here.
501 The coordinate system is constructed so that the z -axis is parallel to the beam axis. The x -axis

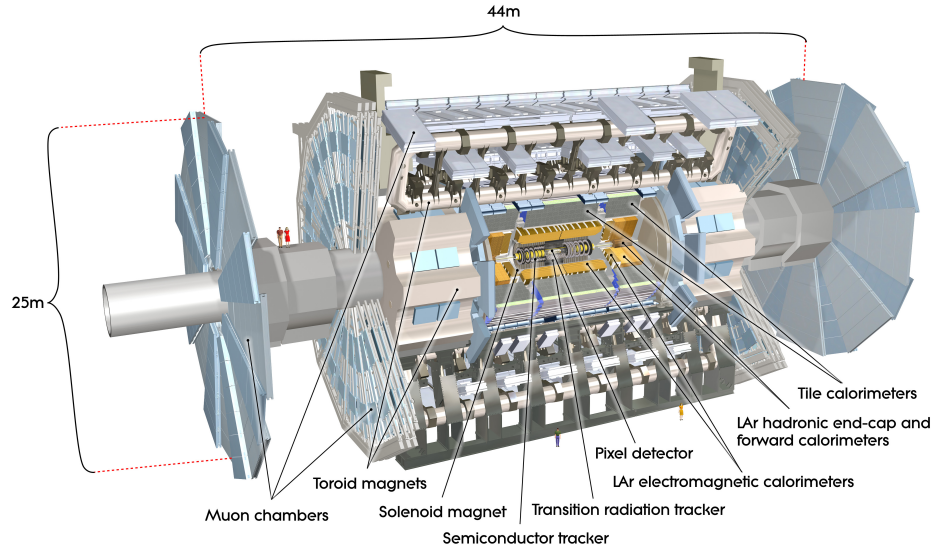


Figure 4.5: An overview diagram of the ATLAS experiment. Shown are all detection and tracking systems and the toroid magnet which encompasses them. Note also the muon system on the outside of the detector.

502 is positive in the direction going from the IP to the centre of the LHC ring, and the positive
 503 y -axis points upwards. Thus the x - y plane is transverse to the beam direction. All transverse
 504 variables such as the transverse momentum p_T , transverse energy E_T and missing transverse
 505 energy E_T^{miss} are measured along this plane. The azimuthal angle ϕ is measured around the
 506 beam axis, and the polar angle θ is the angle from the beam axis. The pseudorapidity is defined
 507 as $\eta = -\ln \tan(\theta/2)$. The distance in the η - ϕ plane between two objects is denoted by ΔR and
 508 defined as $\Delta R = \sqrt{\Delta\eta^2 + \Delta\phi^2}$. Finally side A of the detector is defined as the positive z side
 509 and side C is the negative z . Finally, the distance perpendicular to the beam-pipe is denoted by
 510 R . The transverse impact parameters d_0 is defined as the distance of closest approach (perigee)
 511 of a track to the primary vertex. The longitudinal impact parameter z_0 is the distance in z
 512 between the perigee and the primary vertex.

513 4.2.1 Inner Detector

514 The inner detector (ID) (Figure 4.6) is a tracking detector located closest to the beam-pipe and
 515 used for momentum and impact parameter measurement, vertex and track reconstruction and
 516 particle identification. The ID is designed to provide hermetic, high-resolution tracking in the
 517 range $|\eta| < 2.5$.

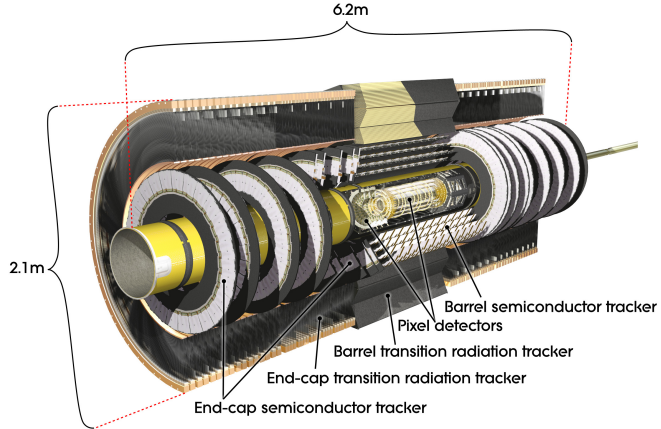


Figure 4.6: Drawing of the ATLAS inner detector.

518 The entire ID is contained within the central solenoid (CS) that generates a 2 T magnetic
 519 field for the purpose of momentum measurement. The trajectory of a charged particle is bent
 520 in the presence of a magnetic field by an amount proportional to the momentum of the particle

521

$$r = \frac{p_T}{qB} \quad (4.3)$$

522 where r is the bending radius, p_T and q are the transverse mass and charge of the particle,
 523 respectively, and B is the magnetic field strength. The reconstruction of the path allows a
 524 measurement of the momentum. A particle with larger p_T would have a more straight trajec-
 525 tory than a low- p_T particle in the same magnetic field. For a central track with $p_T = 5$ GeV the
 526 relative resolution on the measured transverse momentum is $\sim 1.5\%$ [2].

527 The reconstruction of interaction vertices is of paramount importance, particularly when
 528 considering the large amount of pile-up observed at ATLAS. Interaction vertices are recon-
 529 structed by fitting all reconstructed tracks to a point. The primary vertex (PV) is then defined
 530 as the vertex with the largest amount of momentum associated with it. In addition the recon-
 531 struction of secondary interaction vertices is used for the identification of short-lived particles
 532 such as b -hadrons and τ .

533 The ID is made of three separate tracking and detection systems located at increasing radii
 534 away from the beam-pipe, the full arrangement can be seen in Figure 4.8a and a plane-view is
 535 shown in Figure 4.8b.

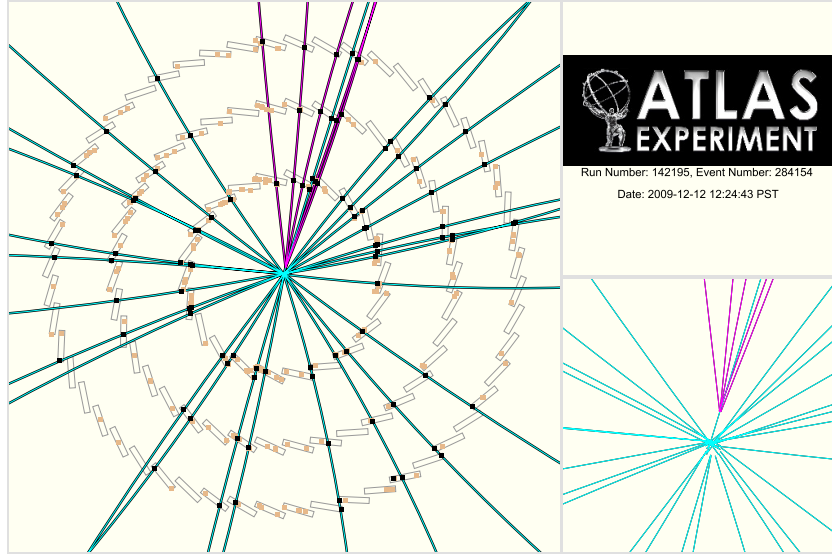
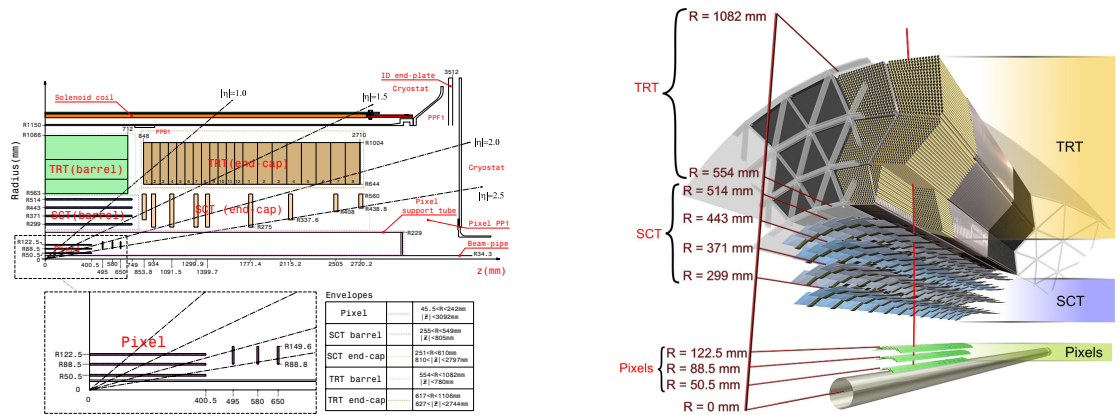


Figure 4.7: An event-display of an event as reconstructed by the ATLAS inner detector. Shown are the results of the vertexing algorithm where each line represents a track. The purple tracks have been fitted to a secondary vertex.



(a) Plan-view of a quarter-section of the ATLAS ID showing the major detector elements with its active dimensions and envelopes. Note also the η markers showing the maximum coverage up to $\eta = 2.5$ [2].

(b) A drawing in the transverse plane of the ATLAS ID showing all major detection elements in the barrel regions [2]. A charged particle track is shown traversing all the detector elements as a solid line.

536 **Pixel detector**

537 The pixel detector is located nearest to the beam-pipe and provides high-granularity and preci-
538 sion for secondary vertex reconstruction. As a charged particle passes through a silicon pixel,
539 an electron-hole pair is created. The electron and hole begin drifting in opposite directions
540 under the influence of a voltage and the charge is then read out through an electrode. This
541 signal is read out as a *hit* by read-out electronics. The pixel detector consists of three silicon
542 pixel sensor layers in the barrel region located at approximately 5 cm, 9 cm and 12 cm from
543 the IP, and three disks at each side located at constant R providing coverage up to $|\eta| < 2.5$.
544 The barrel modules are overlapped in a turbine pattern to provide hermetic coverage. In the
545 barrel region the modules provide an intrinsic resolution of 10 μm in R - ϕ and 115 μm in z [2].
546 The disk sections have an intrinsic resolution of 10 μm (R - ϕ) and 115 μm (R).

547 **Semiconductor tracker**

548 The semiconductor tracker (SCT) located in the intermediate radius range is designed to pro-
549 vide eight hits per track contributing to the measurement of momentum, impact parameter
550 and vertex position. The SCT is made of four layers of stereo-pair silicon micro-strip sensors
551 in the barrel region at increasing radii with an intrinsic resolution of 17 μm (R - ϕ) and 580 μm
552 (z). At the end-caps nine disks of silicon microstrip modules provide large η coverage with a
553 resolution of 17 μm (R - ϕ) and 580 μm (R) [2].

554 **Transition radiation tracker**

555 The transition radiation tracker (TRT) is the outermost tracking layer that forms the ID and it
556 acts as both a tracker and transition radition detector. Transition radiation (TR) is produced
557 when a charged particle crosses the boundaries of two materials with different dielectric con-
558 stants. The probability of producing TR photons depends on the Lorentz factor of the particle
559 $\gamma = E/m$. Thus for two particles of the same energy, a lighter particle will on average emit
560 more ionization than a heavier particle.

561 The TRT is designed to provide up to 36 hits per track using straw-tube sensors. Each
562 straw is 4 mm in diameter and is made of two 35 μm thick Kapton multi-layer films bonded
563 back-to-back. At the center of each straw is a gold plated tungsten wire with a diameter of

564 31 μm and the straw is filled with a mixture of gas (70 % xenon, 27 % CO₂ and 3 % O₂). The
 565 tubes are surrounded by polypropylene-polyethylene fibers that act as radiators and allow for
 566 the production of TR, which later ionizes the gas mixutre and is read-out through the gold-
 567 plated wire.

568 In the barrel the 144 cm long straw-tubes are arranged in modules which contain between
 569 329 and 793 straws. The end-cap disks are made of radially distributed 36 cm long straw-
 570 tubes. Each straw-tube provides an intrinsic resolution of 130 μm along its length [2]. The
 571 combination of a large number of hits over a large radius allows measurements in the TRT to
 572 be made with an accuracy that can complement those made by the pixel detector.

573 **4.2.2 Calorimetry**

574 The ATLAS calorimeter is responsible for the measurement of the energy of particles that
 575 emerge from the event. Sampling calorimeters are used for this purpose, layers of absorber
 576 material (passive) are placed in the path of the particles forcing them to interact and shower.
 577 The amount of energy lost by the incident particle depends on the type of material the parti-
 578 cle traverses, the energy of the particle and the type. At high energies electrons lose energy
 579 predominantly via Bremsstrahlung, while photons lose energy via pair production. The char-
 580 acteristic length associated with this energy loss is a material characteristic known as the
 581 radiation length X_0 .

582 For electrons the energy as a function of material traversed is

$$E = E_0 e^{-x/X_0} \quad (4.4)$$

583 where E is the energy of the incident particle, E_0 is the initial energy and x is the distance
 584 traversed. As an electron traverses one X_0 of material, its energy is reduced by a factor of $1/e$.
 585 For photons the average number of photons traversing through a material length x is reduced
 586 exponentially by a factor of $\frac{7}{9}X_0$. Thus the longitudinal length of the shower is proportional
 587 to the logarithm of the energy of the incoming particle.

588 The number of shower particles changes as a function of the interaction length λ_{int} as

$$N = N_0 e^{-x/\lambda_{\text{int}}} \quad (4.5)$$

589 where N is the number of shower particles at length x and N_0 is the initial number of inci-
 590 dent particles. This is the characteristic length used when discussing the construction of the
 591 hadronic calorimeter. For a given material the λ_{int} is much larger than X_0 and thus therefore
 592 hadronic showers tend to be much broader and deeper than EM showers. Note that on average
 593 1/3 of the particle content of a hadronic showers is EM mostly due to pion decay into photons.

594 The energy of the resulting shower is then measured by some sampling material (active)
 595 located behind the absorbers, this energy is proportional to the energy of the incident particle.

596 The type and thickness of material used is varied through the pseudorapidity range to
 597 improve energy measurement and reduce punch-through of particles into the muon systems
 598 behind. Due to the large amount of intense radiation produced during collisions, radiation
 599 hardness is also a driving factor in material choice.

600 The ATLAS calorimeter consists of the EM calorimeter, designed to measure photons and
 601 electrons covering the pseudorapidity region $|\eta| < 3.2$; the hadronic calorimeter (HCal), which
 602 measures hadronic activity covering the pseudorapidity region $|\eta| < 3.2$; and the forward
 603 calorimeter (FCal) which provides energy measurement capability in the very high pseudo-
 604 rapidity region $3.1 < |\eta| < 4.9$. As can be seen in Figure 4.9 the calorimetry envelopes the
 605 ID and CS providing hermetic coverage symmetric in ϕ . This is particularly important for the
 606 measurement of E_T^{miss} resulting from weakly interacting particles escaping the detector.

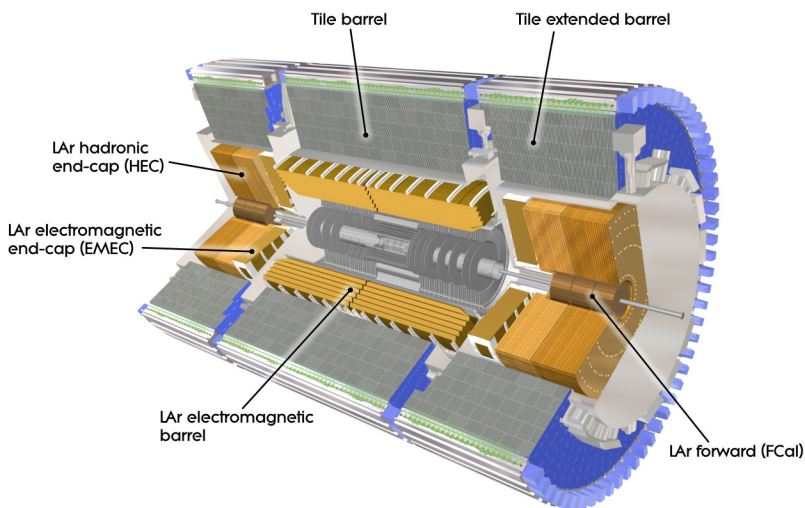


Figure 4.9: A cut-away diagram of the ATLAS detector highlighting the calorimetry system. Shown are the ECal barrel and end-cap, the HCal barrel and end-cap and the FCal end-cap [2].

Section	Resolution
EM Barrel	$\frac{10.1\%}{\sqrt{E}} \oplus 0.17\%$ [44]
EMEC	$\frac{10\%}{\sqrt{E}} \oplus 0.7\%$
HEC	$\frac{100\%}{\sqrt{E}} \oplus 10\%$
FCAL	$\frac{100\%}{\sqrt{E}} \oplus 10\%$

Table 4.1: Design energy resolution of all ATLAS calorimeter components. The resolution is made of a sampling term ($1/\sqrt{E}$) associated with the choice of passive and active materials and the construction of the layers, and a constant term associated with the depth of the detector, cracks and dead material.

607 **Electromagnetic calorimeter**

608 The EM calorimeter is made of a barrel section ($|\eta| < 1.475$) and two end-caps ($1.375 <$
 609 $|\eta| < 3.2$). The EM barrel consists of two half-barrels separated by a 4 mm gap at $z = 0$.
 610 The end-caps consist of two coaxial wheels, the outer ring covering the pseudorapidity range
 611 $1.375 < |\eta| < 2.5$ and the inner ring covering the range $2.5 < |\eta| < 3.2$. The pseudorapidity
 612 region $1.37 < |\eta| < 1.52$ is not used for precision physics due to the large amount of material,
 613 this is known as the “crack” region.

614 The EM calorimeter employs liquid Argon (LAr) as the active material due to its intrinsic
 615 radiation hardness and response over time, and lead as the passive material arranged in an
 616 accordion geometry for full ϕ symmetry. Particles interact with the lead absorbers creating a
 617 shower which ionizes the layers of liquid Argon. A potential is applied across the LAr mate-
 618 rial allowing for signal readout via Kapton/copper electrodes. The total thickness of the EM
 619 calorimeter is $> 24X_0$ in the barrel and $> 26X_0$ in the end-caps. The amount of material is
 620 optimized in pseudorapidity to enhance energy resolution.

621 In the region devoted to precision physics the EM calorimeter is divided into three seg-
 622 ments as shown in Figure 4.10, the strip layer is designed to improve particle identification
 623 and pseudorapidity position measurement. The design energy resolution for all components
 624 of the calorimeter are shown in Table 4.1.

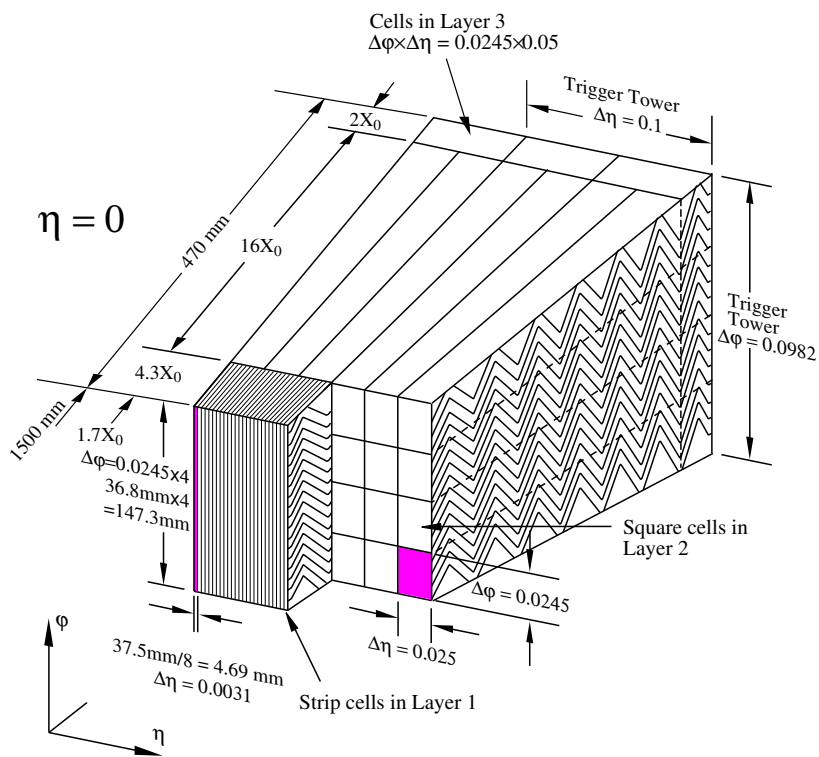


Figure 4.10: Cut-away diagram of the EM calorimeter barrel at $\eta = 0$. Shown are the three different layers with varying cell structures. The strip section is designed to enhance particle identification and position measurement in η .

625 **Hadronic calorimeter**

626 The hadronic calorimeter uses different types of passive and active material to accommodate
627 for the varying conditions in different regions of the detector. The materials used and structure
628 of the detector must provide good energy resolution, full symmetric coverage for the purpose
629 of E_T^{miss} measurement, full containment of all hadronic activity to prevent punch-through to
630 the muon system and be sufficiently radiation hard.

631 The hadronic calorimeter consists of two parts a scintillator tile calorimeter in the barrel
632 region, and a LAr calorimeter in the end-cap.

633 The tile calorimeter is located directly outside the EM calorimeter. The barrel portion of
634 the calorimeter covers the region $|\eta| < 1.0$ and the two extended barrels cover the range
635 $0.8 < |\eta| < 1.7$. The tile calorimeter uses steel as the passive material and scintillating tiles
636 as the active material. The resulting hadronic showers enter the scintillating tiles and produce
637 photons which are passed to photomultiplier tubes. The total detector thickness which is tile-
638 instrumented is $9.7\lambda_{\text{int}}$ at $\eta = 0$.

639 The hadronic end-cap (HEC) uses LAr technology due to its radiation-hardness in this
640 challenging high pseudorapidity region. The HEC consists of two independent wheels per end-
641 cap covering the range $1.5 < |\eta| < 3.2$ overlapping the tile calorimeter at low pseudorapidity
642 range and the forward calorimeter located at high pseudorapidity.

643 **Forward calorimeter**

644 The forward calorimeter (FCal) is responsible for energy measurement in the very-high pseu-
645 dorapidity range $3.1 < |\eta| < 4.9$ of both electromagnetic and hadronic activity. Due to the
646 large amount of radiation in this region, LAr is employed as the active material. The FCal con-
647 sists of three layers, the first made primarily of copper, designed mostly for the measurement
648 of electromagnetic activity while the two outer tungsten layers are responsible for hadronic
649 activity measurement.

650 **4.2.3 Muon spectrometer**

651 The muon spectrometer (MS) is the outer most layer of the ATLAS detector (Figure 4.11) and
652 is responsible for the precision measurement of p_T of charged-particles that pass-through the

653 ATLAS calorimetry. It is designed to detect charge particles leaving the calorimeters and mea-
 654 sure their momentum with a precision of 10 % at a momentum of 1 TeV [2]. Muon tracking
 655 performance is vital to the SMT tagger described in Section 4.4.4, as it relies on the precise
 656 reconstruction of muon tracks in the ID and MS. Inner detector tracks and Muon spectrometer
 657 tracks are fitted to form a *combined* muon track, the quality of the fit is at the core of the SMT
 658 algorithm.

659 Due to their larger mass, muons tend to have a larger transverse momentum and as such
 660 do not lose as much energy through the emission of photons in the calorimetry. As a result,
 661 muons tend to traverse the hadronic calorimeter and escape the detector volume. The muon
 662 system provides measurement of these particles up to $|\eta| < 2.7$ and triggering up to $|\eta| < 2.4$.
 663 Measurement of p_T is facilitated by the magnetic field generated by the large toroid magnet
 664 in the barrel region $|\eta| < 1.4$ and two smaller end-cap magnets in $1.6 < |\eta| < 2.7$. In the
 665 transition region ($1.4 < |\eta| < 1.6$) deflection is provided by the barrel and end-cap fields.

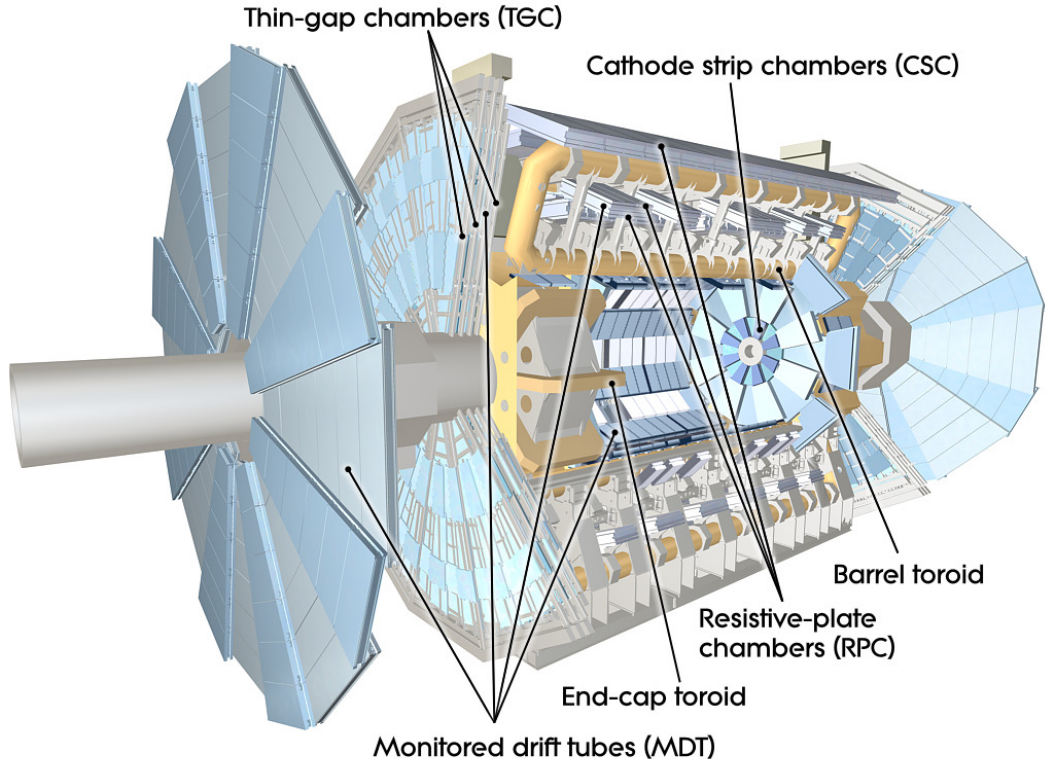


Figure 4.11: Cut-away drawing of the ATLAS muon system.

666 The structure of the MS is delimited by the magnet system. In the barrel region three

Monitored drift tubes	MDT
- Coverage	$ \eta < 2.7$ (innermost layer: $ \eta < 2.0$)
- Number of chambers	1150
- Function	Precision tracking
Cathode strip chambers	CSC
- Coverage	$2.0 < \eta < 2.7$
- Number of chambers	32
- Function	Precision tracking
Resistive place chambers	RPC
- Coverage	$ \eta < 1.05$
- Number of chambers	606
- Function	Triggering, second coordinate
Thin gap chambers	TGC
- Coverage	$1.05 < \eta < 2.7$ (2.4 for triggering)
- Number of chambers	3588
- Function	Triggering, second coordinate

Table 4.2: Main parameters of the muon system [2].

667 cylindrical layers of precision-tracking chambers are located in and on the coils of the barrel
 668 toroid magnet at radii of 5 m, 7.5 m and 10 m. End-cap region coverage is provided by three
 669 chamber planes perpendicular to the z -axis located in front and behind the end-cap toroid
 670 magnet at distances $|z| \approx 7.4$ m, 10.8 m, 14 m and 21.5 m from the interaction point.

671 The MS contains four different types of chambers responsible for precision-tracking and/or
 672 triggering in various pseudorapidity ranges as shown in Table 4.2. The arrangement of these
 673 chambers is shown in Figure 4.12.

674 In the barrel region, precision-measurement is performed by monitored drift tubes (MDT)
 675 chambers. These chamber consist of three to eight pressurized aluminium drift tubes, each
 676 containing a tungsten-rhenium wire anode and a mixture of argon and carbon dioxide gas. An
 677 average spatial resolution of 80 μm per tube and 35 μm per chamber is achieved.

678 The end-cap region is instrumented with cathode-strip chambers (CSC) due to their higher
 679 rate capability and time resolution. CSCs are multiwire chambers with cathode planes seg-

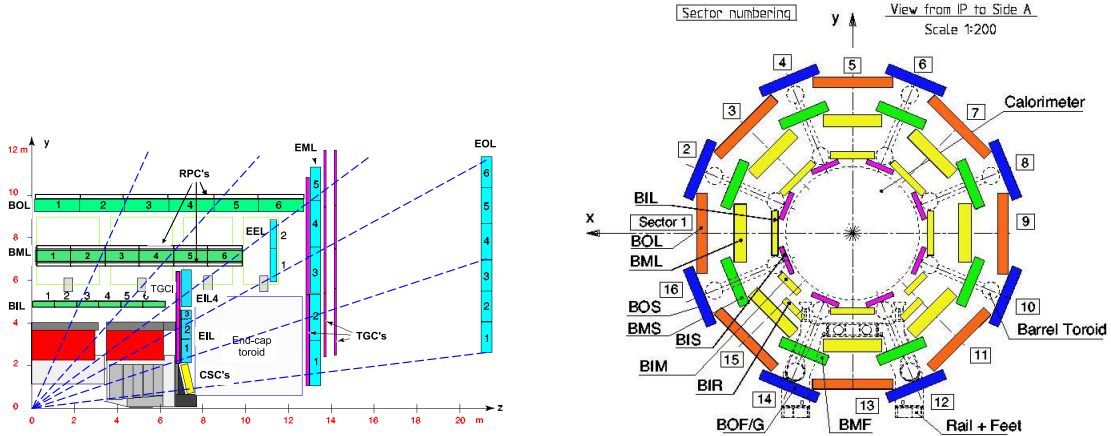


Figure 4.12: Plan view of quarter-section of the ATLAS detector. Figure 4.13: Transverse view of the muon system. Shown are the

680 mented into strips in orthogonal directions. This allows both coordinates to be measured si-
 681 multaneously. The resolution of a chamber is $40\text{ }\mu\text{m}$ in the bending plane (R - z) and 5 mm in
 682 the transverse plane.

683 Triggering on muon tracks is another essential role of the muon spectrometer. To this end,
 684 each precision-measurement chamber is complemented with fast triggering chambers. As with
 685 the measurement layers, two different types of chambers are used for the barrel and end-cap
 686 regions. In the barrel region ($|\eta| < 1.05$) resistive plate chambers (RPC) are used attached to
 687 the same support structure as the MDTs. The RPCs are made of two resistive plates, 2 mm
 688 apart, between which a potential difference is applied. The gap between the plates is filled
 689 with a mixture of $\text{C}_2\text{H}_2\text{F}_4/\text{Iso-C}_4\text{H}_{10}/\text{SF}_6$. The signal is read out via metallic strips mounted to
 690 the outer faces of the resistive plates. The end-cap region ($1.05 < |\eta| < 2.4$) is populated with
 691 thin gap chambers (TGC). TGCs multiwire chambers like those used in the CSC, however the
 692 distance between the wire and the cathode is smaller in the TGC. A summary of the spatial
 693 and temporal resolution for the measurement and triggering layers is shown in Table 4.3.

694 **4.2.4 Magnet system**

695 The structure of the ATLAS detector is defined by the large magnet system. The ATLAS magnet
 696 system, shown in Figure 4.14, consists two sets of magnets. The central solenoid and three air-
 697 core toroids.

698 The central solenoid located nearest to the beam, provides a 2 T magnetic field for the ID
 699 for the purpose of tracking, particle identification and p_{T} measurement.

Chamber	Resolution in		
	R/z	ϕ	Time
MDT	35 μm (z)	–	–
CSC	40 μm (R)	5 mm	7 ns
RPC	10 mm (z)	10 mm	1.5 ns
TGC	2-6 mm (R)	3-7 mm	4 ns

Table 4.3: Summary of spatial and temporal resolutions per chamber for all chamber types used in the ATLAS muon spectrometer. Adapted from [2].

700 The barrel toroids extend to $|\eta| < 1.4$ and are made of eight coils, generating a 0.5 T
 701 magnetic field for the MS. In the high pseudorapidity range, magnetic deflection is provided
 702 by two end-cap toroids extending from $1.6 < |\eta| < 2.4$. As in barrel, the end-cap toroids are
 703 made of eight coils offset by 22.5° with respect to the barrel coils. Each end-cap generates a 1 T
 704 magnetic field for the MS. The so-called transition region between the two magnets is covered
 705 by an overlap of the end-cap and barrel fields.

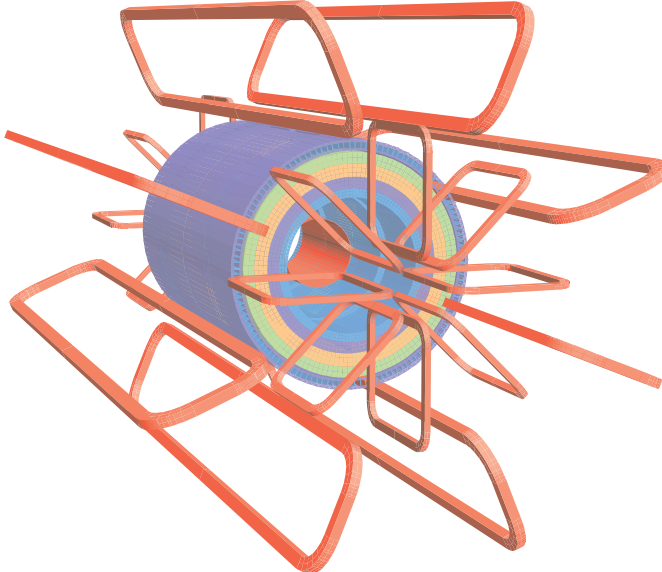


Figure 4.14: Diagram of the ATLAS toroid magnet system. The red central solenoid is located closest to the beam surrounded by layers of tile calorimetry. The eight barrel toroid magnets are shown along with the offset end-cap toroids at each end.

706 **4.2.5 Beam-pipe**

707 The beam-pipe section located within the ATLAS experiment is approximately 38 m in length
708 and made of seven parts. The central chamber has an inner diameter of 58 mm and is con-
709 structed from 0.8 mm thick beryllium due to the material’s transparency to particles, high
710 specific stiffness and compatibility with ultra-high vacuum. The beam-pipe is centred around
711 the IP and integrated with the pixel detector. The additional layers are made of stainless steel
712 located symmetrically on both sides of the IP.

713 **4.2.6 Triggering and DAQ**

714 At the design luminosity of the LHC $\mathcal{L} = 10 \times 10^{34} \text{ cm}^{-2} \text{ s}^{-1}$, the expected event rate is ap-
715 proximately 1 GHz. At an average event size of 1.3 MB per event, the total amount of data
716 produced at ATLAS is 1.2 PB s^{-1} . The maximum rate of data storage at ATLAS is approxi-
717 mately 300 MB s^{-1} , so the rate must be reduced.

718 The trigger and data acquisition system (TDAQ) is responsible for selecting only “inter-
719 esting” events for recording, thus reducing the rate. This is known as an *online selection* as it
720 happens before the data is stored. Selections during analysis for example, are known as *offline*
721 *selection*, as they happen after the data has been recorded.

722 The overwhelming majority of events produced at the LHC are of no interest to physics
723 analysis, for example the so-called *minimum bias events*.

724 At ATLAS, trigger decisions are carried out in three sequential levels: *Level 1* (L1), *Level*
725 *2* (L2) and *Event Filer* (EF), each successive level reduces the rate by applying increasingly
726 more complex selection criteria. The hardware-based L1 trigger, performs the initial selection
727 based on reduced-granularity information from the MS trigger chambers and all calorimeters.
728 Data from the calorimeter trigger towers, shown in Figure 4.10, is used to search for presence
729 of high transverse-momentum muons, photons, electrons, hadronic decays of τ leptons and
730 hadronic jets, as well as large missing transverse energy and large total transverse energy.
731 The central trigger processor applies the the trigger ‘menu’ which includes a combination of
732 selection criteria. Events which are of interest to physics analyses can be produced at such
733 a rate as to overwhelm the capabilities of the DAQ. A *prescale* can be applied to record one
734 out of many of these events, thus reducing the rate. The L1 trigger also constructs *regions of*

735 *interest* (RoIs) around the detector where interesting features have been found. The η and ϕ
736 information of the RoI along with information about the decision is stored and passed to the
737 higher level triggers.

738 The L2 selection makes use of RoIs and the full granularity of the detector to further reduce
739 the event rate to approximately 3.5 kHz and finally the EF implements selections commonly
740 used for offline analysis to reduce the rate to 200 Hz.

741 **4.3 Monte Carlo Simulation**

742 The simulation of data is paramount to HEP research, from the initial detector design phase all
743 the way through to finalized analyses. Monte Carlo (MC) generators simulate various inter-
744 actions, creating kinematic collision event data that reflect our best understanding of nature.
745 These processes are then passed through detector simulation and all the object reconstruction
746 algorithms, resulting in a dataset with an identical format to collision data. Simulation of data
747 happens in three phases: event generation, detector simulation and digitization.

748 **4.3.1 Event Generation**

749 Event generators are tools that model complex physics processes that occur during a particle
750 collision. Many different generators exist to model a variety of beam types (pp , $p\bar{p}$, e^+e^- ,
751 etc...) and event types. Hadronic event generation simulates all components which make up
752 the interaction, namely the hard scattering process, parton showering, hadronising, hadronic
753 decay, the underlying event and photon radiation [45] as shown in Figure 4.15.

754 First, the *hard interaction* of a pair of partons originating from the colliding protons is
755 simulated. An example of such an interaction is $q\bar{q} \rightarrow Z/\gamma^* \rightarrow e^+e^-$. Calculating the cross
756 section for such an interaction involves the convolution of the parton density function (PDF)
757 and the *matrix element* (ME).

758 The PDF $f_i(x, Q^2)$, describes the probability of finding, within the proton, a parton of
759 flavour i carrying a fraction x of the proton momentum, via a hard interaction with energy
760 scale Q . The ME describes the interaction between the two partons and corresponds to one
761 or more of the Feynman diagrams associated with the interaction². The order of a diagram is

²For a rigorous discussion of matrix elements and the Feynman rules, see [15, 16]

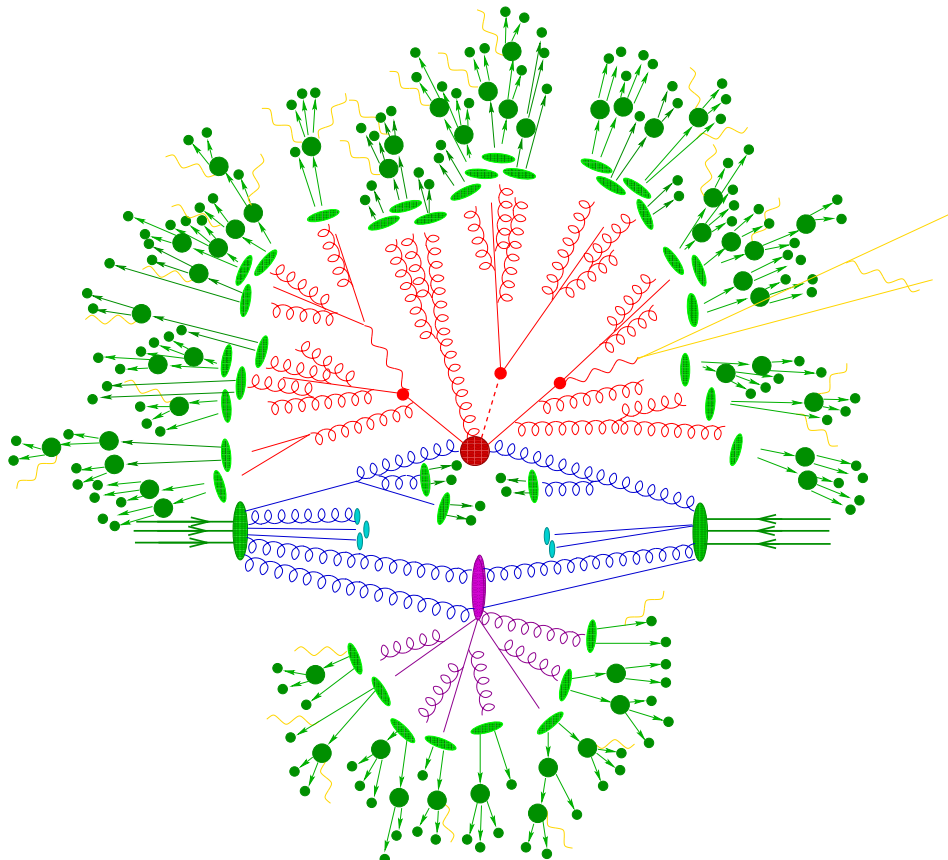


Figure 4.15: Sketch of a proton-proton collision as modelled by the event generator [3]. Shown are the incoming protons beams as green arrows on the left and right sides of the diagram. The partons shown in blue, interact in the hard interaction (red blob) producing a parton shower, also depicted in red, which eventually hadronize (light green blobs) and finally decay into final state particles shown in dark green. The *underlying event* is shown at the bottom of the diagram as the purple blob, note also the beam remnants as light blue blobs that also form part of the underlying event. Photon emission is shown in yellow and occurs at all stages of the event generation.

762 determined by the number of coupling constants associated with it. Different generators are
763 capable of treating diagrams at different orders. The hard interaction is usually modelled at
764 LO or NLO.

765 The next step is *parton-showering* which simulates the emission of gluons by coloured
766 partons. A cascade of partons is produced, as shown in Figure 4.15, and modelled by perturba-
767 tion theory for energies above 1 GeV. All coloured objects are then combined into colourless
768 hadrons in a process known as *hadronization*, these hadrons are subsequently allowed to decay.

769 Finally, the remaining coloured partons not involved in the hard interaction, are allowed
770 to interact forming the *underlying event*.

771 The kinematic information of the original event without the effects of the detector is kept
772 in the data set and is usually referred to as the *truth information*.

773 4.3.2 Detector simulation

774 The generated events are then passed through a detector simulation that mimics the response
775 of the detector to particles traversing through it. A description of the entire detector is im-
776 plemented in the GEANT4 tool-kit [46], including a map of the magnetic fields, the position
777 of the detector components and material description. The software then simulates the signal
778 voltages produced in all tracking and calorimeter components of the detector, these are then
779 passed through a simulation of the read-out electronics and DAQ taking into account known
780 losses and inefficiencies. All of this information is then passed on to the reconstruction soft-
781 ware that “rebuilds” the physics objects from the detector *hits*.

782 4.4 Object reconstruction

783 The process of converting the raw data from the detector into physics objects (electrons, muons
784 and so on) is known as *object reconstruction*. The algorithms for object reconstruction are
785 identical for both collision data and simulated data. As lepton plus jets decays of $t\bar{t}$ are the
786 focus of this thesis, the reconstruction procedures of all types of objects (excluding photons) are
787 relevant. This includes electron, muon and jet reconstruction as well as b -tagging algorithms.
788 The focus of this thesis, the soft muon tagger, relies on *STACO combined* muons, therefore
789 some details of the muon reconstruction algorithms are discussed here.

790 **4.4.1 Electron reconstruction**

791 The electron reconstruction [47] procedure at ATLAS depends on the pseudorapidity of the
 792 candidate. Only electrons that lie within the coverage of the ID are used here, therefore only
 793 the relevant procedure is described. The algorithm used in the central region identifies energy
 794 deposits in the EM calorimeter and associates them with reconstructed ID tracks. Firstly, clus-
 795 ters are seeded from energy deposits with total E_T above 2.5 GeV using a sliding-window algo-
 796 rithm with window size 3×5 in units of 0.025×0.025 in (η, ϕ) space. Tracks with $p_T > 0.5$ GeV
 797 are then extrapolated to the middle layer of the EM calorimeter and then matched to the cluster
 798 seed using cuts in the (η, ϕ) space. In case of multiple matches, tracks with pixel or SCT hits are
 799 given priority and the match with the smallest ΔR distance is chosen. Finally, the size of the
 800 cluster associated with the candidate electron is enlarged to 3×7 and 5×5 in the barrel and
 801 endcap regions respectively. The energy of the electron is then the sum of four contributions
 802 taking into account energy deposited before the EM material, and leakages to other clusters
 803 or beyond the EM calorimeter.

804 Electron identification for central electron candidates is done by applying sequential cuts on
 805 calorimeter, tracking and combined track-cluster variables. Several sets of selection criteria,
 806 labelled *loose*, *medium* and *tight*, are designed for use in analyses. These sets provide increasing
 807 background-rejection power at the cost of efficiency by introducing new cuts at each stage or
 808 by tightening previous cuts. The cut definitions are listed in Appendix A.

809 Additional requirements can be made on the so-called isolation of the electron. Three sets
 810 of isolation strategies are used at ATLAS [48]:

- 811 • **Calorimeter isolation:** The calorimeter isolation $E_T^{\text{cone}\Delta R}$ is defined as the sum of
 812 transverse energy deposited in the cells around the electron in a cone of size ΔR . The
 813 contribution from the electron itself is removed within $\Delta\eta \times \Delta\phi = 0.125 \times 0.175$ around
 814 the electron cluster barycenter. It is corrected for energy leakage from the electron into
 815 the isolation cone and for the effect of pile-up. At ATLAS the nominal cone sizes used
 816 are $\Delta R=0.2, 0.3$ and 0.4 .
- 817 • **Track isolation:** The tracking isolation $N_{\text{trk}}^{\text{cone}\Delta R}$ is defined as the number of tracks in
 818 a cone around the electron, excluding the track of the electron itself.
- 819 • **Momentum isolation:** The momentum isolation $p_T^{\text{cone}\Delta R}$ is defined by the sum of the

820 transverse momentum of tracks with $p_T > 0.4 \text{ GeV}$ in a cone around the electron, ex-
 821 cluding the electron track itself.

822 **4.4.2 Muon reconstruction**

823 Muon reconstruction makes use of the information provided by both the inner detector and
 824 the muon spectrometer systems. Several different strategies exist [49]:

- 825 • **Standalone reconstruction:** Uses MS information only, first constructing *segments*
 826 from several hits in a given chamber and then fitting segments from all three stations to
 827 hits from the four MS components. Tracks are then extrapolated back to the IP taking
 828 into account energy loss and multiple scattering.
- 829 • **Tagging ID tracks reconstruction:** Uses MS or calorimeter information to tag ID
 830 tracks as muons.
- 831 • **Combined track reconstruction:** Standalone muon tracks are extrapolated back to
 832 the vertex and matched to ID tracks within ($|\eta| < 2.5$) and combined. This results in an
 833 improved momentum sensitivity from ID and MS information.

834 These strategies can be implemented in a variety of ways. There are two prominent fam-
 835 ilies, STACO and MUID, that contain reconstruction packages which exploit one or a combi-
 836 nation of these strategies. The STACO combined algorithm is used by the SMT tagger and is
 837 described in more detailed below.

838 **STACO Combined Algorithm**

839 The STACO package [50] combines ID and MS tracks by performing a statistical combination
 840 of the two independent tracks using track parameters ($\eta, \phi, p_T, d_0, z_0$) and their covariance
 841 matrices. The quality of the fit is represented in the resulting χ^2_{match} :

$$842 \quad \chi^2_{\text{match}} = (\mathbf{T}_{\text{MS}} - \mathbf{T}_{\text{ID}})^T (\mathbf{C}_{\text{MS}} + \mathbf{C}_{\text{ID}})^{-1} (\mathbf{T}_{\text{MS}} - \mathbf{T}_{\text{ID}}) \quad (4.6)$$

842 where \mathbf{T}_{MS} and \mathbf{T}_{ID} contain the track parameters for the MS track and the ID track respectively,

843

$$\mathbf{T}_{\text{MS or ID}} = \begin{pmatrix} \eta \\ \phi \\ p_{\text{T}} \\ d_0 \\ z_0 \end{pmatrix} \quad (4.7)$$

844 and \mathbf{C}_{MS} and \mathbf{C}_{ID} are the covariance matrices, defined as

$$\mathbf{C}_{ij} = (\mathbf{T}_i - \langle \mathbf{T}_i \rangle)(\mathbf{T}_j - \langle \mathbf{T}_j \rangle) \quad (4.8)$$

845 where $\langle \mathbf{T}_i \rangle$ is the expectation value of \mathbf{T}_i . The full covariance matrix is shown in Appendix C.

846 If more than one possible combination per track exists, the best combined χ^2_{match} is chosen
 847 and then the track is removed from the pool of tracks to be match. The algorithm continues
 848 making associations until no more tracks remain.

849 Finally, tracking, calorimeter and momentum isolation variables are defined in a similar
 850 way as with electrons.

851 4.4.3 Jet Reconstruction

852 As quarks and gluons hadronize and fragment they produce an increasing number of soft
 853 hadrons or high energy photons. A jet reconstruction algorithm attempts to recombine all
 854 these components to reconstruct the four-momentum vector of the original quark/gluon. This
 855 process results in an object known as a “jet”. These jets are the closest physical representation
 856 of a hard quark or a gluon available to experimentalists. The development of jet reconstruc-
 857 tion algorithms is driven by theoretical and experimental requirements. Theoretically it is
 858 crucial that jet algorithms be *infrared and collinear safe*. The probability of gluon emission
 859 approaches infinity in the collinear and soft regime. These infinities cancel out with virtual
 860 gluon emission. If jets resulting from hard particles are merged or split due to soft emission or
 861 collinear splitting these probabilities do not cancel and a divergence occurs. A jet algorithm is
 862 said to be soft and collinear when the reconstructed jets remain unchanged under the addition

863 of a soft emission or a collinear splitting. In additions jet algorithms should be able to work
 864 given parton-level, hadron-level or calorimeter information. From an experimental perspective
 865 some of the requirements for a jet algorithm are: stability under increased luminosity or
 866 center-of-mass energy, computationally efficient and fast, and work independently of detector
 867 technology.

868 There are many different jet reconstruction algorithms such as the Cambridge/Aachen, k_T
 869 and SISCone algorithms. However only the ATLAS default, known as the anti- k_T algorithm,
 870 is described and used here.

871 **Anti- k_T algorithm**

The anti- k_T algorithm is a clustering algorithm that sequentially combines objects to form cone-shaped jets [51]. This algorithm has been found to be more resilient to the effects of pile-up and underlying event and the shape of the jet is unaffected by soft radiation producing regularly shaped jets with a circular area, amongst other advantages [51]. The clustering process begins by measuring the distance between all particles, d_{ij} , and the distance between particle i and the beam d_{iB} defined as

$$d_{ij} = \min(k_{T,i}^{-2}, k_{T,j}^{-2}) \frac{\Delta_{ij}^2}{R^2}$$

$$d_{iB} = k_{T,i}^{-2}$$

872 where $\Delta_{ij}^2 = (y_i - y_j)^2 + (\phi_i - \phi_j)^2$, and $k_{T,i}$, y_i and ϕ_i are the transverse momentum, rapidity
 873 and azimuthal angle of object i . The parameter R defines the characteristic cone size of the jet,
 874 note that by construction not all anti- k_T jets are conical. For every object both distances are
 875 calculated, if d_{ij} is the smallest then objects i and j are combined forming protojet, if q_{iB} is
 876 smallest the object is labelled as a final jet and removed from the list of objects to be combined.
 877 This process continues until all objects are removed.

878 In general soft particles will tend to combine with hard objects before combining with other
 879 soft objects. If two hard objects lie at $2R$ from each-other, they will both form conical shapes
 880 with radius R . Otherwise partially conical jets will form depending on the relative magnitudes
 881 of k_T of each particle. The standard value of R used for ATLAS analyses is 0.4, this is used
 882 here unless stated otherwise.

883 **Jet calibration**

884 The process of jet calibration is intended to correct the jet energy as measured in the detector
885 so as to recover the energy of the original stable particle jet that entered the detector. Clusters
886 of energy deposits (topo-clusters) in the calorimeter are constructed from topologically con-
887 nected calorimeter cells [52]. Calorimeter jets are constructed from topo-clusters that enter
888 the clustering algorithm as massless particles.

889 These clusters are initially reconstructed at the EM scale, which correctly measures the
890 energy of particles in EM showers. If jet reconstruction is carried on these clusters the jets
891 are known as EM jets. An additional collection of topo-clusters is created by calibrating the
892 calorimeter cells to correctly reconstruct the response of the calorimeter to hadrons. The
893 main calibration scheme is known as *local cluster weighting* (LCW). In this scheme each topo-
894 cluster is classified as electromagnetic or hadronic based on shower shape variables, then
895 simulation-derived corrections are applied to each cluster. These correct for the effects of
896 non-compensation, signal losses due to threshold effects, and energy loss in non-instrumented
897 regions of the calorimeter. These corrected topo-clusters are then used in the jet reconstruction
898 algorithms, to build LCW jets.

899 Additional corrections are applied to topo-clusters at either EM or LCW scale in an attempt
900 to restore the *jet energy scale* (JES) to that of jets reconstructed from simulated stable particles.
901 These correct for the effects of pile-up, point the jet to the primary vertex rather than the
902 ATLAS centre and additional corrections derived from MC simulations. Jets corrected in this
903 way are said to be at the EM+JES scale or LCW+JES scale depending on the scale of the topo-
904 clusters. Each calibration methodology has some uncertainties associated with it, which vary
905 with jet p_T and η [53].

906 **4.4.4 b -jet tagging techniques**

907 The ability to identify jets as originating from a b -quark or a c -quark (HF), or uds/g (LF) is very
908 important in the study of many types of interactions such as $t\bar{t}$ events. This process is known
909 as b -tagging. Many b -taggers have been developed at ATLAS to achieve the highest b -tagging
910 efficiency along with strong rejection of jets from c and LF quarks. These algorithms exploit
911 impact parameters (IP3D), secondary vertex reconstruction (SV1) and more complicated algo-

912 rithms that exploit the topology of the b - and c -hadron decays (JetFitter). The output of these
 913 variables are used as inputs into multivariate algorithms to provide enhanced b -tagging capa-
 914 bilities. The MV1 tagger is one such algorithm and is used as the default at ATLAS. Finally,
 915 *soft lepton tagging* (SLT) exploits the production of leptons within some b -jets to provide sepa-
 916 ration from LF. The performance of these b -taggers is shown in Figure 4.16. The tagger used in
 917 this thesis is an implementation of soft lepton tagging described in more detail in Section 4.4.4.

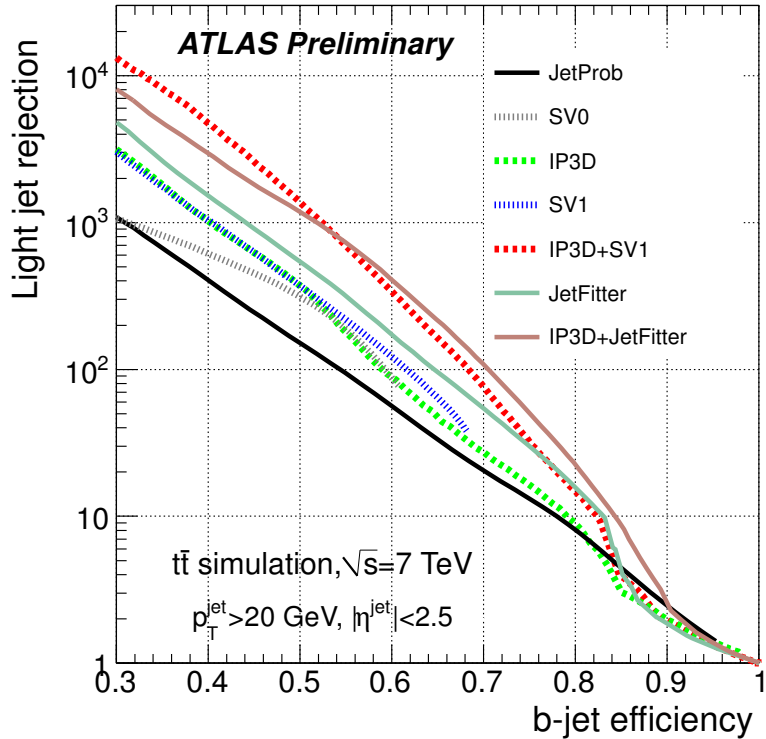


Figure 4.16: Light jet rejection as a function of the b -jet tagging efficiency, comparing some of taggers used at ATLAS as measured in simulated $t\bar{t}$ events [4].

918 The SV0 and SV1 algorithms

919 The SV0 algorithm [54] reconstructs secondary vertices using the tracks within the cone of
 920 the candidate jet. These secondary vertices are located at a decay length L from the primary
 921 vertex. A cut is then applied on the decay length significance $L/\sigma_L < 5.72$, this is an operating
 922 point that yields a b -tagging efficiency of 50 % as measured on simulated inclusive $t\bar{t}$ events.

923 The SV1 algorithm is an extension of the SV0 algorithm. In order to improve the tagging
 924 performance, three properties of the secondary vertex are used as inputs to a likelihood ratio,

namely the invariant mass of the tracks associated to the vertex, the ratio of the sum of the energies of the tracks in the vertex to the sum of the energies of the tracks in the jet, and the number of two-track vertices. Additionally the ΔR between the jet axis and the line joining the primary and secondary vertices is also used.

The JetFitter algorithm

The JetFitter algorithm [4] uses a Kalman filter to find a line along which the b , c and the primary vertices lie, along with their position on the line, giving an approximated flight-path for the b -hadron. Discrimination is based on a likelihood using similar variables as in the SV1 algorithm and additional variables such as the flight length significances of the secondary vertices.

The IP3D algorithm

The IP3D algorithm makes use of the transverse and longitudinal impact parameter significances in two-dimensional histograms to discriminate between b , c and LF jets. A likelihood-ratio method is used: the IP significances are compared to pre-defined smoothed and normalized distributions for b - and light-jets hypotheses. This produces a weight distribution for each model and a cut is applied to select jets. The IP3D algorithm is often combined with the JetFitter (IP3D+JetFitter) or SV1 algorithm (IP3D+SV1) to provide additional discriminating power.

The MV1 algorithm

The MV1 algorithm uses the output weights of the IP3D, SV1 and JetFitter algorithms as inputs to an artificial neural network. The current working point used at ATLAS is set at a b -tagging efficiency of 70 % with an associated mistag rate of less than 1.5 % [55] depending on the η and p_T of the jet in question.

Soft Lepton Tagging

Soft lepton tagging (SLT) algorithms attempt to identify leptons produced in the semileptonic decay of b and c quarks for the purpose of determining the presence of HF quarks. The term “semileptonic” here refers to the decay of a b -hadron in such a way as to produce a lepton-neutrino pair along with an additional hadron. The lepton produced would have a low- p_T and

Mode	Muon BR [%]
$b \rightarrow \mu^-$	$10.95^{+0.29}_{-0.25}$
$b \rightarrow c \rightarrow \mu^+$	8.02 ± 0.19
$b \rightarrow \bar{c} \rightarrow \mu^-$	1.6 ± 0.5
$b \rightarrow \tau^- \rightarrow \mu^-$	0.42 ± 0.04
All modes	21.0 ± 1.0

Table 4.4: Branching ratio for the production of a muon from a b -quark in both direct and indirect modes [7].

as such is known as a soft lepton. The SMT tagger exploits muons and as such these will be the focus of the following discussion.

A soft muon can be produced in a variety of ways starting from a b -quark, either directly via $b \rightarrow \mu \bar{\nu}_\mu X$, where X is any hadron; or indirectly, via a c , \bar{c} or a τ lepton. The direct and indirect via a c production mechanisms are shown in Figure 4.17. The branching-ratio for each of these decays is shown in Table 4.4. The total BR for the production of a soft muon from a b is $20.1 \pm 1.0 \%$, thus the probability for a $t\bar{t}$ event to contain at least one semileptonically decaying b is approximately 36 %.

Add plot
of pt
for SMT
muon
and W
muons

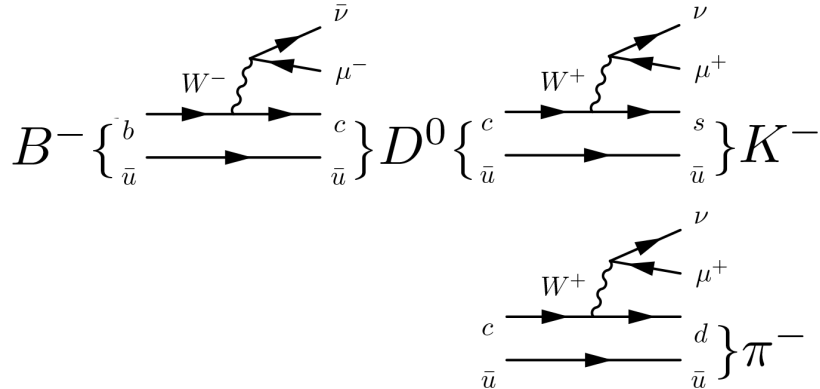


Figure 4.17: Feynman diagram of one of the mechanisms for lepton production via semileptonic b decay. Shown are the direct $b \rightarrow \mu$ and indirect $b \rightarrow c \rightarrow \mu$.

The SLT tagger used in this analysis is based on the quality of the fit between the ID track and MS track as represented by the χ^2_{match} . Several tagger-specific cuts are placed on the candidate muons and jet. Candidate SMT muons are required to lie within the coverage

963 of the ID ($|\eta| < 2.5$) and have sufficient transverse momentum for reliable reconstruction
964 ($p_T > 4 \text{ GeV}$). Requirements are made on the impact parameters of the muon ID track ($|d_0| <$
965 3 mm and $|z_0 \sin \theta| < 3 \text{ mm}$) to remove contributions from spurious matches between ID and
966 MS tracks, and from pile-up vertices. Finally, the main cut on the quality of the fit $\chi^2_{\text{DoF}} =$
967 $\chi^2_{\text{match}}/N_{\text{DoF}}$ is set at less than 3.2. This is an operating point that provides a b -jet (semileptonic
968 b -jet) identification efficiency of 10 % (50 %) and a LF rejection factor of 200 per jet.

969 Candidate jets are required to have more than three charged tracks associated with them
970 or a jet EM fraction smaller than 0.8. These criteria ensure that the jet did not originate from
971 the muon itself. Finally, the muon is associated to the jet with a cut $\Delta R_\mu^{\text{jet}} < 0.5$. The following
972 chapter describes the calibration of the SMT tagger.

973 **Chapter 5**

974 **Calibration of the Soft Muon Tagger
975 for 2012 ATLAS Data**

976 High-energy physics relies heavily on the use of simulated data to inform the development of
977 analysis techniques. It is thus paramount that the simulation reflect nature as closely as pos-
978 sible. However the simulation does not accurately predict conditions within the detector and
979 the effects on the muon reconstruction and the quality of the fit between the inner detector
980 tracks and muon spectrometer tracks which is represented in the χ^2_{match} . Instead the difference
981 between simulation and data is quantified and taken into account. This process is known as
982 calibration. In the case of the muon reconstruction method and the χ^2_{match} tagger it is impor-
983 tant that the difference in efficiency between MC and data be accounted for. This is done by
984 constructing a scale factor (SF), defined in this case by:

$$\text{SF}_{\chi^2_{\text{match}}} = \frac{\epsilon_{\chi^2_{\text{match}}}^{\text{Data}}}{\epsilon_{\chi^2_{\text{match}}}^{\text{MC}}} \quad (5.1)$$

985 One of the advantages of using the χ^2_{match} tagger over other forms of tagging is that the
986 presence of a jet is not required to measure the χ^2_{match} of a muon. This means that the calibra-
987 tion can be performed on isolated muons such as those from $J/\psi \rightarrow \mu\mu$ or $Z \rightarrow \mu\mu$ using
988 the so called tag and probe method. This calibration relies on muons with low- p_T from J/ψ
989 decays.

990 The tag and probe method used in this calibration is defined as follows. A STACO combined

muon is designated as the tag, this muon must pass a stringent set of cuts implying that this is indeed a muon from a J/ψ . The second muon which is designated as the probe is an ID track only. To ensure that the probe is the second muon from the J/ψ decay, the invariant mass of the combined tag and probe system is required to be within a mass window centered around the true J/ψ mass. The complete selection used in the calibration is detailed in Section 5.1. These probes are then used to measure the reconstruction efficiency and the χ^2_{match} tagger efficiency as described in Sections 5.2 and 5.3.

The tag and probe method used here is based on a previous calibration of the χ^2_{match} tagger performed on 2011 ATLAS collision data outlined in [10]. The analysis presented here differs from the 2011 calibration in several ways and these will be highlighted and explained.

Software, Collision Data and Simulated samples

The dataset used is made of those luminosity blocks selected by the recommended standard *good runs list* (GRL) which corresponds to all pp collision periods in 2012. The GRL selects only those luminosity blocks where detector conditions are appropriate for physics data-taking. This includes all relevant detector components being operational and that stable beam conditions have been achieved. The datasets are part of the 2013 summer reprocessing corresponding to data taken in periods A through to L, excluding periods F and J. In total this represents an integrated luminosity of 20.1 fb^{-1} .

The efficiency scale factor is measured against a sample containing almost 10 million $J/\psi \rightarrow \mu\mu$ events. At event generation, filters are applied so the sample only contains events where both truth muons have a momentum of at least 4 GeV and they must lie within the pseudorapidity range $|\eta| < 2.5$. This selection matches the object selection used by most analyses.

5.1 Tag and Probe Selection

The tag and probe procedure is as follows: first, require the presence of a STACO CB muon which passes a very stringent selection. This strongly implies that this is a real muon and thus is labelled as the Tag. Additionally a very loose selection is applied to all ID tracks. These are known as candidate Probes. Pairs of tag and probes are then formed by requiring that the

1019 combined invariant mass lie within a J/ψ mass window and the pair pass additional pairing
1020 cuts. This then implies that the Probe is likely the other muon from the J/ψ decay and as such
1021 is a suitable test-bed to measure the performance of the muon reconstruction algorithm. All
1022 selection criteria are detailed and explained in Section 5.1.2.

1023 After selecting a sample of probes the performance of the algorithm is estimated by mea-
1024 suring the proportion of probe candidates which are selected by the algorithm. In other words
1025 the performance is estimated by counting the number of muons which are reconstructed given
1026 that the ID track is very likely to be a real muon. Probes which are reconstructed into STACO
1027 CB muons are labelled as muon probes. The performance of the χ^2_{match} tagger is estimated in a
1028 similar manner, by measuring the proportion of combined muon probes which pass the SMT
1029 selection.

1030 **5.1.1 Trigger requirements**

1031 In order for an event to be included in the analysis it must pass at least one of the trigger chains
1032 listed in Appendix D. For the sake of brevity only the primary trigger EF_mu6_Trk_Jpsi_loose
1033 which contributes the majority of events is described here.

1034 As stated in the trigger name this is an Event Filter trigger which requires the presence of a
1035 muon with a momentum of at least 6 GeV and an ID track who's combined invariant mass lies
1036 within a J/ψ mass window of $2.6 \text{ GeV} < m_{\text{inv}} < 3.6 \text{ GeV}$. This loose mass window contains
1037 the entirety of the J/ψ peak in all examined p_T and η ranges as well as additional side bands
1038 to allow for background removal. Double muon triggers are not used to avoid introducing a
1039 bias by specifically selecting events with two good muons.

1040 While all triggers are operational in all periods, most are heavily prescaled and the prescale
1041 is period dependent. This does not have a first-order effect on the measurement since only ra-
1042 tios are compared between collision data and MC. However, the effective integrated luminosity
1043 is approximately 200 nb^{-1} as a result of the prescale. A short study was carried out to examine
1044 the effects of a multiple prescaled triggers on the scale factors. The SF were obtained with only
1045 the primary trigger and with all triggers enabled, no significant discrepancy between the two
1046 was detected.

STACO Combined Muon
$ \eta < 2.5$
$p_T > 4 \text{ GeV}$
$ d_0 < 0.3 \text{ mm}$
$ z_0 < 1.5 \text{ mm}$
$ d_0/\sigma_{d_0} < 3$
$ z_0/\sigma_{z_0} < 3$

Table 5.1: Tag selection criteria.

1047 5.1.2 Selection Cuts

1048 The selection criteria for tags, probes, muon probes and SMT muons are listed and detailed
 1049 below. Note that all cuts are applied on the kinematic properties measured in the ID due to its
 1050 improved resolution unless it is not possible as in the case of the χ^2_{match} which is a combined
 1051 MS and ID property. Also note that all objects must pass a set of track quality criteria as
 1052 recommended by the ATLAS *muon combined performance* (MCP) group. These cuts require
 1053 a certain number of detector elements be active to ensure good quality track reconstruction.
 1054 The selection criteria are listed in Appendix E.

1055 The tag selection is summarized in Table 5.1. The tag is a STACO combined muon with a
 1056 pseudorapidity and transverse momentum that allow for reliable reconstruction. The require-
 1057 ments on the impact parameter variables are in place to remove spurious muons from pileup
 1058 events and the decay-in-flight of long-lived hadrons. Finally, the tag muon is required to have
 1059 fired at least one of the triggers under which the event was recorded. This is done by matching
 1060 the reconstructed trigger object to the tag muon via a ΔR cut of less than 0.01.

1061 The probe selection is a subset of the tag selection and only requires an ID track with
 1062 $|\eta| < 2.5$ and $p_T > 4 \text{ GeV}$.

1063 The tag and probe pair selection is designed to select pairs which likely come from a J/ψ
 1064 decay. These pairing criteria are summarized in Table 5.2. The main component of the selection
 1065 is the invariant mass window cut, requiring the muons come from a J/ψ decay. The tag and
 1066 the probe are required to be well separated in $\eta\phi$ space to prevent the objects from entering
 1067 each others isolation cones.

1068 In the 2011 calibration analysis the track of the tag and the probe were refitted to a common

Opposite Charge
$ m_{J/\psi} - m_{\text{tag, probe}} \leq 2 \text{ GeV}$
$0.2 < \Delta R_{\text{probe}}^{\text{tag}} < 3.5$
$\Delta z_0 < 0.2 \text{ mm}$

Table 5.2: Pairing criteria.

1069 vertex and the quality of the refit, expressed by a χ^2 , was part of the pairing criteria. This cut
 1070 is present to reduce the effects of pile-up on the measurement by ensuring both objects have
 1071 a common origin. Since the data format used for this analysis is a derived form of that used
 1072 in 2011 it is not possible to perform such a refit. Instead, a cut on $\Delta z_0 = |z_{0, \text{tag}} - z_{0, \text{probe}}|$ is
 1073 applied. If several pairings are made for a single tag, the pair with the smallest Δz_0 is used.

1074 The STACO CB reconstruction efficiency is not measured by applying the algorithm on
 1075 the probe collection but rather a probe is said to be a muon probe if it matches a combined
 1076 muon from the STACO collection. This is done by requiring the ΔR between the probe and
 1077 the STACO CB muon be less than 0.01. Probes which are matched become the numerator of
 1078 the reconstruction efficiency and the denominator is defined as the number of probes:

$$\epsilon_{\text{reco}} = \frac{N_{\text{muon probe}}}{N_{\text{probe}}} \quad (5.2)$$

1079 A muon probe is said to be an SMT muon if it passes the selection listed in Table 5.3. These
 1080 cuts match the muon cuts defined in Section 4.4.4. Note in particular the main component of
 1081 the soft muon tagger, the cut on $\chi_{\text{match}}^2/N_{\text{DoF}} < 3.2$, the distribution of the χ_{DoF}^2 is shown in
 1082 Figure 5.1.

$ d_0 < 3 \text{ mm}$
$ z_0 \sin(\theta) < 3 \text{ mm}$
$\chi_{\text{match}}^2/N_{\text{DoF}} < 3.2$

Table 5.3: SMT criteria.

1083 Those muon probes which pass the SMT selection are the numerator of the SMT efficiency

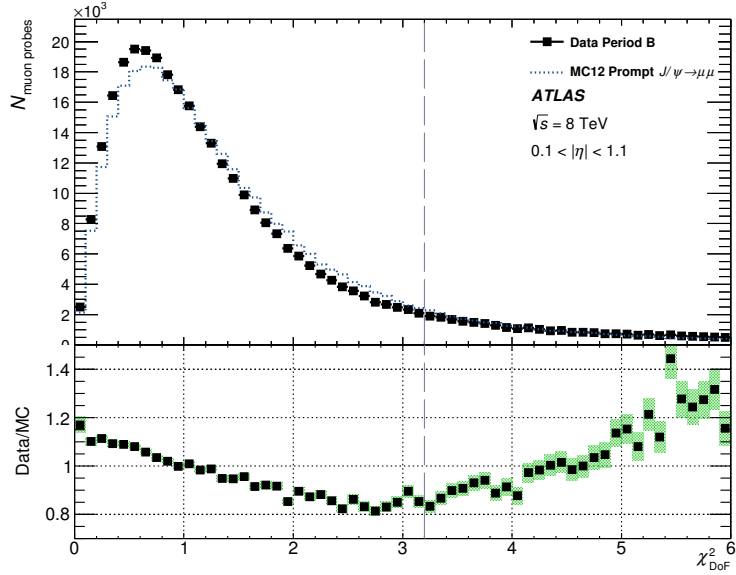


Figure 5.1: The distribution of χ^2_{DoF} for all muon probes for ATLAS collision data (solid dots) and prompt J/ψ Monte Carlo simulation (solid line). Note that the collision data distribution includes sources of background.

and the denominator is defined as the number of muon probes:

$$\epsilon_{\text{SMT}} = \frac{N_{\text{SMT}}}{N_{\text{muon probe}}} \quad (5.3)$$

5.2 Invariant mass fitting

The pairing criteria are very effective at selecting J/ψ events, however non- J/ψ background events also pass the selection. These include combinatorial background where the wrong tag and probe pair is constructed and Drell-Yan which appears as a continuum below the J/ψ peak.

The number of probes is extracted from a fit to the invariant mass of the dimuon system using a composite function to accommodate for the background and the Gaussian-like J/ψ peak.

The invariant mass peak of the J/ψ is modelled by a Gaussian distribution while the background is modelled with a quadratic polynomial. The invariant mass distribution is fitted by a sum of the two functions. Instead of relying on obtaining a good fit to the signal peak, the

1096 yield is obtained by subtracting the integral of the background function from the binned data.

1097 The integration is performed in a window with a width based on the width of the fitted J/ψ
 1098 peak. The integration window marked in Figure 5.2 corresponds to three times the width of the
 1099 peak (3σ). Additionally, note the composite fit line as well as the background-only distribution
 1100 and the implied signal Gaussian peak.

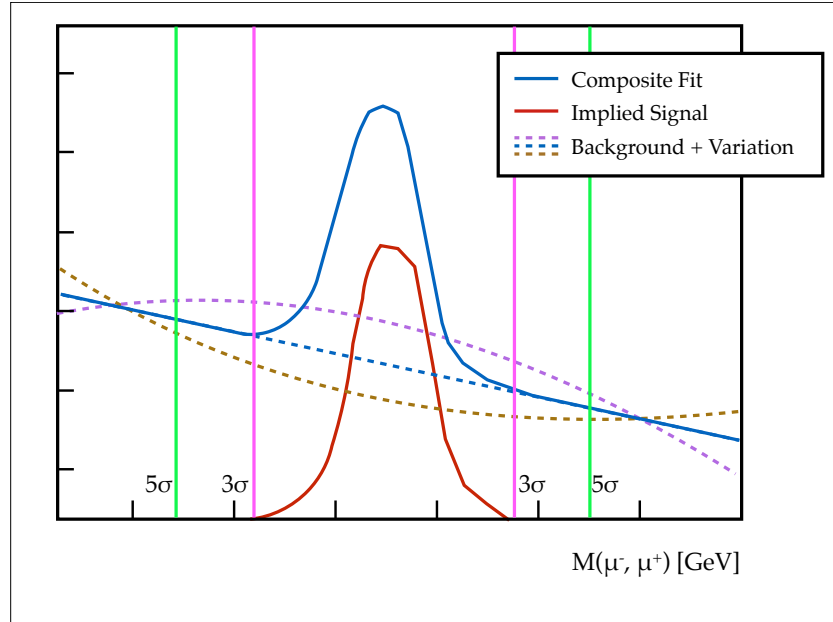


Figure 5.2: A drawing of the various components of the fit procedure. The composite fit is shown along with the corresponding implied signal and background. The two variations of the background shape are also shown, these are exaggerated for illustration purposes.

1101 Note that the J/ψ peak does not follow a Gaussian shape exactly, but rather the best fit is
 1102 obtained by the so-called Crystal Ball function shown in Figure 5.3. This is a convolution of a
 1103 Gaussian function with a power tail at low invariant mass to account for the energy loss due
 1104 to photon emission. Different combinations of signal and background functions were tested
 1105 to determine the most stable combination. For the signal the sum of two Gaussian functions
 1106 was tested, while for the background a linear function, an exponential function and the sum
 1107 of two exponential functions were tried. It was found that none of these yielded good stable
 1108 fits in the entire pseudorapidity range. For example, the linear function resulted in a mismod-
 1109 elling of the background at the probe level and yielded negative efficiencies or extremely large
 1110 uncertainties.

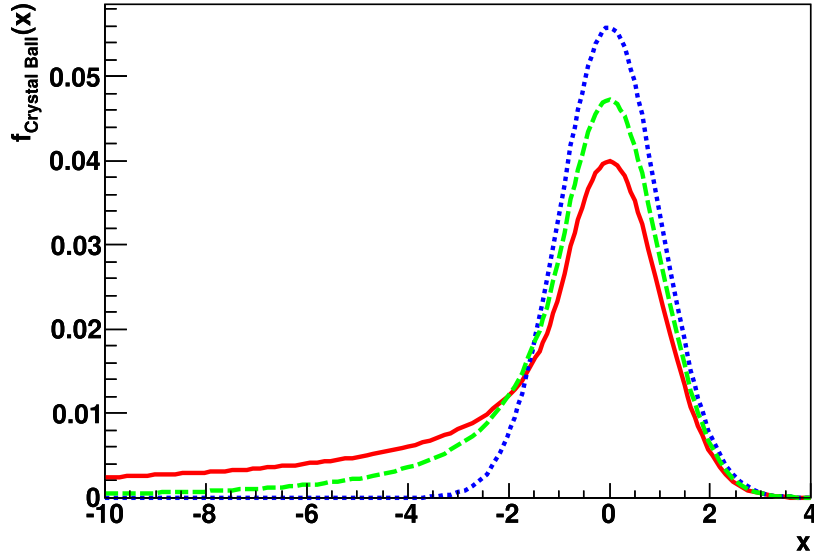


Figure 5.3: Diagrams of crystal ball distributions. Modified from [5].

1111 From an operational perspective using a Gaussian function allowed for a good stable fit
 1112 over the many hundreds of bins and simplified the fitting procedure. Any mismodelling of the
 1113 background because of the choice of a Gaussian in lieu of the Crystal Ball fit, is taken into
 1114 account by the background uncertainty described in the next section.

1115 Several different sets of initial fit conditions were tested and those which yielded the best
 1116 and most stable fits across the entire η and p_T range were used.

1117 The means of all the distributions are allowed to vary independently, meaning that the
 1118 mean obtained in the fit to the probe distribution does not influence the width of the Gaussian
 1119 function fitted to the muon probe distribution. The mean of the gaussian is expected to lie very
 1120 close to the true J/ψ mass, however this is not forced in the fitting procedure. Instead the fit
 1121 is allowed to set the mean in a window with a width of approximately 1.2 GeV. The width at
 1122 the probe level is obtained from the fit and is then used in the fits to the muon probe and SMT
 1123 distributions.

1124 **5.2.1 Uncertainty Measurement**

1125 The uncertainty on the efficiency is made of three components. First, the statistical uncertainty
1126 on the efficiency is estimated as a binomial error,

$$\Delta\epsilon = \sqrt{\frac{\epsilon(1-\epsilon)}{N}} \quad (5.4)$$

1127 where ϵ is the measured efficiency and N is, in this case the denominator of the efficiency
1128 measured.

1129 Secondly, an uncertainty is associated with the fit to the background. This is done by taking
1130 the largest upward and downward fluctuations of the background by the uncertainty on the
1131 fit parameters of the background, and obtaining the maximum upward and downward effects
1132 on the efficiency. After the fit of the composite function is carried out, a downward variation
1133 of the background is defined as:

$$f^{\text{down}}(x) = a_{\min}x^2 + b_{\max}x + c_{\min}, \text{ where } p_{\max/\min} = p_{\text{central}} \pm \sigma_p \quad (5.5)$$

1134 where the maximum and minimum of a parameter is obtained by varying the central value by
1135 the uncertainty obtained from the fit. The upward variation of the background fit is thus the
1136 opposite, defined as:

$$f^{\text{up}}(x) = a_{\max}x^2 + b_{\min}x + c_{\max} \quad (5.6)$$

1137 These background variations then result in the maximum deviation from the nominal in-
1138 tegral (Figure 5.2). The uncertainty on the efficiency is then determined by obtaining the max-
1139 imum efficiency in both directions. If the nominal efficiency is defined as

$$\epsilon_{\text{nominal}} = \frac{N_{\text{numerator}}^{\text{nominal}}}{N_{\text{denominator}}^{\text{nominal}}} \quad (5.7)$$

1140 then the variations are defined as,

$$\epsilon_{\text{up}} = \frac{N_{\text{numerator}}^{\text{up}}}{N_{\text{denominator}}^{\text{up}}}, \quad \epsilon_{\text{down}} = \frac{N_{\text{numerator}}^{\text{down}}}{N_{\text{denominator}}^{\text{down}}} \quad (5.8)$$

1141 where $N^{\text{up/down}}$ are the yields obtained from the intergration of the upward/downward vari-

1142 ations of the background function.

1143 Finally the uncertainty on the background is given by the average of the differences be-
1144 tween ϵ_{up} and ϵ_{down} , and the nominal efficiency:

$$\sigma_{\text{bkg}} = \frac{1}{2}(|\epsilon_{\text{up}} - \epsilon_{\text{nominal}}| + |\epsilon_{\text{down}} - \epsilon_{\text{nominal}}|) \quad (5.9)$$

1145 The final component of the uncertainty is constructed by varying the integration window.
1146 The nominal value is defined as 3σ away from the centre of the fitted Gaussian, where again
1147 σ is the FWHM of the same fitted Gaussian. An uncertainty is constructed by measuring
1148 the efficiency with a wide integration window corresponding to 5σ . The integration window
1149 uncertainty is defined as:

$$\sigma_{\text{window}} = |\epsilon_{5\sigma} - \epsilon_{3\sigma}| \quad (5.10)$$

1150 Finally, the total uncertainty on the efficiency is given by the sum in quadrature of the all
1151 uncertainty components. The uncertainty on the efficiency is then carried over to the scale
1152 factor determination. As expected the invariant mass distribution for all probes contains a
1153 large amount of background, particularly in data (Figure 5.4). The “shoulders” at each side of
1154 the J/ψ peak are the result of the tag-and-probe J/ψ trigger which includes a mass window
1155 cut more stringent than that required by the pairing selection. Requiring that the probe match
1156 a STACO CB muon greatly reduces the amount of background, applying the SMT requirements
1157 reduces the background though not as substantially.

1158 5.3 Efficiencies

1159 The efficiency is monitored as a function of a variety of kinematic variables, including the
1160 isolation, transverse momentum, azimuthal angle and the pseudorapidity of the probe.

1161 5.3.1 2011 Calibration

1162 As mentioned, the selection and fitting procedure used for this calibration are based on the
1163 2011 analysis [56]. In this calibration the efficiencies measured exhibited no dependence on
1164 ϕ , an asymmetric dependence on η particularly in the forward regions of the detector and a
1165 dependence on p_T . The scale factors were consistent with unity within their uncertainty across

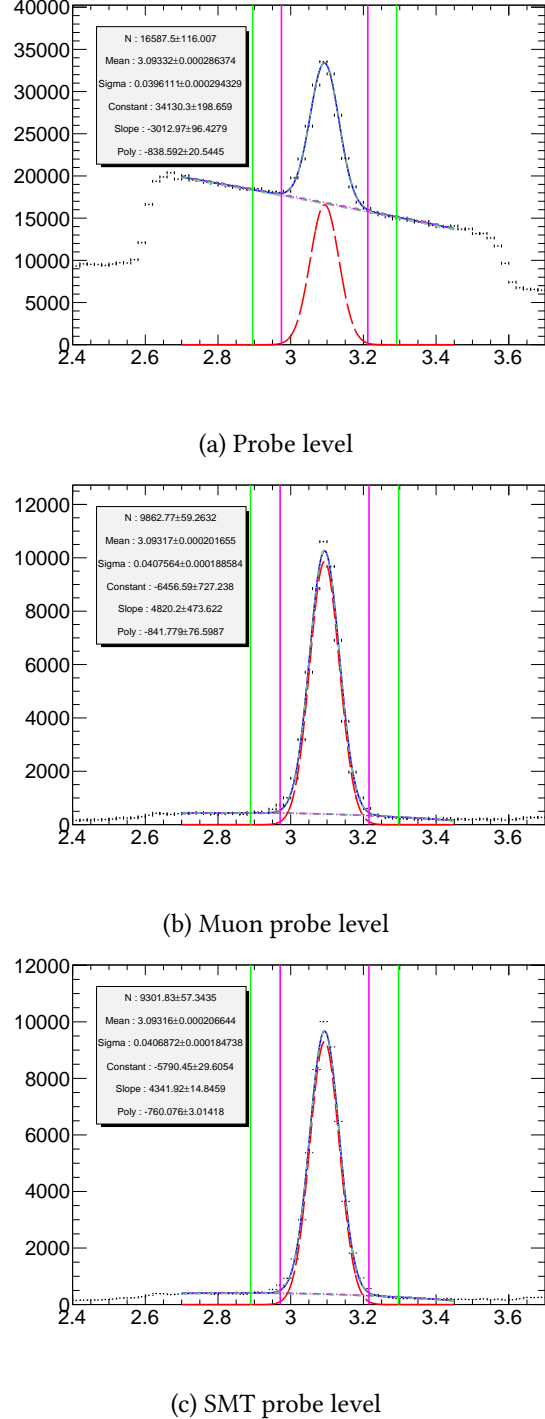


Figure 5.4: Invariant mass distributions of tag and probe pairs at a) probe, b) muon probe and c) SMT level in collision data for probes in barrel A with a p_T of 5 to 6 GeV. Note the components of the fit, the variations on the background and the 3σ and 5σ integration windows used for systematics. Fit parameters are shown with uncertainties.

¹¹⁶⁶ the entire η and p_T range examined (Table 5.4).

p_T range [GeV]	Scale Factor in				
Side A	Crack	Barrel	Transition	Endcap	Forward
4–5	0.974 ± 0.009	0.981 ± 0.003	0.987 ± 0.007	0.981 ± 0.003	0.991 ± 0.005
5–6	0.996 ± 0.008	0.983 ± 0.003	0.987 ± 0.008	0.988 ± 0.004	0.980 ± 0.006
6–7	0.990 ± 0.009	0.984 ± 0.003	0.960 ± 0.010	0.984 ± 0.005	0.981 ± 0.006
7–8	0.966 ± 0.013	0.987 ± 0.004	0.978 ± 0.008	0.990 ± 0.006	0.982 ± 0.007
8–10	0.983 ± 0.011	0.981 ± 0.003	1.005 ± 0.009	0.988 ± 0.005	0.954 ± 0.008
10–12	0.928 ± 0.019	0.979 ± 0.004	1.002 ± 0.009	0.991 ± 0.006	0.984 ± 0.011
Side C	Crack	Barrel	Transition	Endcap	Forward
4–5	0.984 ± 0.008	0.978 ± 0.003	0.992 ± 0.007	0.979 ± 0.003	1.005 ± 0.006
5–6	0.992 ± 0.007	0.991 ± 0.002	0.982 ± 0.009	0.986 ± 0.004	1.012 ± 0.007
6–7	0.989 ± 0.008	0.981 ± 0.003	0.980 ± 0.008	0.990 ± 0.005	1.003 ± 0.010
7–8	0.931 ± 0.017	0.983 ± 0.003	0.970 ± 0.053	0.985 ± 0.006	1.047 ± 0.010
8–10	0.981 ± 0.017	0.987 ± 0.003	0.968 ± 0.009	0.990 ± 0.005	1.100 ± 0.008
10–12	0.974 ± 0.015	0.976 ± 0.004	0.970 ± 0.011	1.002 ± 0.006	1.083 ± 0.010

Table 5.4: Data/MC Scale Factors for 2011 Data in all five regions of the detector as a function of p_T . The uncertainties include systematic and statistical components as described in [10].

¹¹⁶⁷ 5.3.2 Efficiency Binning

¹¹⁶⁸ The efficiencies are measured with respect to pseudorapidity and across the $|\eta|$ range of the
¹¹⁶⁹ ATLAS detector in regions defined in Table 5.5. The binning in other variables is determined
¹¹⁷⁰ by the amount of statistics available to allow for the fitting procedure to produce good and
¹¹⁷¹ stable results. The chosen p_T binning is shown in Table 5.6.

¹¹⁷² 5.4 Results

¹¹⁷³ The reconstruction and χ^2_{match} efficiencies are presented in the following pages as a function of
¹¹⁷⁴ η , ϕ and p_T . Firstly, the STACO CB reconstruction efficiencies and scale factors as measured in
¹¹⁷⁵ side A and C of the detector are shown in Figure 5.5 and Figure 5.6 respectively. The efficiencies
¹¹⁷⁶ exhibit a strong dependence on transverse momentum and pseudorapidity.

Name	$ \eta $ range
Crack	0.0–0.1
Barrel	0.1–1.1
Transition	1.1–1.3
Endcap	1.3–2.0
Forward	2.0–2.5

Table 5.5: Pseudorapidity regions of the ATLAS detector.

1177 The reconstruction efficiency for muons in the crack region appears to suffer from low
 1178 statistics particularly in the high- p_T range, this is expected due to the MS being only partially
 1179 equipped in the region around $\eta = 0$. Additionally, in the transition region the MS coverage
 1180 in ϕ is not uniform due to some chambers not being installed.

1181 It is important to note that the nominal calibration of the reconstruction efficiency within
 1182 ATLAS is performed on $Z \rightarrow \mu\mu$ due to the smaller uncertainty using high- p_T muons. The SF
 1183 for low- p_T are then obtained by extrapolating back into the low momentum range.

1184 The χ^2_{match} efficiency exhibits an asymmetric dependence on the muon probe pseudora-
 1185 pidity, but no dependence on the azimuthal angle ϕ (Figure 5.7). As expected there is a strong
 1186 dependence on the transverse momentum of the muon probe (Figure 5.8). As in the 2011 anal-
 1187 ysis it was decided to bin the SF as a function of p_T and η , distinguishing between side A and
 1188 C of the detector. The scale factor and efficiency distributions are presented in the next pages.

The SMT scale factors and their total uncertainties are summarized in Table 5.6. As an example of the typical uncertainties obtained, the SMT efficiencies measured for muon probes with p_T in the range 5–6 GeV in the positive barrel region are

$$\epsilon_{\text{Data}} = (94.15 \pm 0.32 \text{ (bkg.)} \pm 0.02 \text{ (sig.)} \pm 0.10 \text{ (stat.)})\%$$

$$\epsilon_{\text{MC}} = (89.01 \pm 0.01 \text{ (bkg.)} \pm 0.01 \text{ (sig.)} \pm 0.07 \text{ (stat.)})\%$$

1189 As expected, the background uncertainty dominates in collision data while in simulation it
 1190 represents the smallest source of uncertainty. The width of the J/ψ peak increases for forward
 1191 probes, overwhelming the background distribution delimited by the trigger “shoulders”. This
 1192 is reflected in increased fit parameter uncertainties and thus a larger background uncertainty.

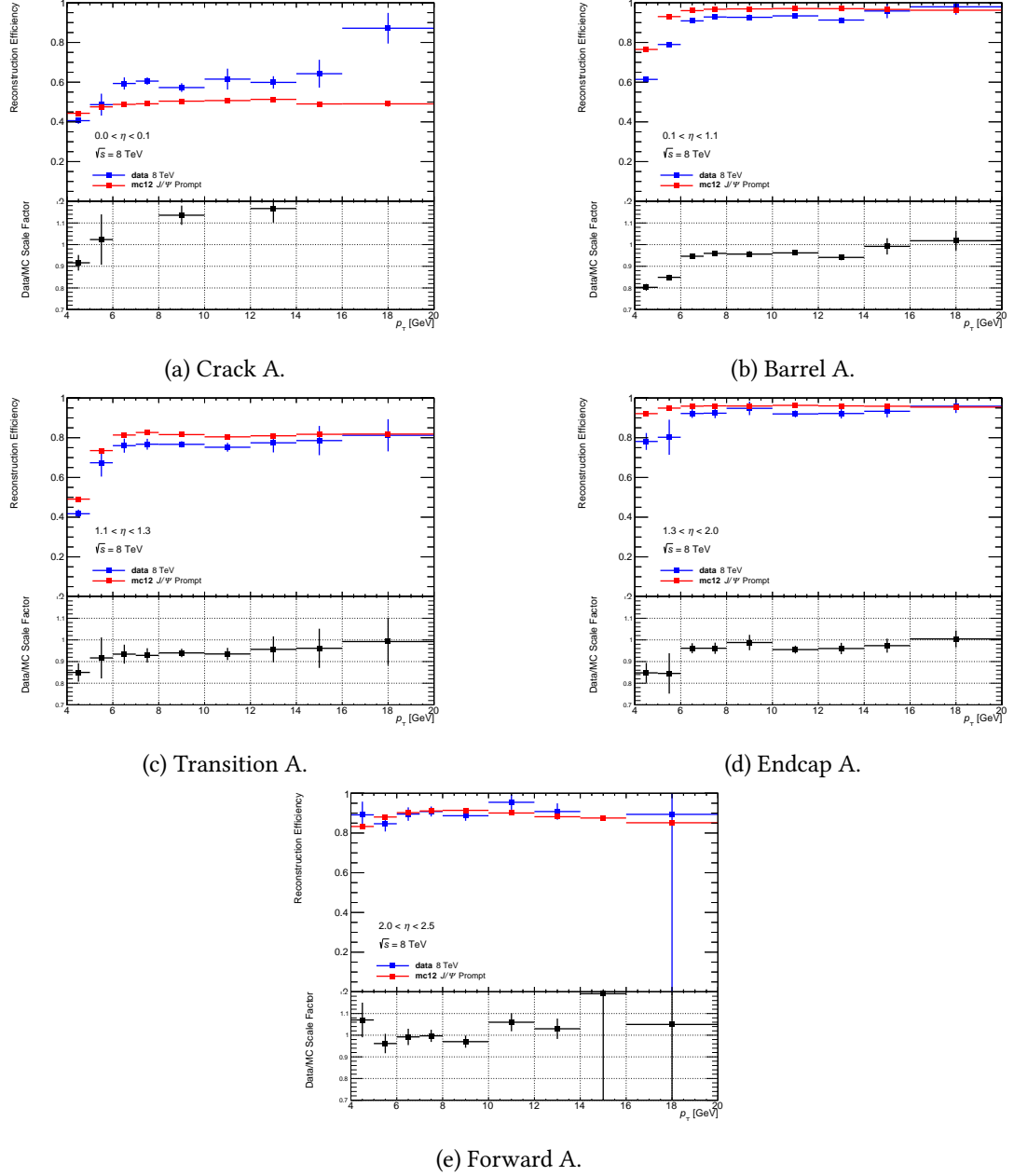


Figure 5.5: Distribution of STACO CB reconstruction efficiencies and scale factor in side A of the detector for all detector regions.

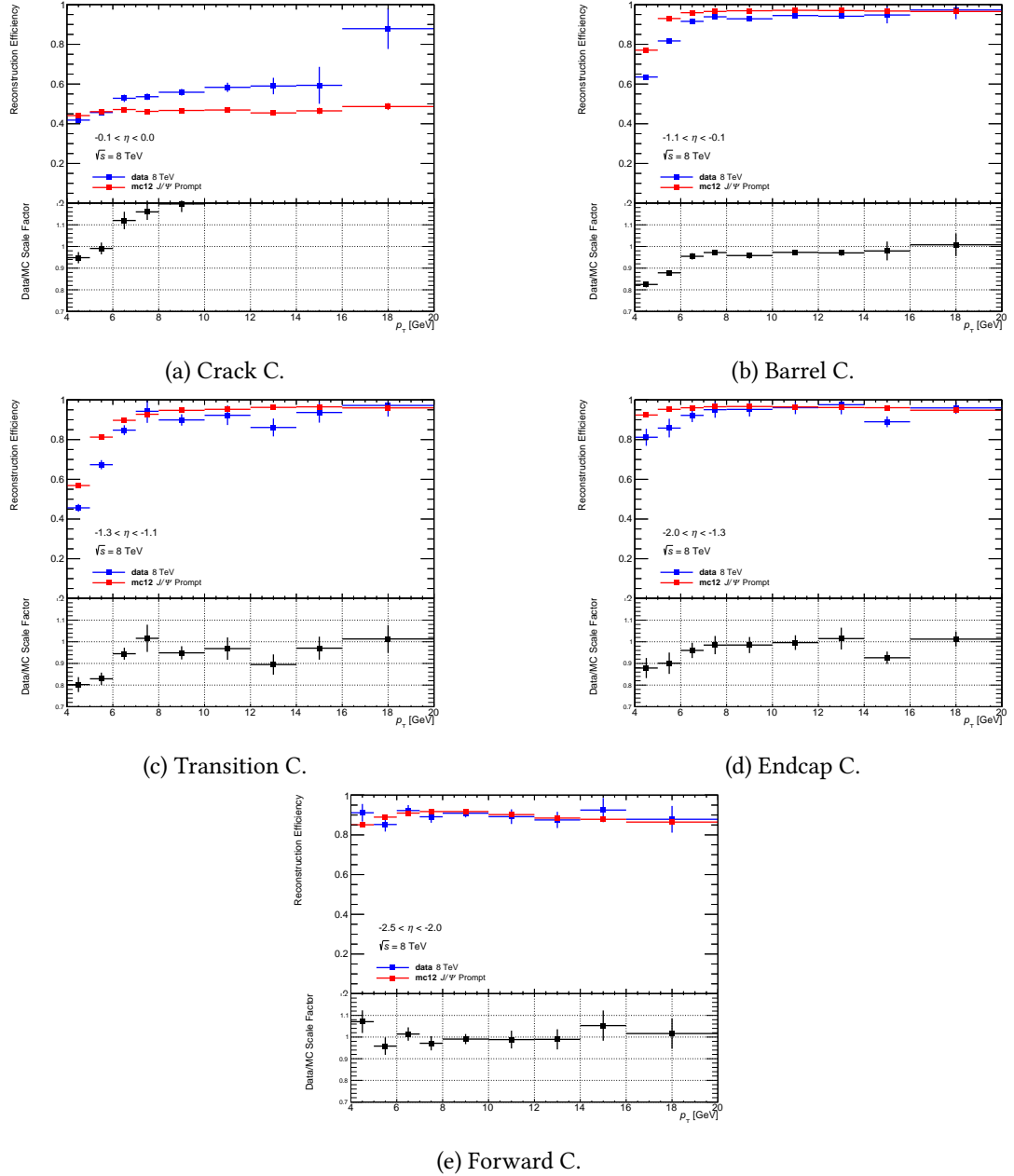
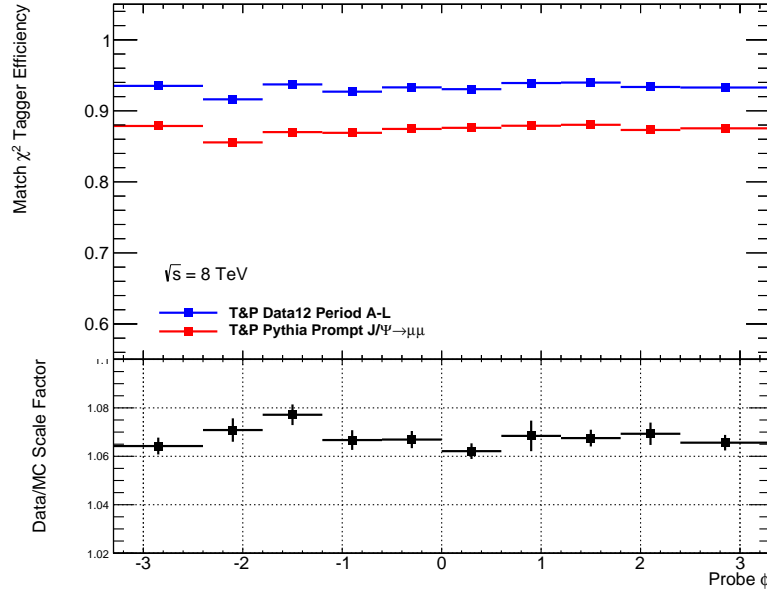
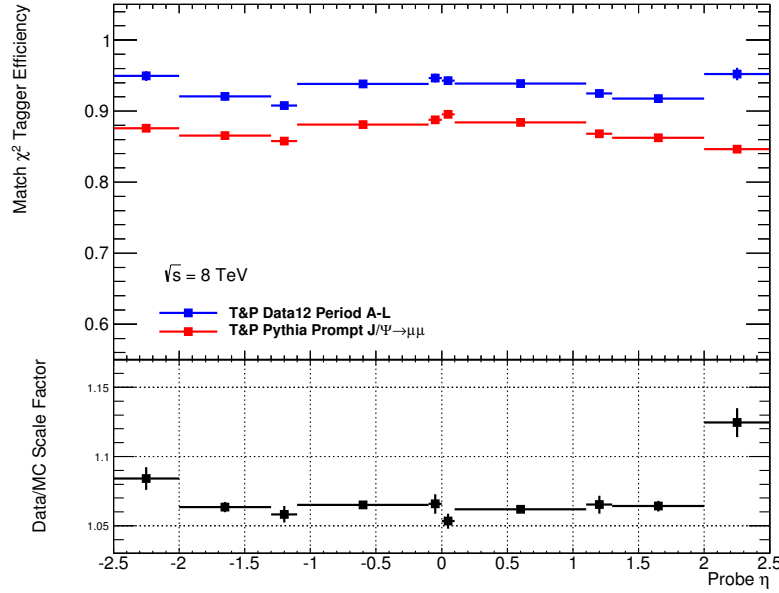


Figure 5.6: Distribution of STACO CB reconstruction efficiencies and scale factor in side C of the detector for all detector regions.



(a) χ^2_{match} efficiency and scale factor as a function the pseudorapidity ϕ of the probe muon.



(b) χ^2_{match} efficiency and scale factor as a function of the pseudorapidity η of the probe muon.

Figure 5.7: Distribution of the χ^2_{match} efficiencies and scale factor with respect to the (a) azimuthal angle ϕ and (b) the pseudorapidity η of the muon probe passing the SMT requirements.

p_T range [GeV]		Scale Factor in				
Side A		Crack	Barrel	Transition	Endcap	Forward
4–5		1.051 ± 0.014	1.053 ± 0.001	1.045 ± 0.005	1.059 ± 0.002	1.088 ± 0.002
5–6		1.051 ± 0.005	1.058 ± 0.001	1.057 ± 0.005	1.062 ± 0.010	1.106 ± 0.003
6–7		1.068 ± 0.006	1.066 ± 0.001	1.069 ± 0.004	1.066 ± 0.002	1.132 ± 0.003
7–8		1.061 ± 0.006	1.063 ± 0.001	1.065 ± 0.004	1.062 ± 0.002	1.142 ± 0.003
8–10		1.061 ± 0.016	1.063 ± 0.001	1.068 ± 0.004	1.063 ± 0.002	1.161 ± 0.003
10–12		1.057 ± 0.024	1.071 ± 0.006	1.062 ± 0.007	1.060 ± 0.015	1.171 ± 0.006
12–14		1.059 ± 0.016	1.062 ± 0.003	1.070 ± 0.010	1.057 ± 0.020	1.178 ± 0.012
14–16		1.043 ± 0.068	1.069 ± 0.013	1.076 ± 0.043	1.069 ± 0.006	1.204 ± 0.013
16–20		1.027 ± 0.077	1.077 ± 0.006	1.112 ± 0.019	1.067 ± 0.004	1.208 ± 0.009
Side C		Crack	Barrel	Transition	Endcap	Forward
4–5		1.044 ± 0.014	1.055 ± 0.001	1.053 ± 0.004	1.056 ± 0.002	1.064 ± 0.005
5–6		1.069 ± 0.005	1.057 ± 0.001	1.050 ± 0.015	1.061 ± 0.008	1.083 ± 0.003
6–7		1.080 ± 0.005	1.068 ± 0.004	1.065 ± 0.004	1.065 ± 0.002	1.095 ± 0.003
7–8		1.064 ± 0.017	1.068 ± 0.005	1.061 ± 0.005	1.066 ± 0.002	1.100 ± 0.004
8–10		1.070 ± 0.007	1.067 ± 0.004	1.054 ± 0.005	1.061 ± 0.002	1.101 ± 0.003
10–12		1.089 ± 0.010	1.073 ± 0.003	1.083 ± 0.022	1.062 ± 0.003	1.107 ± 0.006
12–14		1.095 ± 0.015	1.069 ± 0.009	1.063 ± 0.028	1.049 ± 0.005	1.114 ± 0.008
14–16		1.059 ± 0.032	1.076 ± 0.006	1.085 ± 0.014	1.061 ± 0.006	1.107 ± 0.013
16–20		1.109 ± 0.032	1.088 ± 0.003	1.096 ± 0.021	1.050 ± 0.004	1.120 ± 0.009

Table 5.6: Data/MC Scale Factors for 2012 Data in all five regions of the detector as a function of p_T . The uncertainties include systematic and statistical components as described in Section 5.2.1.

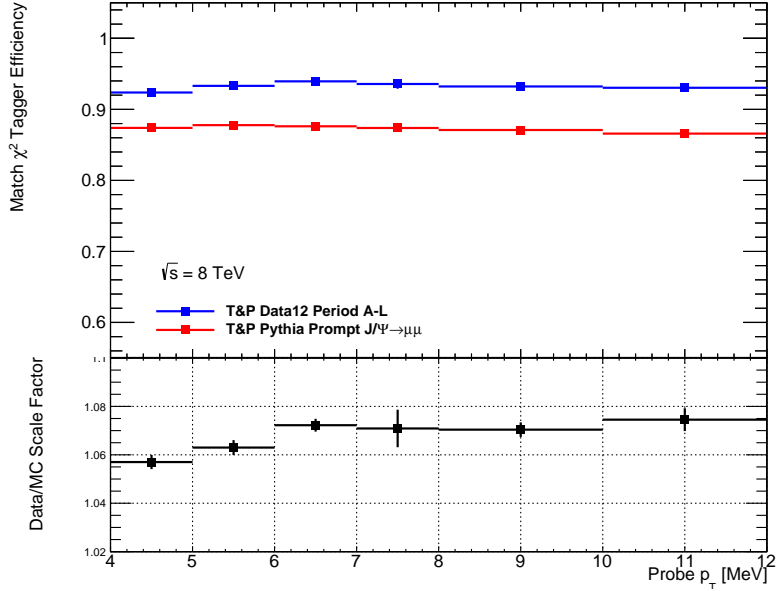


Figure 5.8: Distribution of the χ^2_{match} efficiencies and scale factor with respect to the transverse momentum of the muon probe passing the SMT requirements.

1193 Isolation dependence

1194 The muons from J/ψ used in this calibration are produced in isolation, meaning there is very
1195 little energetic activity surrounding them in the detector. In contrast muons from semileptonic
1196 decay of b -quarks in $t\bar{t}$ events are produced amongst the numerous components of the b -jets.
1197 Thus it is important to ensure that the performance of the χ^2_{match} tagger is not affected by the
1198 isolation of the muon for a calibration on J/ψ events to be applicable. In this calibration, as in
1199 the 2011 analysis, the nine isolation variables are considered. These are defined in Section 4.4.1.

1200 The dependence on the isolation variables is measured in a range dictated by the available
1201 statistics. The isolated nature of muons in J/ψ events limits the number of muons available
1202 at higher $p_T/\text{et}/\text{nucone}$ values. This is particularly true of the MC simulation compared to data
1203 which contains non-isolated muons. As in the 2011 analysis there appears to be no dependence
1204 on any of the isolation variables examined (Figures 5.14, 5.15 and 5.16).

1205 Dependence on d_0

1206 The dependence on the impact parameter d_0 was examined and no direct dependence is ob-
1207 served. The scale factor shows no structure with respect to d_0 when binned in p_T (Figure 5.17).

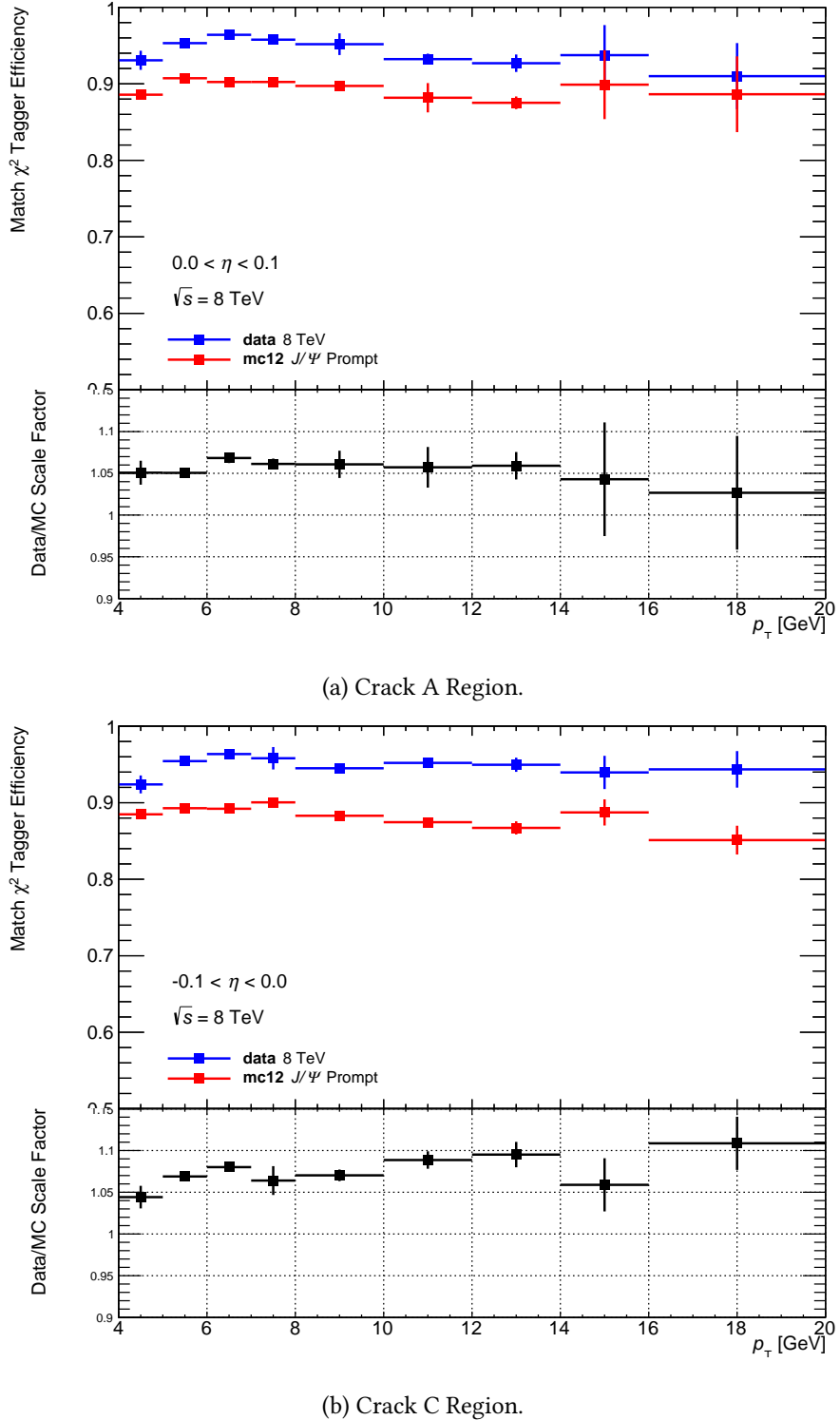


Figure 5.9: χ^2_{match} efficiencies and scale factors in the crack region of the detector for side (a) A and (b) C.

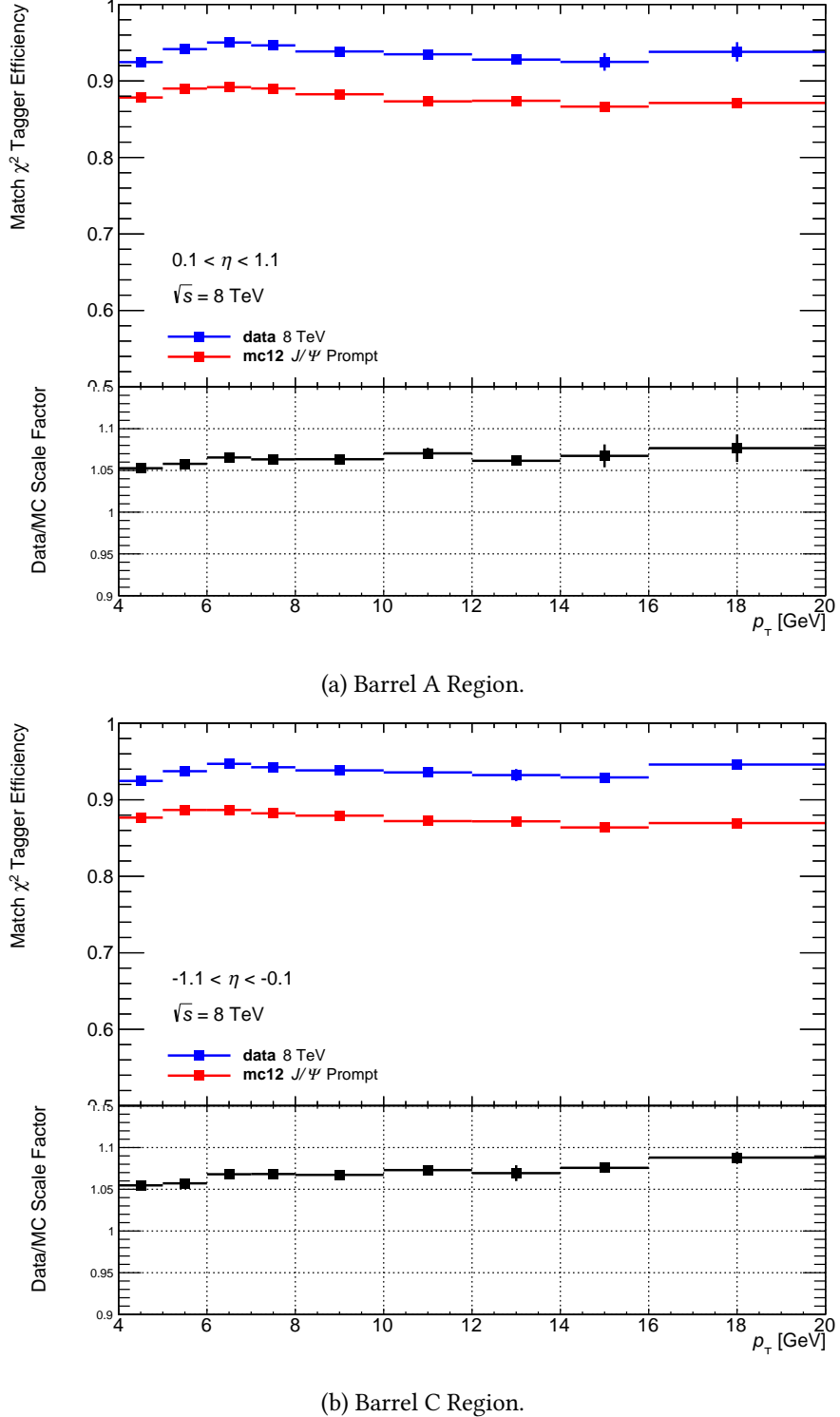
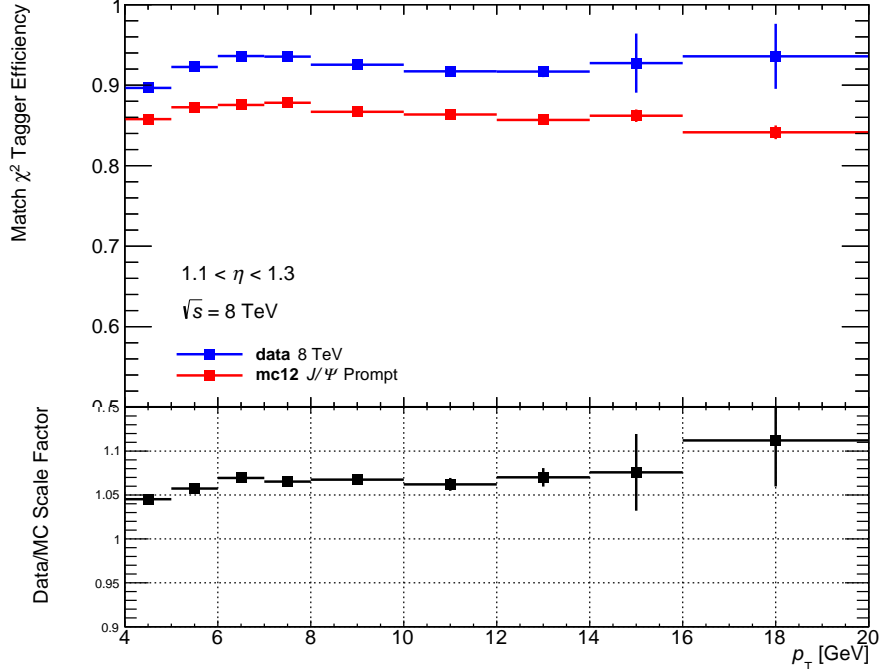
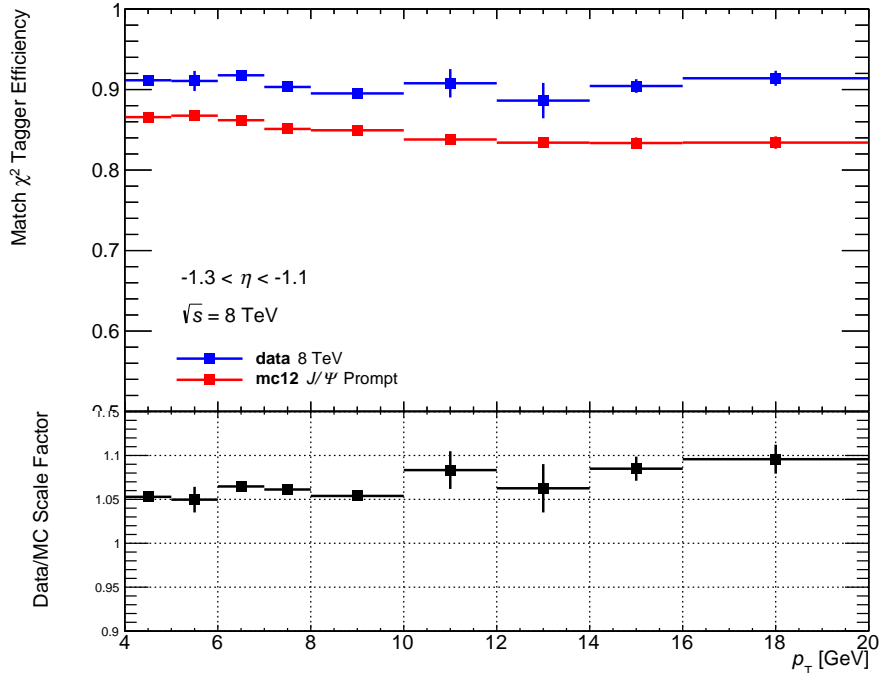


Figure 5.10: χ^2_{match} efficiencies and scale factors in the barrel region of the detector for side (a) A and (b) C.



(a) Transition A Region.



(b) Transition C Region.

Figure 5.11: χ^2_{match} efficiencies and scale factors in the transition region of the detector for side (a) A and (b) C.

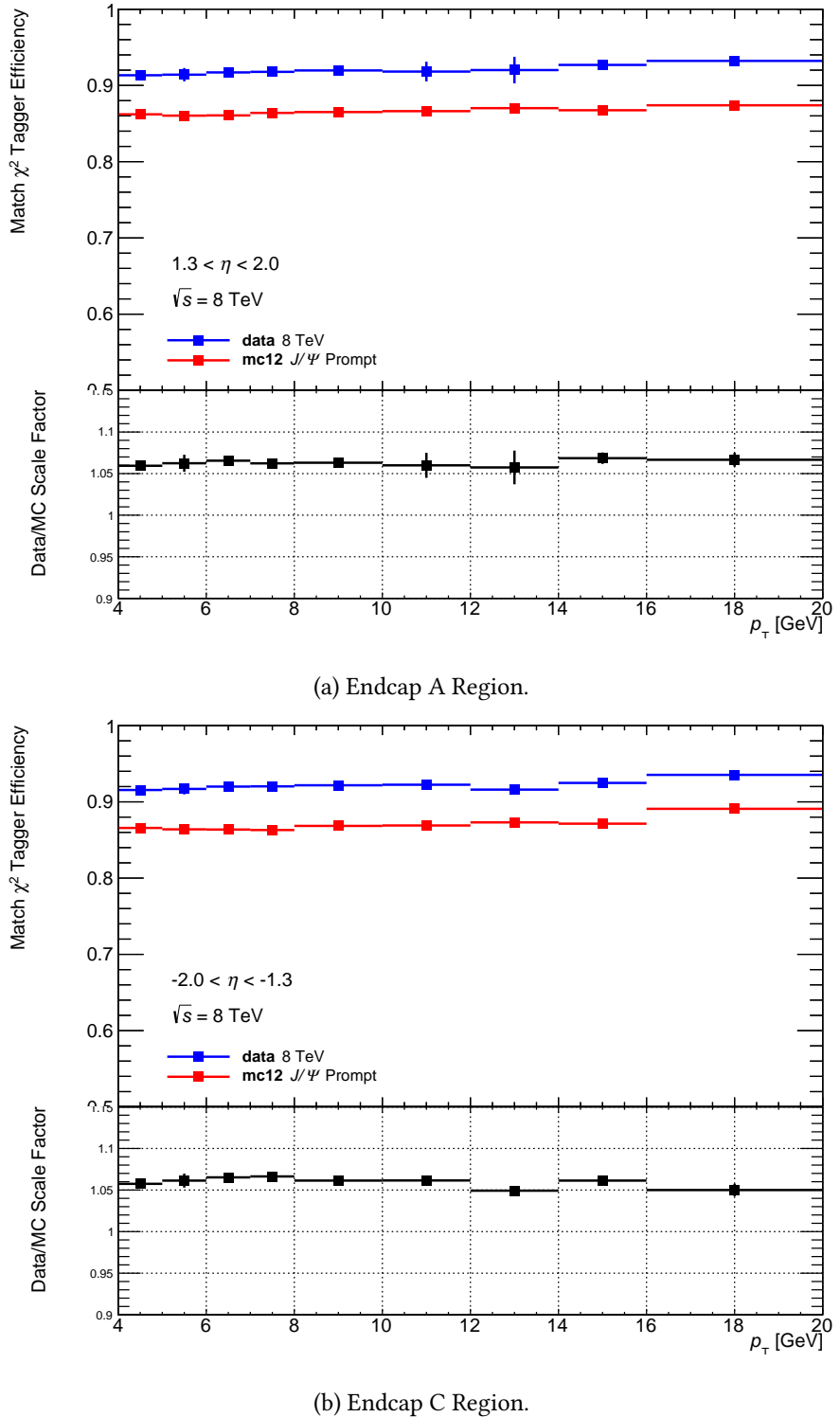


Figure 5.12: χ^2_{match} efficiencies and scale factors in the endcap region of the detector for side (a) A and (b) C.

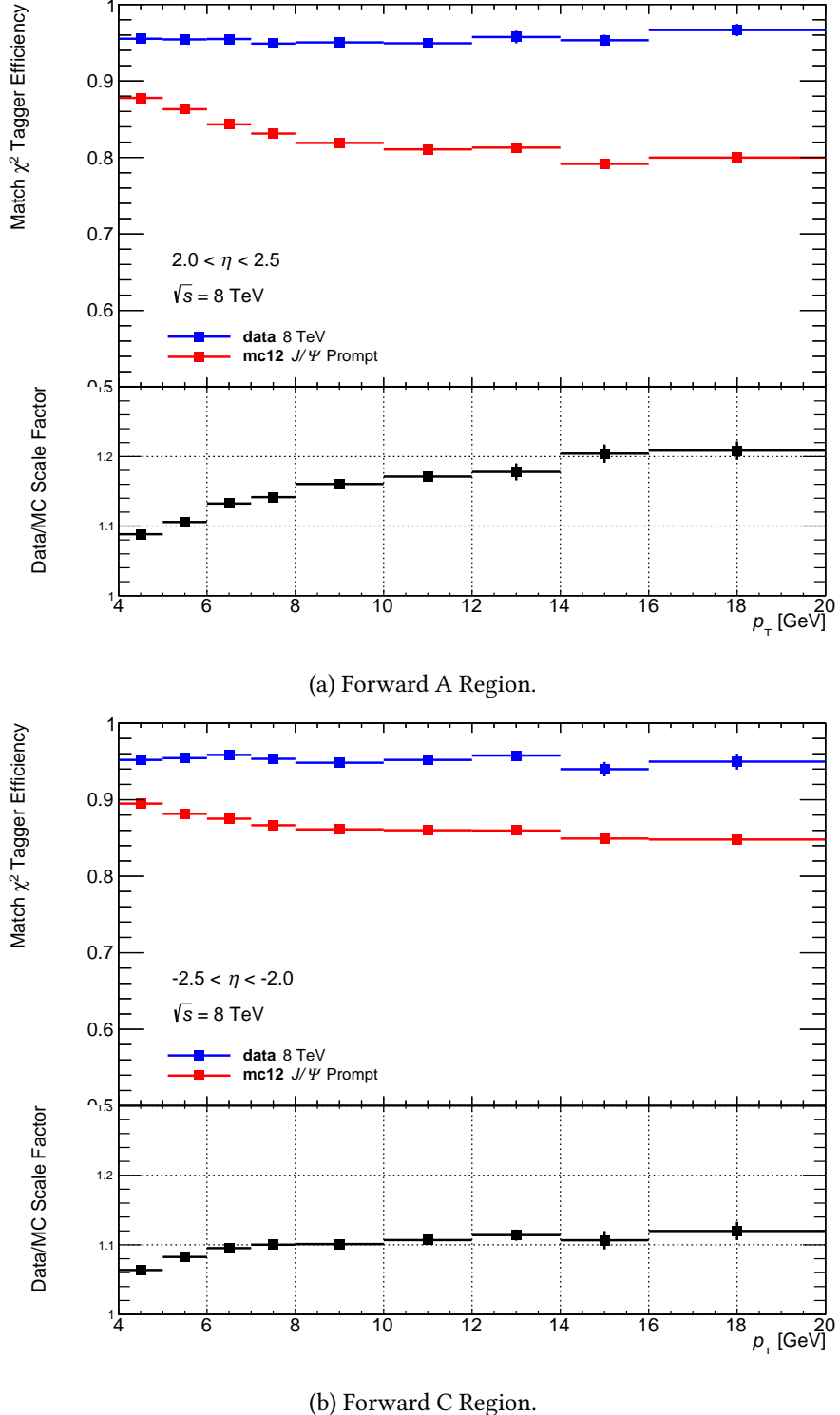


Figure 5.13: χ^2_{match} efficiencies and scale factors in the forward region of the detector for side (a) A and (b) C.

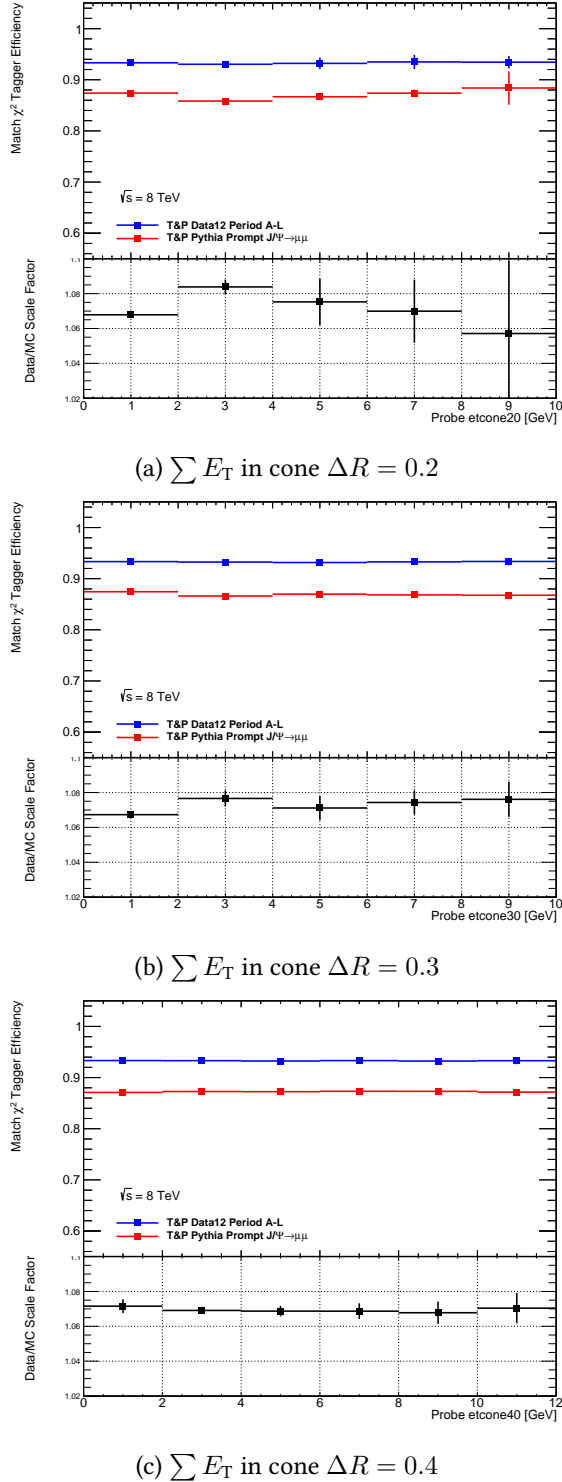


Figure 5.14: χ^2_{Dof} efficiencies and scale factor with respect to $\sum E_T$ for a muon probe that passes the SMT requirements.

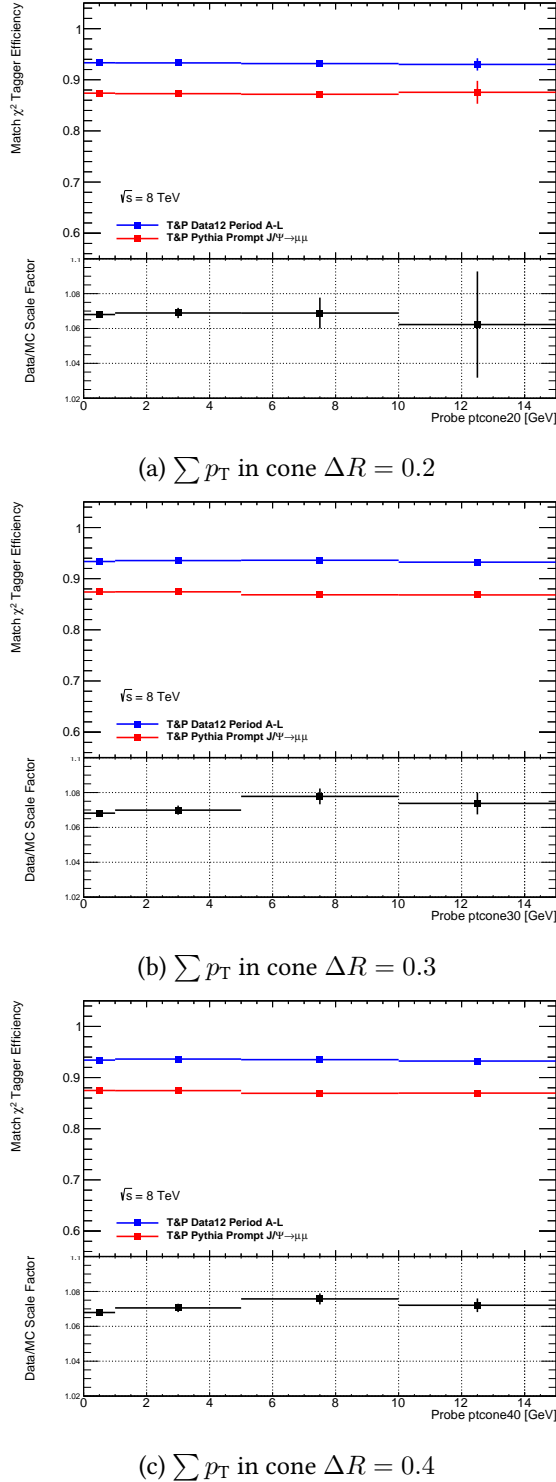


Figure 5.15: χ^2_{DoF} efficiencies and scale factor with respect to $\sum p_T$ for a muon probe that passes the SMT requirements.

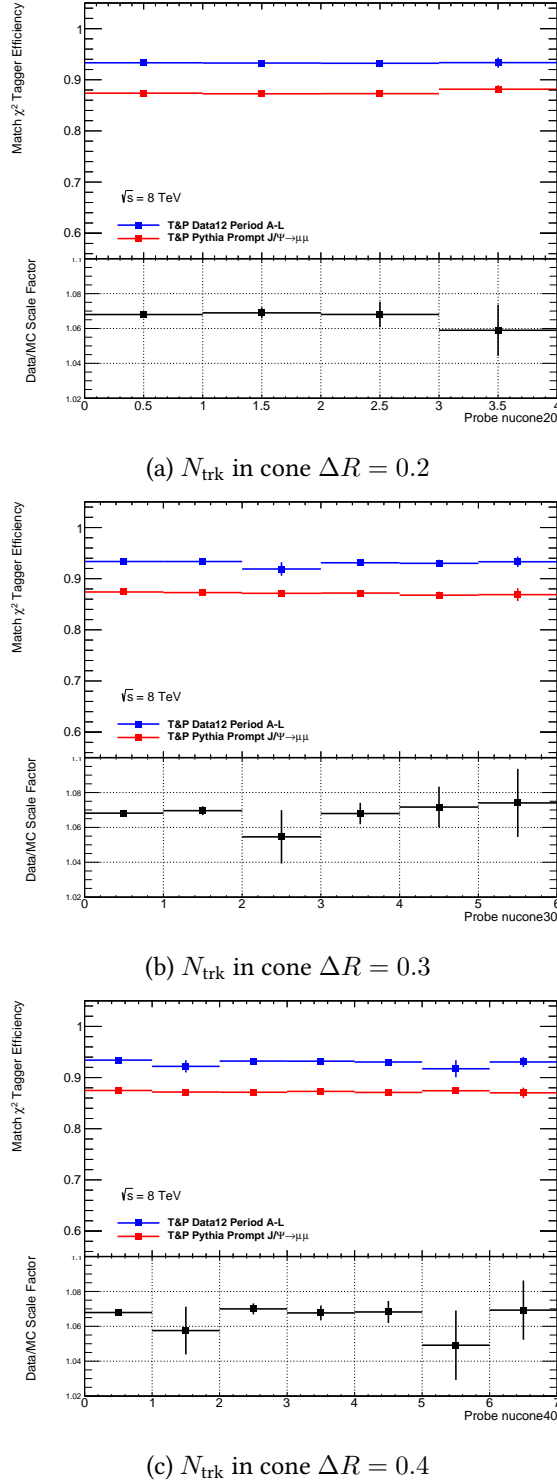


Figure 5.16: χ^2_{DoF} efficiencies and scale factor with to N_{tracks} for a muon probe that passes the SMT requirements.

1208 Since the scale factors are binned in η and p_T , the correlation between d_0 and p_T is taken into
1209 account.

1210 **5.5 Scale Factor Discrepancy**

1211 There is a discrepancy between the 2011 and 2012 scale factors. The SFs in the 2011 analysis
1212 do not deviate substantially from unity, while the 2012 SF deviate as much as 15 % depending
1213 on the region of phase-space. The efficiency measured in the 2012 collision-data appears to
1214 be consistent with the 2011 result, however in simulation the efficiency is measured to be
1215 lower. Thus the difference in SF appears to come from a mismodelling of the χ^2_{DoF} variable. A
1216 number of factors can contribute to this type of mismodelling, such as the detector alignment
1217 and detector material description used in the detector simulation. Both of these can result in
1218 mismodelling of the kinematic variables that make up the χ^2_{DoF} variable.

1219 In order to find the source of the discrepancy the components of the χ^2_{DoF} variable were
1220 examined. The *pull* of a kinematic variable is defined here as

$$X_{\text{pull}} = \frac{X^{\text{ID}} - X^{\text{ME}}}{\sqrt{\sigma_{X^{\text{ID}}}^2 + \sigma_{X^{\text{ME}}}^2}} \quad (5.11)$$

1221 where X is any of the five kinematic components of χ^2_{match} , and σ is the uncertainty on that
1222 variable. The pulls are shown in terms of the azimuthal angle, the polar angle, the longitudinal
1223 and transverse impact parameters and the charge over momentum (q/p) of the muon probe in
1224 in Figure 5.18. The transverse momentum is related to the q/p by $p_T = |1/(q/p)| \sin(\theta)$ and
1225 the pseudorapidity is defined in terms of the angle θ in Section ???. The momentum appears
1226 to be well modelled in MC as can be seen from the pull distribution. In contrast the angular
1227 variable seem to exhibit the worst agreement.

1228 A study to test the effects of different alignment profiles was carried out. Several samples
1229 with different alignment profiles were compared to a small sample of 8 TeV collision data from
1230 a single run. These include the nominal prompt J/ψ sample used in this calibration, the J/ψ
1231 sample used for the 2011 calibration, a $Z \rightarrow \mu\mu$ sample where the detector is perfectly
1232 aligned, a 2011 $Z \rightarrow \mu\mu$ sample with an update detector geometry description and a $Z \rightarrow \mu\mu$
1233 sample with so-called *smeared A-lines*. The smeared alignment is produced by distorting the

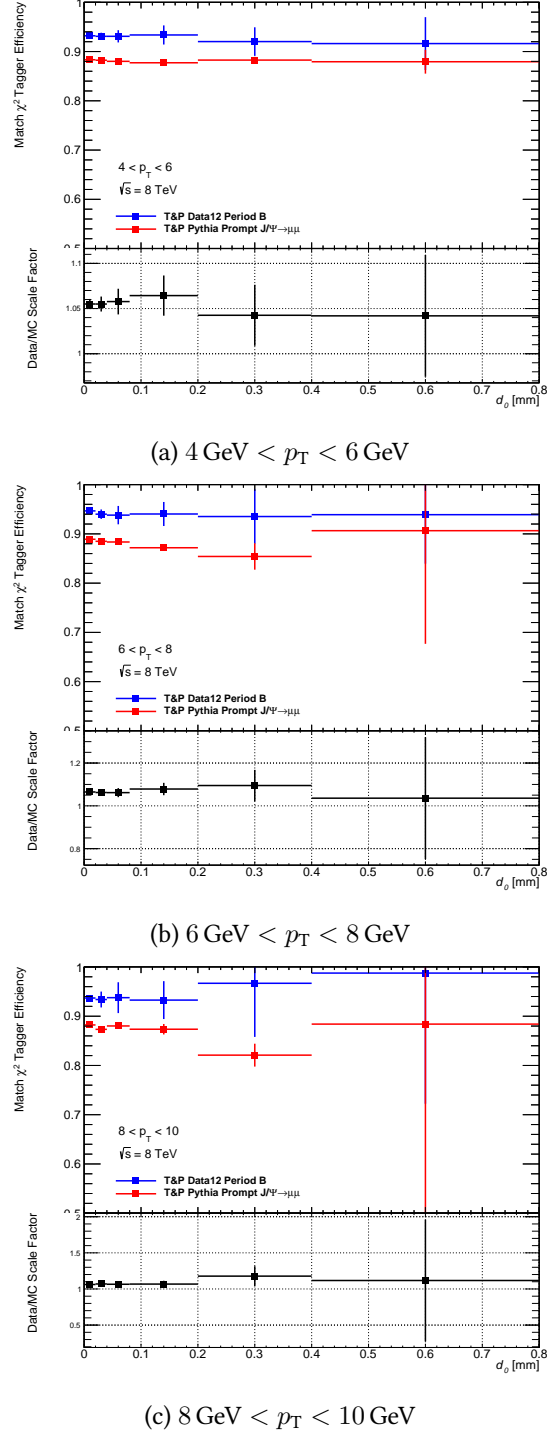


Figure 5.17: Distribution of the χ^2_{match} efficiencies and scale factor with respect to impact parameter d_0 for muon probes with p_T in the ranges (a) 4–6 GeV, (b) 6–8 GeV and (c) 8–10 GeV. The measurement was carried out only on Period B of 2012 ATLAS collision data.

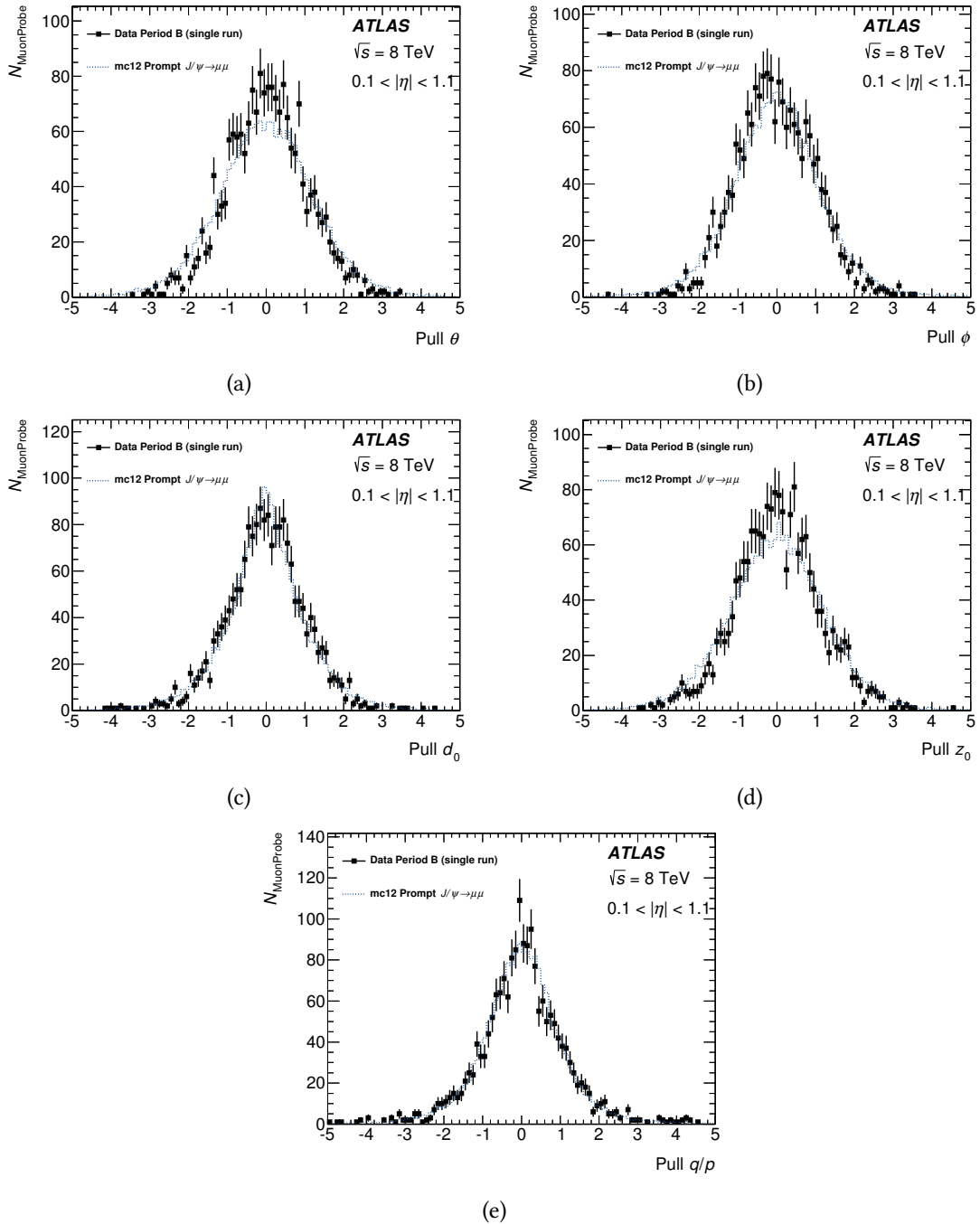


Figure 5.18: Distribution of pull (see 5.11) of components of χ^2_{DoF} as measured in the ID for muon probes in the barrel region for collision data (squares) and prompt J/ψ simulation (dotted). Shown are (a) θ , (b) ϕ , (c) d_0 , (d) z_0 and (e) q/p . These distributions are based on smaller samples and are normalized to unit area.

Sample	Pseudo-efficiency [%]
Data $\sqrt{s} = 8$ TeV 2012	94.35 ± 0.02
Prompt J/ψ 2012	95.22 ± 0.02
Prompt J/ψ 2011	90.59 ± 0.02
Z Smeared A-lines 2012	91.37 ± 0.03
Z Ideal Alignment 2012	91.43 ± 0.03
Z New Geometry 2011	92.44 ± 0.03

Table 5.7: Summary of χ^2_{match} tagger efficiencies as measured in all tested samples

1234 ideal alignment sample within the current measured alignment uncertainties. This procedure
 1235 is not designed to perfectly represent the details in the misalignment of the ATLAS detector,
 1236 but rather simulates a detector which is as well aligned as the real detector. These two profiles
 1237 are compared in small samples of $Z \rightarrow \mu\mu$ events.

1238 A sample of good reconstructed muons is constructed by matching STACO combined
 1239 muons to truth muons from Z or J/ψ . The χ^2_{DoF} distribution of these muons are then compared
 1240 in coarse p_T and η bins.

1241 As expected, the alignment profile does have an effect on the χ^2_{DoF} distribution, particularly
 1242 in the lower end (Figure 5.19). However, this effect is not sufficiently large to account for the
 1243 entirety discrepancy between simulation and data. A pseudo-efficiency of the χ^2_{match} selection
 1244 is obtained by taking the area under the curve below 3.2 and comparing it to the total area
 1245 under the curve. The results are summarized in Table 5.7.

1246 5.5.1 Future developments

1247 As can be seen from Figure 5.18e, the momentum appears to be well modelled in both data and
 1248 simulation. As a result an alternative variable known as the momentum imbalance is currently
 1249 being studied. The momentum imbalance is defined as

$$\text{Mom. Imb.} = \frac{p^{\text{ID}} - p^{\text{ME}}}{p^{\text{ID}}} \quad (5.12)$$

1250 where p^{ID} is the momentum of the muon track as measured in the ID and p^{ME} is measured in
 1251 the MS extrapolated back to the primary vertex. This extrapolation takes into account the loss

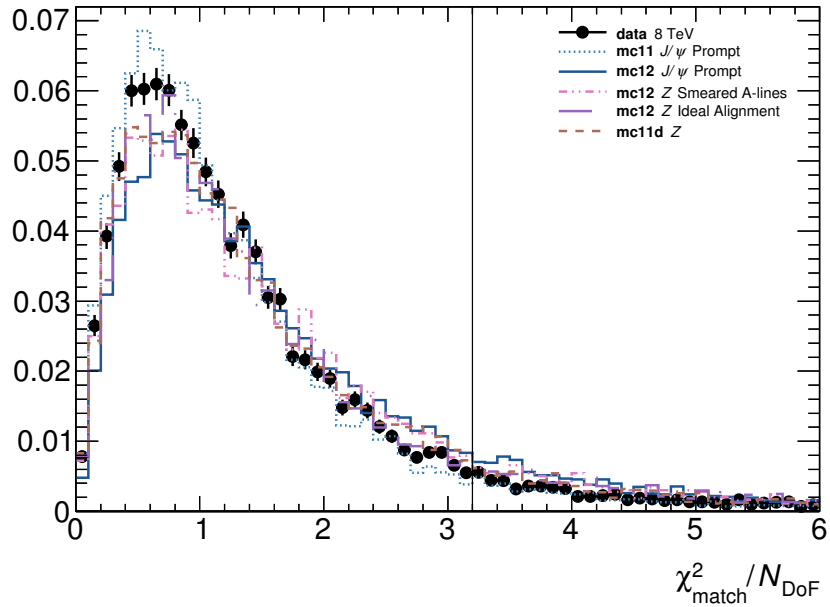


Figure 5.19: Distribution of χ^2_{DoF} of STACO CB muons from $Z \rightarrow \mu\mu$ with ideal detector alignment (dot-dashed), $Z \rightarrow \mu\mu$ with smeared alignment (solid), $J/\psi \rightarrow \mu\mu$ with smeared alignment at $\sqrt{s} = 8$ TeV (dotted) and $J/\psi \rightarrow \mu\mu$ with smeared at $\sqrt{s} = 7$ TeV as used in the 2011 analysis (dot-dashed). Distributions are normalized to unit area.

Sample	Pseudo-efficiency [%]
Data $\sqrt{s} = 8$ TeV 2012	89.83 ± 0.03
Prompt J/ψ 2012	93.57 ± 0.02
Prompt J/ψ 2011	92.81 ± 0.02
Z Smeared A-lines 2012	94.19 ± 0.03
Z Ideal Alignment 2012	94.46 ± 0.02
Z New Geometry 2011	94.20 ± 0.03

Table 5.8: Summary of momentum imbalance efficiencies as measured in all tested samples

1252 of momentum that occurs when the muon traverses through the detector material.

1253 The momentum imbalance distribution for the aforementioned samples is shown in Fig-
 1254 ure 5.20. Measurements of the efficiency using momentum imbalance have been carried out
 1255 and the simulation appears to model collision data well with respect to this variable. The se-
 1256 lection using momentum imbalance requires $Mom. Imb. < 0.1$ as background sources tend to
 1257 peak above threshold. The pseudo-efficiency for this selection as measured in the samples are
 1258 shown in Table The momentum imbalance at this operating point has a similar performance
 1259 to the χ^2_{match} version of the tagger in terms of efficiency and fake rate.

1260 In addition, a comparison of the reconstruction efficiencies with those obtained by mem-
 1261 bers of the MCP group was carried out. As a result the pairing selection has been loosened to
 1262 allow for multiple probes per tag. This increases the statistics available for invariant mass fit-
 1263 ting and more importantly, has increased the reconstruction efficiency across the η - p_T phase
 1264 space. It is possible for the correct probe to be further away from the tag in z_0 than other
 1265 spurious tracks. By forcing the selection of the closest ID track in z_0 , the sample of probes is
 1266 contaminated with non-muons resulting in a lower than expected reconstruction efficiency.

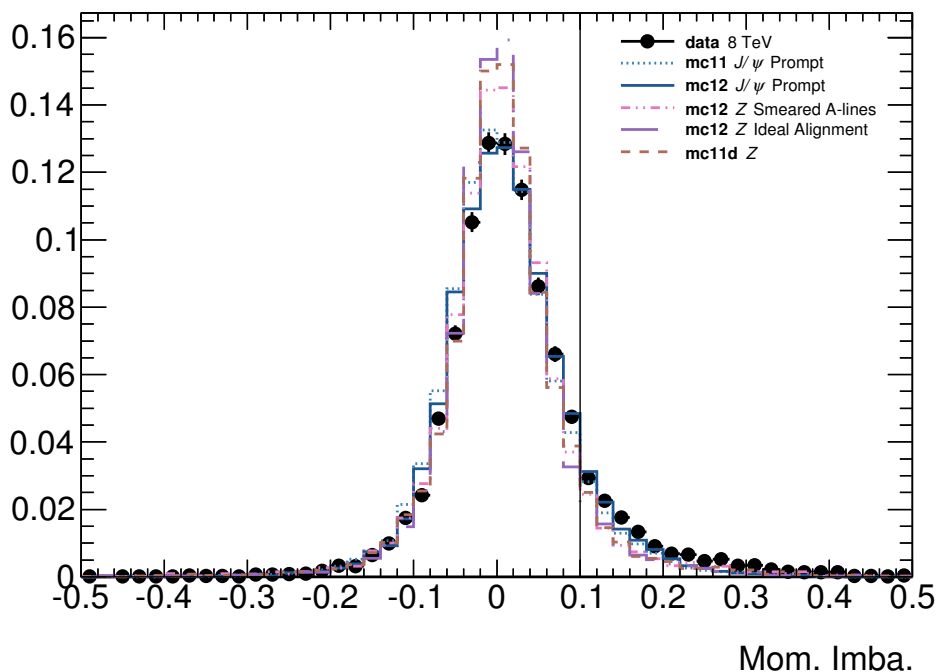


Figure 5.20: Distribution of the momentum imbalance of STACO CB muons from $Z \rightarrow \mu\mu$ with ideal detector alignment (double dot-dashed), $Z \rightarrow \mu\mu$ with smeared alignment (solid), $J/\psi \rightarrow \mu\mu$ with smeared alignment at $\sqrt{s} = 8$ TeV (dotted) and $J/\psi \rightarrow \mu\mu$ with smeared at $\sqrt{s} = 7$ TeV as used in the 2011 analysis (dot-dashed). Distributions are normalized to unit area.

1267 **Chapter 6**

1268 **Measurement of the $t\bar{t}$ cross-section
1269 in the ℓ +jets channel using SMT**

1270 This section describes a $t\bar{t}$ cross-section measurement carried out by the joint RHUL and QMUL
1271 SMT group. Measurement of the $t\bar{t}$ production cross-section is important for many reasons.
1272 First, the value of the $t\bar{t}$ cross-section at various \sqrt{s} ¹ is a powerful test of the SM and pertur-
1273 bative QCD. New physics processes could have a similar final-state signature so any signifi-
1274 cant deviations from the prediction would point to the presence of new physics. Additionally,
1275 $t\bar{t}$ events constitute a background to other analyses such as SUSY searches and Higgs boson
1276 searches and properties studies.

1277 Presented here is a measurement of the top-pair production cross-section at $\sqrt{s} = 7$ TeV
1278 in the lepton plus jets channel, with at least one of the b -quarks in the event decaying semilep-
1279 tonically producing a soft muon. The presence of such a jet is determined by the use of the
1280 χ^2_{match} -based SMT tagger described in Section 4.4.4.

1281 **6.1 Data and Monte Carlo samples**

1282 This measurement is based on collision data recorded by ATLAS in 2011 at the LHC. After
1283 applying quality cuts based on the beam and detector conditions, the dataset contains an inte-
1284 grated luminosity of $(4.66 \pm 0.08) \text{ fb}^{-1}$. Several simulation samples are used in this analysis.
1285 The $t\bar{t}$ signal sample was simulated with MC@NLO v4.01 [57, 58] interfaced to HERWIG [59]

1Production cross-sections depend on the \sqrt{s} of the collision.

Source	Branching Ratio [%] (Ratio to PDG)		
	PDG	HERWIG	PYTHIA
$b \rightarrow \mu$	10.95 ± 0.29	9.57 ± 0.03 1.14 ± 0.03	10.01 ± 0.03 1.09 ± 0.03
$b \rightarrow \tau \rightarrow \mu$	0.42 ± 0.04	0.70 ± 0.02 0.60 ± 0.06	0.67 ± 0.01 0.62 ± 0.06
$b \rightarrow c \rightarrow \mu^+$	8.02 ± 0.19	8.24 ± 0.03 0.97 ± 0.02	8.89 ± 0.03 0.90 ± 0.02
$b \rightarrow \bar{c} \rightarrow \mu^-$	1.60 ± 0.50	2.51 ± 0.02 0.64 ± 0.20	2.66 ± 0.02 0.60 ± 0.19

Table 6.1: List of branching ratios as used in HERWIG and PYTHIA generators compared to the reference PDG values [7].

for parton showering and hadronisation and JIMMY [60] for underlying event simulation. The $W/Z + \text{jets}$ samples were generated using ALPGEN [61] interfaced into HERWIG+JIMMY. The single top samples were generated using MC@NLO interfaced to HERWIG+JIMMY for the s and Wt channels and AcerMC [62] interfaced to PYTHIA [63] for the the t channel. Finally the diboson samples ($WW/WZ/ZZ$) were generated using HERWIG alone.

This analysis is based on the tagging of muons from semileptonic decays of b -quarks. In order to obtain the correct event yields it is important that the simulation used correctly models the inclusive production rate of soft muons and the individual BR for all production chains (Table 4.4). To this end, each event with a soft muon is reweighted such that the BR conforms with the latest measured value as quoted in Ref. [7]. The reference BR and the values used for HERWIG and PYTHIA are shown in Table 6.1.

6.2 Object selection and event selection

The selection criteria used in this analysis are based on the nominal $\sqrt{s} = 7$ TeV selections recommended by the ATLAS top group. Some alterations have been implemented to adapt to the usage of the χ^2_{match} tagger instead of the standard MV1 method for b -jet tagging. Collision and simulation events are required to have fired an inclusive single electron or muon trigger with offline-reconstructed candidates with $p_T > 25$ GeV for electrons and $p_T > 20$ GeV for muons. Electrons are required to have $|\eta| < 2.47$ and not lie within the transition between the barrel and endcap calorimeters ($1.37 < |\eta| < 1.52$). They must satisfy the *tight* identification criteria set as described in Appendix A. Electrons are required to be isolated using cuts on calorimeter

1306 isolation ($E_T^{\text{cone}20}$) and momentum isolation ($p_T^{\text{cone}30}$) as defined in Section 5.4. The cut value
1307 for both is defined such as to maintain an efficiency of 90 %. The isolation requirements are
1308 designed to reduce the amount of multijet background, where reconstructed electrons are not
1309 produced in isolation.

1310 Muon candidates are reconstructed using the MUID combined algorithm, and must lie
1311 within the coverage of ID ($|\eta| < 2.5$). The combined track is obtained from a fit using both
1312 ID and MS information. The muon is required to be isolated in both tracking and calorimeter
1313 isolation with $E_T^{\text{cone}20} < 4 \text{ GeV}$ and $p_T^{\text{cone}30} < 2.5 \text{ GeV}$ and to be well separated from the jet by
1314 at least $\Delta R > 0.4$. Events must contain exactly one “good” muon or one “good” electron.

1315 Jets are reconstructed using the anti- k_t algorithm with a distance parameter $R = 0.4$.
1316 Calorimeter topological clusters at the EM scale are used as inputs to the algorithm and JES
1317 corrections are applied to the resulting jets. In addition, Jets are required to have a $p_T > 25 \text{ GeV}$
1318 and $|\eta| < 2.5$. An additional requirement is applied on the jet vertex fraction (JVF), which is
1319 defined as the sum p_T of all tracks matched to a jet that originated from a given vertex divided
1320 by the sum p_T of all tracks that make up the jet. The JVF is normally defined with respect to the
1321 primary vertex. Jets are required to have a JVF larger than 0.75. Finally, jets within $\Delta R < 0.2$
1322 of an electron are rejected.

1323 In the e +jets analysis, a large amount of missing transverse energy is required ($> 30 \text{ GeV}$)
1324 to account for escaping neutrinos. The transverse mass of the W boson $m_{T,W}$ is reconstructed
1325 from the signal lepton and the missing transverse energy. In the electron channel the measured
1326 $m_{T,W}$ must be larger than 30 GeV . In the μ +jets channel the E_T^{miss} requirement is set at $>$
1327 20 GeV and a triangular cut is performed by requesting that $E_T^{\text{miss}} + m_{T,W} > 60 \text{ GeV}$.

1328 For both channels, a minimum of three “good” jets is required. All events which pass these
1329 selections are labelled as “pretag” events. Pretag events which contain at least one jet tagged
1330 by the SMT algorithm are labelled as “tagged” events. In the μ +jets channel, requirements are
1331 placed on the invariant mass of the soft muon and the signal muon $m_{\mu\mu}$ to remove contribu-
1332 tions from dimuon Υ ($8 \text{ GeV} \leq m_{\mu\mu} \leq 11 \text{ GeV}$) and Z ($80 \text{ GeV} \leq m_{\mu\mu} \leq 100 \text{ GeV}$) decays.
1333 Finally, the signal muon must not be the soft muon ($\Delta R > 0.01$).

1334 The efficiency of the full selection as measured on the $t\bar{t}$ signal sample is 1.42 % in the
1335 e +jets channel and 2.15 % in the μ +jets channel. These efficiencies include both lepton plus
1336 jets and dilepton events with at least three jets and at least one jet tagged by the SMT algorithm.

1337 Acceptance to fully hadronic events is negligible.

1338 **6.3 Background estimation**

1339 Lepton plus jets $t\bar{t}$ events have a varied final state signature that includes a lepton, multiple
1340 jets including b -jets and missing energy. As a result $t\bar{t}$ analyses must take into account many
1341 different types of background: diboson, W +jets, Z +jets, single-top and multijet. W +jets events
1342 (e.g. Figure 6.1a) enter the signal region due to the presence of a real lepton, missing transverse
1343 energy and one or two real b -jets or mistagged LF jets. Gluon emissions can also occur resulting
1344 in additional jets. The W +jets background is estimated using data-driven methods. Z +jets
1345 events (e.g. Figure 6.1b) can pass the selection if one of the two leptons is not identified if, for
1346 example the lepton enters the crack region. This results in an overall imbalance of momentum
1347 interpreted as missing energy. The Z boson can be created in association with a gluon which
1348 result in real b -jets or LF jets that could be mistagged. Diboson production (e.g. Figure 6.1c)
1349 such as WW , ZZ or WZ enters the signal region due to the presence of real leptons, missing
1350 energy (real or from missed leptons) and HF jet or mistagged LF jets.

1351 Multijet events which contain LF and/or b -quarks enter the signal region when they con-
1352 tain a fake lepton which passes the isolation requirement. Fake electrons include both real
1353 electrons: such as those from photon conversions in the detector material and semileptonic
1354 decay of b - and c -quarks, and objects that fake the electron signature such as tracks overlap-
1355 ping with photons and jets with few charged tracks or small amounts of energy deposited in
1356 the hardonic calorimeter.

1357 Fake muon sources include real muons from decay-in-flight of pions or kaons within the
1358 tracking region, and objects that fake the muon signature such as hadrons that do not shower
1359 in the detector material and *punch-through* hadrons from hadronic showers. Additionally, the
1360 semileptonic decay of b - and c -quarks can also produce muons which constitutes a background
1361 to the signal W -muon. However, in this analysis these soft muons are those tagged by the SMT
1362 tagger. A significant amount of fake E_T^{miss} must also be reconstructed for the multijet events to
1363 pass the selection. Missing energy is reconstructed by combining all energy depositions in the
1364 detector, any imbalance is then treated as missing energy. There are numerous sources of fake
1365 E_T^{miss} including uninstrumented sections of the detector, noisy or dead calorimeter cells, mis-

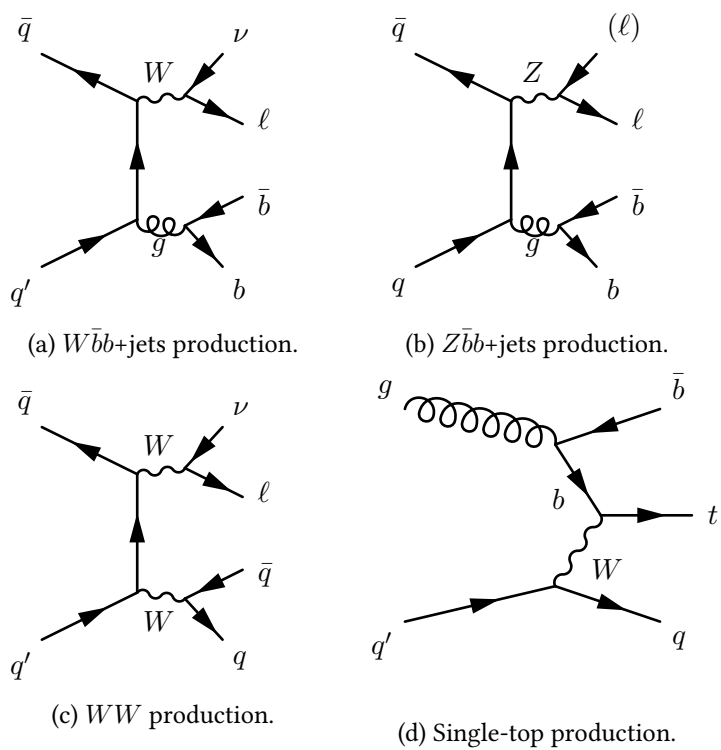
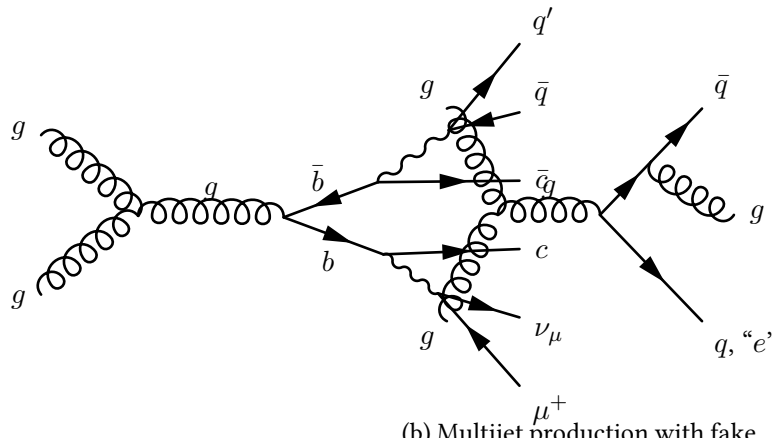


Figure 6.1: Feynman diagrams of some $V + \text{jets}$ and diboson background processes to $t\bar{t}$ in the $\ell + \text{jets}$ channel.

reconstruction of physics objects, fake muons from punch-through and pile-up. Although the probability of each of these processes is small, the large production cross-section for multijet make it an important background. The simulation of these effects for the purpose of background estimation is impractical due to the sample size required. Additionally the simulation of these effects is difficult to model precisely. As a result the multijet background is estimated using data-driven methods.



(a) Multijet production with real lepton.

Figure 6.2: Feynman diagrams of some single-top and multijet background processes to $t\bar{t}$ in the $\ell+jets$ channel.

Diboson, single-lepton and $Z+jets$ backgrounds are estimated using MC simulation.

6.3.1 Multijet in the electron channel

This analysis makes use of two different methodologies, the so-called *matrix method* [64] is used for the central value of the estimate and the so-called *ABCD method* is used for verification.

At pretag level the multijet content in the signal region is estimated by using the matrix method. In addition to the standard electron selection, a looser selection is defined where the isolation requirement is removed. Events are categorized by whether they pass the standard

selection or only loose selection². The number of events in each category is the sum of events with “real” electrons and “fake” electrons as follows:

$$N^{\text{loose}} = N_{\text{real}}^{\text{loose}} + N_{\text{fake}}^{\text{loose}} \quad (6.1)$$

$$N^{\text{std}} = rN_{\text{real}}^{\text{loose}} + fN_{\text{fake}}^{\text{loose}} \quad (6.2)$$

1377 where r and f are the “real” and “fake” efficiencies for the loose event to also pass the standard
 1378 selection. Given a measured N^{std} and N^{loose} in data, and if f and r are known the number of
 1379 events with a fake electron that passes the standard selection can be calculated as

$$N_{\text{fake}}^{\text{std}} = fN_{\text{fake}}^{\text{loose}} = f \frac{N^{\text{std}} - rN^{\text{loose}}}{(f - r)} \quad (6.3)$$

1380 thus $N_{\text{fake}}^{\text{std}}$ is the final estimate of the multijet background in the signal region.

1381 The relative efficiency r is measured from an inclusive sample of $Z \rightarrow ee$ events and f
 1382 is measured from a sample of events with exactly one loose electron, at least one jet with a
 1383 $p_T > 25 \text{ GeV}$ and $E_T^{\text{miss}} < 20 \text{ GeV}$. This sample is enriched with events that have low missing
 1384 energy and one electron likely coming from a jet faking a lepton. An uncertainty of 50 % is
 1385 assigned to the pretag estimate to cover the respective uncertainties on f and r .

1386 To derive the tagged estimate the pretag estimates are scaled by the probability of SMT
 1387 tagging an event. The tagging probability of multijet events $R_{\text{SMT}}^{\text{multijet}}$ is derived from control
 1388 regions defined by the isolation of the electron and the E_T^{miss} cut that forms part of the event
 1389 selection, as shown in Figure 6.3.

1390 These four regions, labelled A through D, can be identified as a background-dominated
 1391 region, containing events with low- E_T^{miss} and a non-isolated electron; a signal region, with
 1392 events that pass the event selection; and two control regions, containing events with high-
 1393 E_T^{miss} or an isolated electron. The events in each of the regions then represents a different
 1394 aspect of multijet events that pass the event selection. The tagging rate is simply defined as

$$R_{\text{SMT}} = \frac{N_{\text{Tagged}}}{N_{\text{Pretag}}} \quad (6.4)$$

1395 where N is the number of events in the region. Contaminations from non-multijet events such

²All muons that pass the standard selection by construction also pass the loose selection

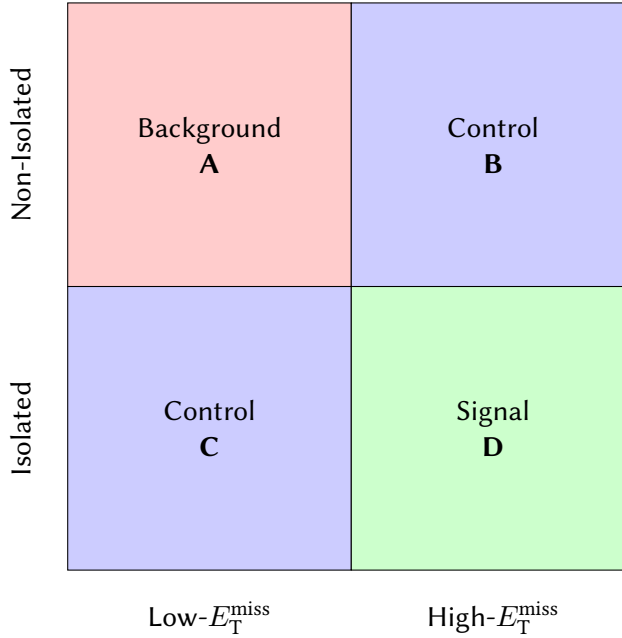


Figure 6.3: A diagram of the E_T^{miss} -isolation phase space. Shown are the four regions as defined by the event selection.

as $W+\text{jets}$, $Z+\text{jets}$, $t\bar{t}$, single-top and diboson events are subtracted using MC simulation. Thus the yield in each region is defined as

$$N^{\text{Multijet}} = N^{\text{Data}} - N^{W+\text{jets}} - N^{Z+\text{jets}} - N^{\text{Diboson}} - N^{t\bar{t}} - N^{\text{Single-top}} \quad (6.5)$$

The largest sources of contaminations in all regions come from $t\bar{t}$, $W+\text{jets}$ and $Z+\text{jets}$. The amount of contamination in each region is summarized in Table 6.2 at pretag level and in Table 6.3 for tag level. Single-top and diboson contribute less than 1 % in most bins and are therefore not shown here. As expected, Region A contains the least amount of contamination from other processes and is dominated by multijet. Regions B and C are dominated by $W+\text{jets}$ in all jet-bins because of the presence a real lepton and E_T^{miss} from the neutrino. The $Z+\text{jets}$ contamination is most significant in region C due to the requirement of an isolated electron but low- E_T^{miss} .

The distribution of various kinematic variables is show in Figure 6.4. There appears to be a large tail in the pretag E_T^{miss} distribution (Figure 6.4a) due to the aforementioned sources of fake E_T^{miss} . The momentum distributions at both pretag and tag level point to the presence of hard leptons present in the multijet background likely coming from misidentified jets. The

Jet-bin	Contamination by [%]		
	$t\bar{t}$	$W+\text{jets}$	$Z+\text{jets}$
Region A			
1	0.01 ± 0.00	6.99 ± 0.02	2.57 ± 0.01
2	0.13 ± 0.01	6.44 ± 0.05	3.87 ± 0.04
3	1.14 ± 0.04	5.72 ± 0.10	4.77 ± 0.09
≥ 3	2.24 ± 0.05	5.64 ± 0.09	4.90 ± 0.08
Region B			
1	0.12 ± 0.01	39.1 ± 0.1	1.64 ± 0.02
2	1.47 ± 0.03	30.6 ± 0.2	2.61 ± 0.05
3	8.42 ± 0.15	22.7 ± 0.3	3.21 ± 0.09
≥ 3	14.0 ± 0.2	20.2 ± 0.2	3.14 ± 0.08
Region C			
1	0.02 ± 0.00	43.3 ± 0.1	20.0 ± 0.4
2	0.49 ± 0.01	36.4 ± 0.1	26.4 ± 1.1
3	4.63 ± 0.09	29.6 ± 0.3	29.9 ± 0.3
≥ 3	8.77 ± 0.11	28.0 ± 0.2	29.2 ± 0.2

Table 6.2: Summary of contamination in all control regions at pretag level. The contamination here is shown out of the total number of events in data. The uncertainties shown include statistical and systematic contributions.

Jet-bin	Contamination by [%]		
	$t\bar{t}$	$W+\text{jets}$	$Z+\text{jets}$
Region A			
1	0.05 ± 0.02	4.46 ± 0.18	0.43 ± 0.05
2	0.82 ± 0.12	4.89 ± 0.30	1.33 ± 0.15
3	5.64 ± 0.54	4.97 ± 0.50	1.54 ± 0.27
≥ 3	10.42 ± 0.61	4.50 ± 0.39	1.75 ± 0.24
Region B			
1	1.09 ± 0.17	26.6 ± 0.9	0.43 ± 0.11
2	8.71 ± 0.55	29.9 ± 0.9	1.02 ± 0.18
3	28.3 ± 1.4	12.2 ± 0.8	1.08 ± 0.24
≥ 3	38.9 ± 1.2	9.84 ± 0.53	0.95 ± 0.16
Region C			
1	0.36 ± 0.07	53.6 ± 1.1	4.78 ± 0.26
2	4.86 ± 0.36	41.5 ± 1.2	11.5 ± 0.6
3	26.5 ± 1.4	30.6 ± 1.5	11.7 ± 0.9
≥ 3	40.5 ± 1.3	24.2 ± 1.0	10.1 ± 0.6

Table 6.3: Summary of contamination in all control regions at tagged level. The contamination here is shown out of the total number of events in data. The uncertainties shown include statistical and systematic contributions.

¹⁴¹⁰ χ^2_{Dof} distribution of the SMT muons peaks at low χ^2_{Dof} values pointing to a good quality of
¹⁴¹¹ fit between the ID and MS tracks of the muon. As expected the SMT muons are soft just as
¹⁴¹² those in $t\bar{t}$ events. One possible source of these soft muons is semileptonic b -decays in from
¹⁴¹³ $b\bar{b}$ production.

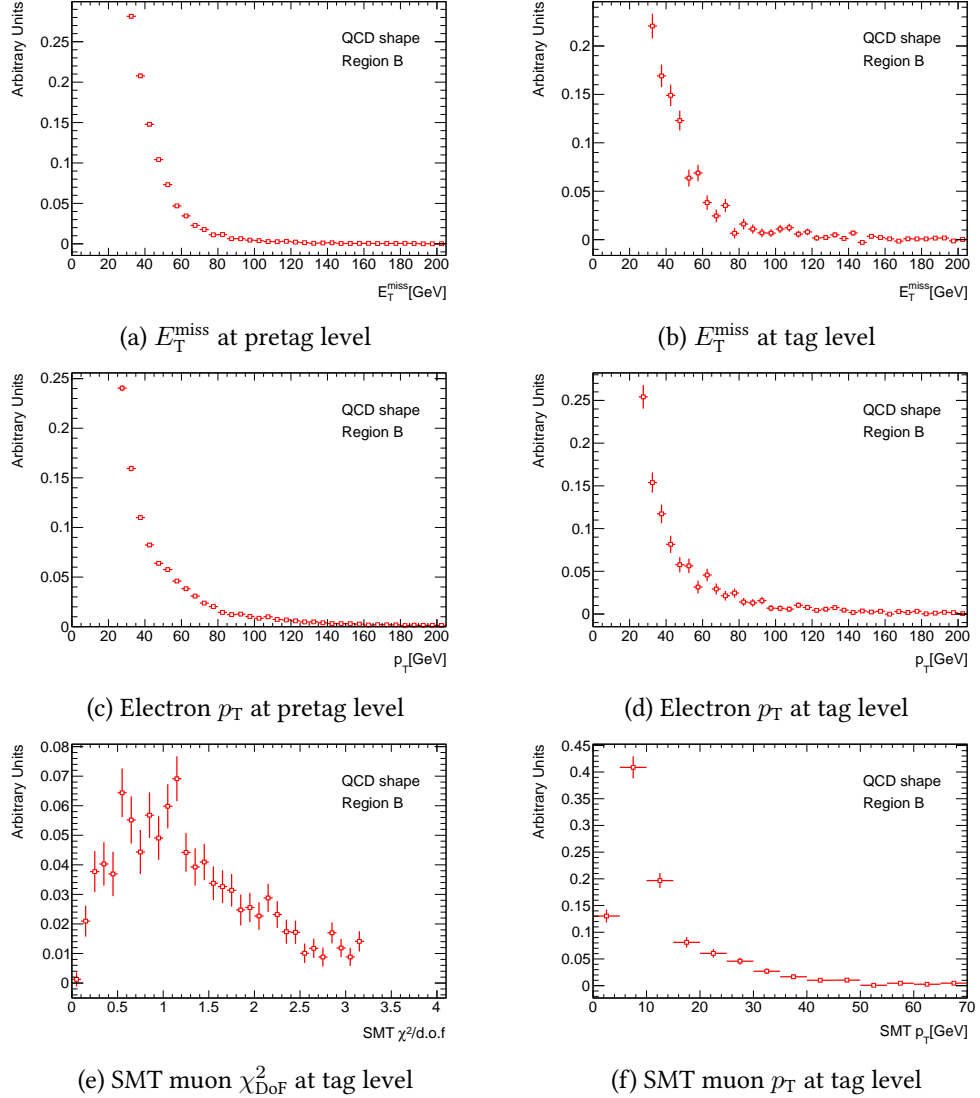


Figure 6.4: Kinematic distributions in region B (high- E_T^{miss} + non-isolated electron) at pretag and tag level. These distributions are obtained by subtracting non-multijet contributions using simulation.

¹⁴¹⁴ The contribution from $t\bar{t}$ is initially based on the theoretical cross-section. An estimate for
¹⁴¹⁵ the multijet contribution is determined using this cross-section and a new measured $t\bar{t}$ cross-
¹⁴¹⁶ section is obtained. The measured cross-section is used to rescale the $t\bar{t}$ contribution and a new

1417 cross-section is obtained. This process is repeated until the measured cross-section stabilizes.
 1418 Only two iterations are needed.

1419 The uncertainty on the tagging-rate contains statistical and systematic contributions. The
 1420 systematic uncertainty includes the uncertainty on the cross-section of the $t\bar{t}$ and W +jets sam-
 1421 ples, uncertainty arising from the SMT tagger and finally uncertainties arising from the BR re-
 1422 weighting described earlier. The dominant source of uncertainty depends on the region and
 1423 jet-bin. in regions where contamination is high the uncertainty from W +jets and $t\bar{t}$ are more
 1424 significant.

1425 The final tagging-rate is the unweighted average of all the regions. This definition was
 1426 chosen as no single type of multijet event is favoured over the others. The uncertainty is the
 1427 difference between regions A and C, as this is larger than the uncertainty on any individual
 1428 region.

1429 The tagging-rates per region for each jet-bin are shown in Table 6.4. Finally, the multijet
 1430 background estimates in the e +jets channel are shown in Table 6.5. The uncertainties on the
 1431 final pretag and tagged estimates are dominated by the 50 % uncertainty on the efficiencies
 1432 associated with the matrix method pretag estimate.

Jet-bin	SMT tagging rate $R^{\text{SMT}} [\%]$			
	Region A	Region B	Region C	Average
1	1.17 ± 0.01	1.10 ± 0.10	0.609 ± 0.056	0.962 ± 0.446
2	2.25 ± 0.03	2.49 ± 0.10	1.55 ± 0.17	2.09 ± 0.47
3	3.44 ± 0.09	4.31 ± 0.21	2.27 ± 0.85	3.34 ± 1.02
≥ 3	3.84 ± 0.09	5.14 ± 0.41	2.52 ± 1.30	3.83 ± 1.31

Table 6.4: Multijet SMT event tagging-rate in regions A) inverted- E_T^{miss} , non-isolated,
 B) High- E_T^{miss} , non-isolated and C) low- E_T^{miss} , isolated.

1433 **The ABCD method**

1434 The ABCD method relies on a pair of uncorrelated variables to extrapolate the amount of
 1435 multijet events from a set of control regions into the signal region. First a two-dimensional
 1436 phase-space is constructed, in this case the same two variables, transverse missing energy and
 1437 lepton isolation are used. If these two variables are uncorrelated then the following relation

Jet-bin	Multijet event yield	
	Pretag	Tagged
1	$145\,000 \pm 72\,000$	1390 ± 700
2	$39\,600 \pm 19\,800$	830 ± 416
3	$11\,300 \pm 5\,700$	378 ± 190
≥ 3	$16\,200 \pm 8\,100$	620 ± 311

Table 6.5: Multijet estimates in the $e+jets$ channel. The uncertainties are combined statistical and systematics. A systematic uncertainty of 50 % is used on the matrix method pretag event yields in addition to the uncertainties obtained on the tagging rate.

¹⁴³⁸ holds

$$\frac{N_D^{\text{Multijet}}}{N_C^{\text{Multijet}}} = \frac{N_B^{\text{Multijet}}}{N_A^{\text{Multijet}}} \quad (6.6)$$

¹⁴³⁹ where N_X^{Multijet} is the number of multijet events in region X. As with the matrix method, the
¹⁴⁴⁰ value of N^{Multijet} is obtained by subtracting the contribution of other processes from the data
¹⁴⁴¹ value using simulation. The contamination and uncertainties at pretag level are shown in
¹⁴⁴² Table 6.2. The contamination present at tag level are summarized in Table 6.3.

¹⁴⁴³ This allows an estimation of the number of multijet events that pass the event selection by
¹⁴⁴⁴ extrapolating from the background region into the signal region. The uncertainty on the final
¹⁴⁴⁵ estimate includes statistical contributions from the yield in each region and the systematic
¹⁴⁴⁶ uncertainty on the $W+jets$ and $t\bar{t}$ samples as described. The multijet estimates in all regions
¹⁴⁴⁷ at pretag and tagged level are presented in Table 6.6. The uncertainty on the estimate in some
¹⁴⁴⁸ jet-bins is smaller than the matrix method estimate. However, in the signal jet-bin (≥ 3) the
¹⁴⁴⁹ uncertainty at tag level is very large. As a result the matrix method estimate is used and the
¹⁴⁵⁰ ABCD estimate is used as a cross-section. Comparing the results from the matrix method and
¹⁴⁵¹ the ABCD method, it appears that both yield compatible results within their uncertainties.

¹⁴⁵² 6.3.2 Multijet background in the muon channel

¹⁴⁵³ The procedure in the muon channel is similar to that used for the electron channel. A pretag
¹⁴⁵⁴ estimate of the multijet fraction in the signal region is obtained using the matrix method. The
¹⁴⁵⁵ “real” muon selection efficiency r is measured from an inclusive sample of $Z \rightarrow \mu\mu$ events.

Jet-Bin	Multijet event yield	
	Pretag	Tag
1	$99\,000 \pm 48\,000$	565 ± 264
2	$33\,500 \pm 13\,000$	572 ± 272
3	9500 ± 3320	270 ± 220
≥ 3	$13\,000 \pm 5000$	438 ± 449

Table 6.6: Multijet estimates obtained using the ABCD method. The uncertainty contains statistical and systematic components.

1456 The “fake” muon selection efficiency f is obtained from data using two different samples:

- 1457 • a background-dominated control region where the $E_T^{\text{miss}} + m_{T,W}$ cut is inverted and an
1458 additional cut of $m_{T,W} < 20$ GeV is applied,
- 1459 • and a fit to the transverse impact parameter significance σ_{d_0} distribution where both
1460 $E_T^{\text{miss}} + m_{T,W}$ and E_T^{miss} cuts are inverted.

1461 The central value of the pretag estimate is obtained from an average of these two regions
1462 and was found to be $27\,000 \pm 5400$. An uncertainty of 20 % is assigned to the final estimate to
1463 account for the uncertainty associated with each region and the difference between them.

1464 The SMT event tagging rate is obtained from two control regions, defined by inverting the
1465 E_T^{miss} and $E_T^{\text{miss}} + m_{T,W}$ cuts, and by inverting the muon isolation requirement. As with the
1466 electron analysis, contamination from other non-multijet processes is subtracted using MC
1467 simulation. Finally, the sources of uncertainty are also the same as those considered in the
1468 electron channel.

1469 The final multijet estimate at tagged level is obtained by multiplying the average pretag
1470 estimate by the unweighted tagging rate. The uncertainty on the unweighted tagging rate is
1471 set to half the difference between the two control regions, as this is larger than the individual
1472 uncertainties combined. The final uncertainty is obtained by combining the uncertainty on the
1473 pretag estimate and the uncertainty on the tagging-rate. The final tagged estimate was found
1474 to be 1310 ± 350 .

Control region	SMT tagging rate [%]
Inverted isolation	5.7 ± 0.1
Inverted triangular cut	4.0 ± 0.5
Unweighted average	4.9 ± 0.8

Table 6.7: Summary of tagging-rates as measured in data in the two multijet-dominated regions. The uncertainty quoted includes statistical and systematic contributions. The uncertainty on the unweighted average is set as half of the difference between control regions [6].

1475 6.3.3 W +jets background

1476 The W +jets background is the most dominant background since these events contain a real
 1477 lepton and E_T^{miss} from the escaping neutrino. Events can be classified into W +HF, which is the
 1478 largest contribution; and W +LF where a LF jet is mistagged. Due to the significant uncertainty
 1479 on the overall normalization of W +jets and the presence of a mistagged LF jet, a data-driven
 1480 method known as W charge asymmetry [65] is used to estimate this background.

The W charge asymmetry method relies on the charge asymmetry in the production of W -bosons. As the LHC is a proton-proton collider, up-type valance quarks are more prevalent, resulting in an increased rate of W^+ production via $u\bar{d} \rightarrow W^+$ or $c\bar{s} \rightarrow W^+$ compared to W^- production involving down-type quarks. The ratio of these production cross-sections r is theoretically well understood [66]. It is thus possible to use this ratio as measured in MC simulation to determine an overall normalization in data from the following formula:

$$N_{W^+} + N_{W^-} = \frac{N_{W^+}^{\text{MC}} + N_{W^-}^{\text{MC}}}{N_{W^+}^{\text{MC}} - N_{W^-}^{\text{MC}}} (D^+ - D^-) \quad (6.7)$$

$$= \frac{r_{\text{MC}} + 1}{r_{\text{MC}} - 1} (D^+ - D^-) \quad (6.8)$$

1481 where r_{MC} is the ratio as measured in MC and D^\pm are the number of events in data with a
 1482 positively- or negatively-charged lepton. Contributions from other charge asymmetric pro-
 1483 cesses, namely single-top and diboson are removed using MC simulation. This results in
 1484 an overall normalization for the W +jets background at the pretag level. The flavour of the
 1485 quarks produced in association with the W -boson is particularly important when performing
 1486 b -tagging. Events are categorized by the flavour of these accompanying quarks into $Wc+jets$,

Channel	Pretag	Tagged
$e+\text{jets}$	$59\,300 \pm 5\,400$	1640 ± 330
$\mu+\text{jets}$	$117\,200 \pm 9\,300$	2900 ± 500

Table 6.8: Summary of the $W+\text{jets}$ background estimates for the electron and muon channels [6].

1487 $Wb\bar{b}+\text{jets}$, $Wc\bar{c}+\text{jets}$ and $W+\text{LF}$. The tagged level estimate is obtained by multiplying the pre-
1488 tag estimate via a tagging-rate, obtained separately for $b\bar{b}$, $c\bar{c}$, c and LF separately. The overall
1489 tagged estimate is then obtained using the following formula:

$$W_{\text{tag}} = R_{\text{tag}}^{\text{LF}} W_{\text{pretag}}^{\text{LF}} + \sum_{\text{HF}}^{\text{HF}=c,cc,b\bar{b}} R_{\text{tag}}^{\text{HF}} W_{\text{pretag}}^{\text{HF}} \quad (6.9)$$

1490 where $R_{\text{tag}}^{\text{LF}}$ is defined as the probability to mistag a LF event and $R_{\text{tag}}^{\text{HF}}$ is the probability to
1491 correctly tag a HF event. The tagging rates are obtained from simulation with the SMT scale
1492 factors and BR reweighting applied to each tagged jet. The results of the estimation are sum-
1493 marized in Table 6.8.

1494 6.3.4 Background Shapes

1495 Kinematic distributions are shown at the tagged level in Figures 6.5 for events with at least
1496 three jets in both electron and muon channels. The multijet distributions are taken from data
1497 normalized to the obtained estimates. In the electron channel the shapes obtained from region
1498 B as defined in Figure 6.3 with contamination from non-multijet processes has been removed.
1499 The multijet shapes in the muon channel are obtained from the loose selection in data, after the
1500 application of per-event weights obtained from the matrix method. SMT muon distributions
1501 for both background and signal are shown in Figure 6.6. It is noted that the χ^2_{DoF} distribution
1502 is shifted in both channels in data compared to the simulation. Any such discrepancies are
1503 accounted for by the χ^2_{DoF} scale factor. Good agreement between data and estimations, both
1504 simulation-based and data-driven, is observed in all distributions.

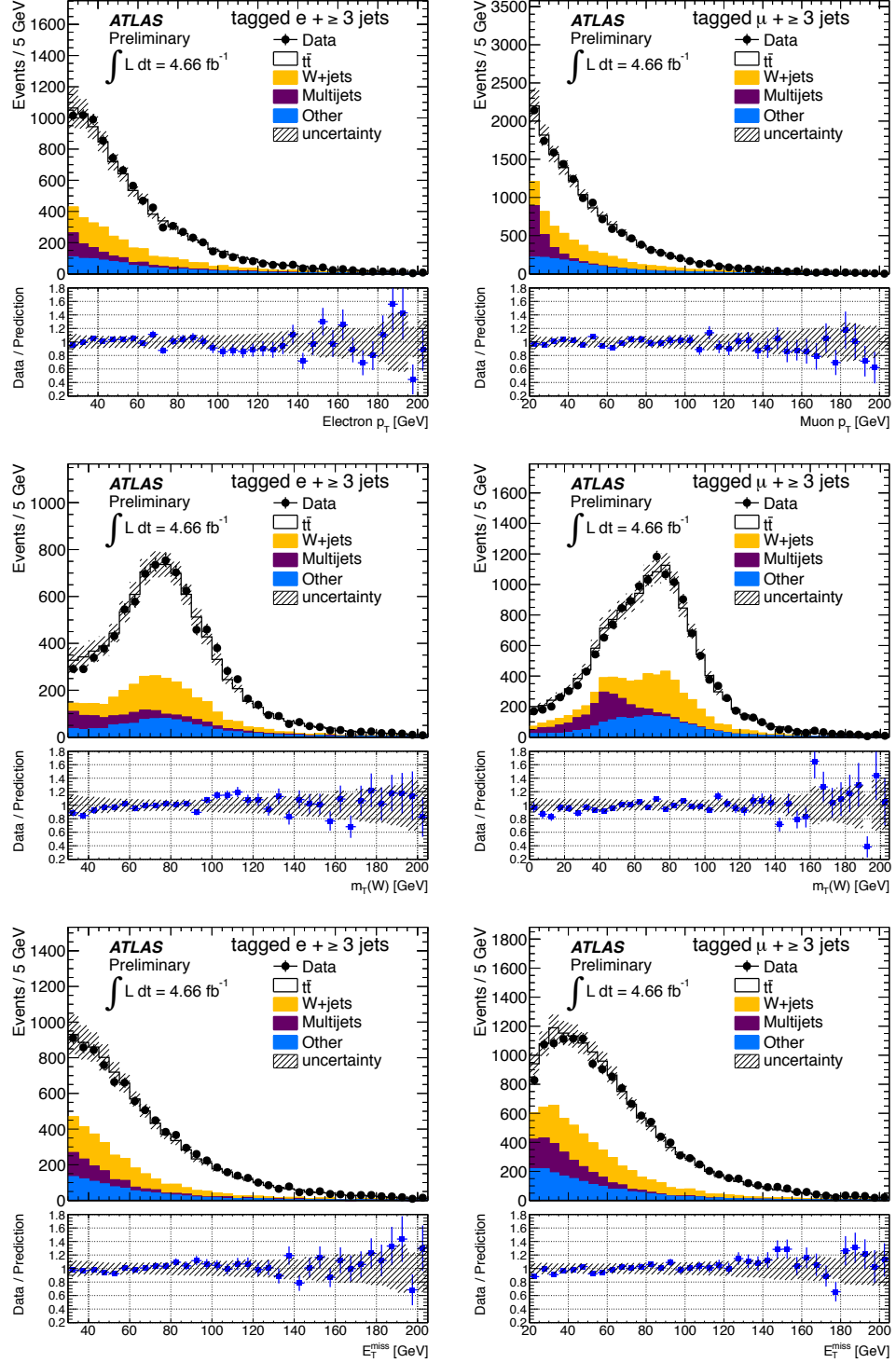


Figure 6.5: Distributions for tagged events in the $e + \text{jets}$ (left) and $\mu + \text{jets}$ (right) channels of, from top to bottom, lepton p_T , transverse W mass and missing transverse energy [6].

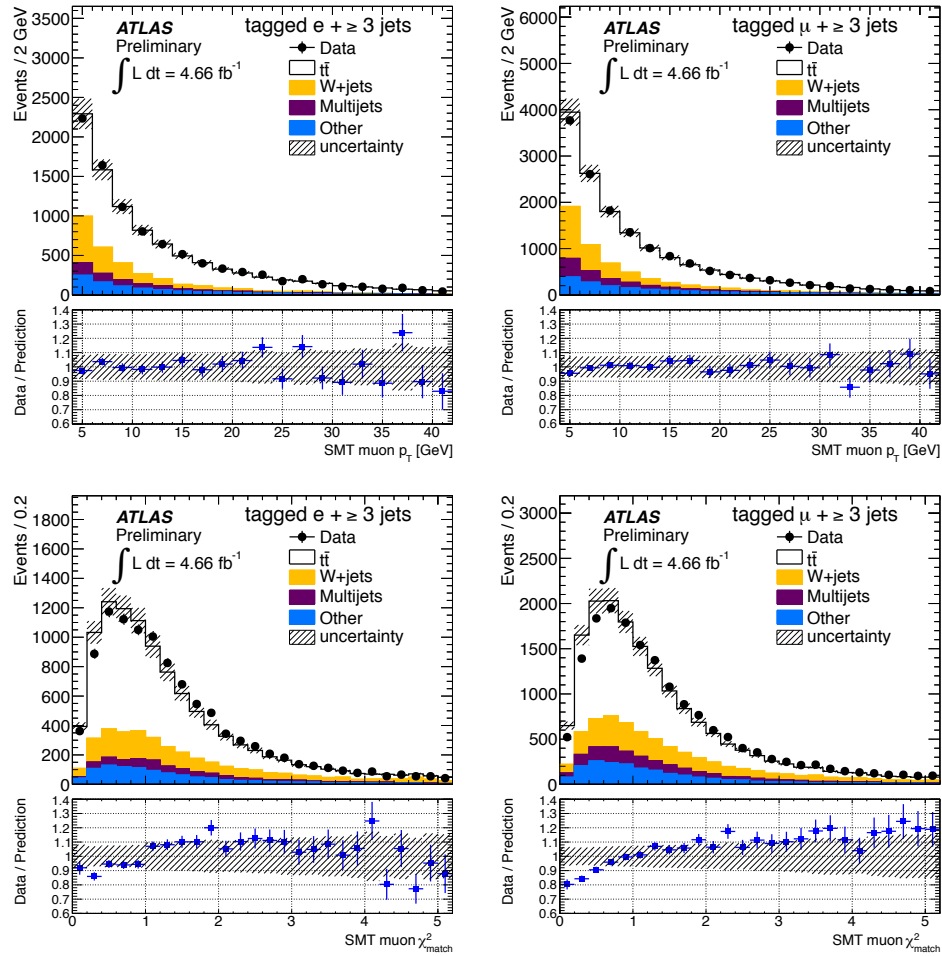


Figure 6.6: Distributions of SMT variables in the $e + \text{jets}$ (left) and $\mu + \text{jets}$ (right) channels, from top to bottom, SMT muon p_T and SMT muon χ^2_{DoF} [6].

1505 **6.4 Systematic uncertainties**

1506 The uncertainties associated with the cross-section include various sources such as signal sim-
 1507 ulation, object reconstruction, background estimation, integrated luminosity determination
 1508 and tagger uncertainties (Table 6.9). The SMT tagger uncertainty is made of the STACO CB
 1509 reconstruction uncertainty and the uncertainty on the χ^2_{match} efficiency measurement.

1510 The signal modelling uncertainties are evaluated by repeating the cross-section measure-
 1511 ment while substituting the main $t\bar{t}$ sample with alternate ones. The NLO generator uncer-
 1512 tainty covers any differences in the modelling of kinematic distributions at parton level as a
 1513 result of the hard interaction in different generators. This is evaluated by comparing the signal
 1514 acceptance in ALPGEN and POWHEG samples to the nominal sample. Initial and final state
 1515 radiation (ISR/FSR)

1516 The largest uncertainties come from the background estimation methods, JES and SMT
 1517 tagger uncertainties. In the multijet background estimate, the uncertainty associated with the
 1518 matrix method pretag estimates is the largest contribution at 50 % of the estimate. The tagger
 1519 uncertainties, including the $b \rightarrow \mu X$ BR reweighting uncertainty, contribute approximately
 1520 $+3.2\%$ to the total uncertainty. In comparison, the total b -tagging uncertainty as measured by
 1521 another ℓ +jets analysis using JetProb is $\pm 4.1\%$ [67]. This is larger than the total SMT tagger
 1522 uncertainty despite including the BR reweighting uncertainty and the analysis quoted above
 1523 being more recent. The analysis uncertainty is dominated by the systematic contributions.
 1524 The reduced acceptance due to the BR of $b \rightarrow \mu$ is not significant in this case.

1525 **6.5 Results and conclusion**

1526 The event yields in data, signal $t\bar{t}$ MC and background contributions that pass the event selec-
 1527 tion for both pretag and tagged in the muon and electron channels are shown in Table 6.10.

1528 The final cross-section is determined by a cut-and-count method and is calculated as

$$\sigma_{t\bar{t}} = \frac{N_{\text{data}} - N_{\text{bkg}}}{\int L dt \times \epsilon \times \text{BR}(\text{noFullHad})} \quad (6.10)$$

1529 where N_{data} is the number of events in collision data that pass the event selection, N_{bkg} is
 1530 the number of events that pass the event selection as estimated using the aforementioned

Source	Relative cross-section uncertainty [%]		
	$e+\text{jets}$	$\mu+\text{jets}$	Combined
Statistical Uncertainty	± 1.5	± 1.3	± 1.0
Object Selection			
Lepton Energy Resolution	$+0.4/-0.3$	$+0.2/-0.01$	$+0.2/-0.1$
Lepton Reco, ID, Trigger	$+2.4/-2.5$	$+1.5/-1.5$	$+1.5/-1.8$
Jet Energy Scale	$+3.8/-4.3$	$+3.2/-3.6$	$+3.5/-3.8$
Jet Energy Resolution	± 0.2	± 0.5	± 0.2
Jet Reconstruction Efficiency	± 0.06	± 0.06	± 0.06
Jet Vertex Fraction	$+1.2/-1.4$	$+1.2/-1.4$	$+1.2/-1.4$
E_T^{miss} Uncertainty	± 0.06	± 0.08	± 0.07
SMT Calibration			
STACO Reconstruction Eff.	± 1.3	± 1.3	± 1.3
Muon χ^2_{match} Eff.	± 0.6	± 0.6	± 0.6
Background Estimates			
Multijet Normalisation	± 5.2	± 3.9	± 4.4
$W+\text{jets}$ Normalisation	± 5.2	± 5.7	± 5.5
Other Bkg Normalisation	± 0.2	± 0.2	± 0.1
Other Bkg Systematics	$+1.6/-1.5$	$+2.5/-2.0$	$+2.2/-1.8$
Signal Simulation			
$b \rightarrow \mu X$ Branching Ratio	$+2.9/-3.0$	$+2.9/-3.1$	$+2.9/-3.1$
ISR/FSR	± 2.4	± 0.9	± 1.5
PDF	± 3.2	± 3.0	± 3.1
NLO Generator	± 3.2	± 3.2	± 3.2
Parton Shower	± 2.2	± 2.2	± 2.2
Total Systematics	$+11.1/-11.3$	$+10.2/-10.3$	$+10.5/-10.6$
Integrated Luminosity	± 1.8	± 1.8	± 1.8

Table 6.9: List of cross-section uncertainty sources for the three-jets inclusive selection [6].

Sample	Event yields in			
	$e+$ jets		$\mu+$ jets	
	Pretag	Tagged	Pretag	Tagged
Data	124 424	9165	227 318	14 940
MC				
$t\bar{t}$	$31\,900 \pm 1300$	5980 ± 350	$52\,100 \pm 1600$	9100 ± 500
$Z+$ jets	9900^{+2500}_{-1400}	270^{+40}_{-30}	11500^{+2400}_{-1600}	780^{+140}_{-100}
Diboson	1190^{+220}_{-180}	40 ± 10	2030^{+350}_{-300}	60 ± 10
Single top	4300 ± 400	630 ± 60	7200 ± 600	980 ± 80
Data-Driven				
Multijet	$16\,200 \pm 8100$	620 ± 310	$27\,000 \pm 5400$	1310 ± 350
$W+$ jets	$59\,300 \pm 5400$	1640 ± 330	$117\,200 \pm 9300$	2900 ± 500
Measured $t\bar{t}$		6000 ± 500		8900 ± 600

Table 6.10: Event yields for signal and background events, as well as the yield measured in data [6].

Channel	Selection Efficiency [%]
$e+$ jets	1.42 ± 0.02
$\mu+$ jets	2.15 ± 0.02
Combined	3.57 ± 0.03

Table 6.11: Summary of event selection efficiencies for the muon, electron and combined channels as measured on the signal $t\bar{t}$ sample [6].

methods, ϵ is the estimated selection efficiency (Table 6.11) and $\text{BR}(\text{noFullHad}) = 0.543$ is the semileptonic and dilepton total branching ratio using a $W \rightarrow \ell\nu$ branching ratio of 0.108 per flavour. The combined cross-section is obtained by combining $e+$ jets and $\mu+$ jets event yields.

The final cross-sections were measured to be

$$\sigma_{t\bar{t}}^{e+\text{jets}} = 167 \pm 3 \text{ (stat.)} \pm 20 \text{ (syst.)} \pm 3 \text{ (lumi.) pb} \quad (6.11)$$

$$\sigma_{t\bar{t}}^{\mu+\text{jets}} = 164 \pm 2 \text{ (stat.)} \pm 17 \text{ (syst.)} \pm 3 \text{ (lumi.) pb} \quad (6.12)$$

$$\sigma_{t\bar{t}} = 165 \pm 2 \text{ (stat.)} \pm 17 \text{ (syst.)} \pm 3 \text{ (lumi.) pb} \quad (6.13)$$

1534 The two channels appear to be in agreement with eachother. No excess of events is ob-
1535 served and the combined cross-section is in good agreement with the latest theoretical SM
1536 cross-section at $\sigma_{t\bar{t}} = 158^{+13.5}_{-12.2}$ pb. The result is also in agreement within uncertainty with
1537 other ATLAS measurements made with different methods. These results, including the one
1538 obtained in this analysis, are summarized in Figure 3.6.

1539 **Chapter 7**

1540 **Muon identification in a boosted $t\bar{t}$
1541 environment**

1542 The large center-of-mass energies at which collisions occur at the LHC allows for the pro-
1543 duction of very high mass particles. Several BSM theories predict the existence of high mass
1544 particles which decay primarily into top-quark pairs. An example of hypothetical model which
1545 predict high mass $t\bar{t}$ resonances is the topcolor assisted technicolor model (TC2), which pre-
1546 dicted the existence of a leptophobic Z' boson. The resultant top quark pair provides a well
1547 understood probe to search for such hypothetical particles.

1548 The Z' could potentially have a mass on the order of several TeV. As a result their decay
1549 product would be produced in the detector with very large momentum. These top quarks are
1550 said to be boosted. In terms of the subsequent top decay, the resultant bottom quark and W
1551 boson are expected to emerge in a collimated cone. The events thus appear as two large back-
1552 to-back jets. If the W decays leptonically, the W lepton is expected to lie very close to or within
1553 the b -jet. If the W decays hadronically all three jets will appear to merge into a single *fat jet*. In
1554 contrast, low boost events where all products are well separated are known as resolved events.

1555 In this chapter the results of a feasibility study conducted to determine the viability of using
1556 the χ^2_{match} tagger to tag W muons from boosted top-quark decays is presented and discussed.
1557 Note that this is in contrast to the cross-section analysis detailed in a previous chapter where
1558 the muon tagged came from the semileptonic decay of b -quarks. The boost is expected to be
1559 related to the mass of the Z' produced, so a higher mass Z' would decay into more collimated

Talk
about
other
possible
models

1560 jets. The environment that results is thus very similar to that of a semileptonic b -decay: a
1561 muon buried inside of a b -jet.

1562 No evidence for such a resonance has been observed and limits have been placed on the
1563 production rate of these resonance for various benchmark models. A leptophobic topcolor
1564 Z' of mass less than 1.74 TeV has been excluded using 4.7 fb^{-1} of ATLAS collision data at
1565 $\sqrt{s} = 7 \text{ TeV}$ [40] using a both resolved and boosted reconstruction approaches. A more recent
1566 analysis using 14.3 fb^{-1} of $\sqrt{s} = 8 \text{ TeV}$ data excluded a Z' with a mass less than 1.8 TeV
1567 at 95 % confidence level [68] with the same combined reconstruction approach. The analysis
1568 detailed here is based on the 7 TeV analysis. Similar analyses performed with data collected
1569 by CMS using resolved and boosted reconstructions have excluded Z' candidates for similar
1570 benchmark models [69–71].

1571 As the boost increases, the nominal isolation requirements used in the resolved $t\bar{t}$ reso-
1572 nance search, namely cuts on $E_T^{\text{cone}\Delta R}$ or $p_T^{\text{cone}\Delta R}$ with a predefined cone size, begin to remove
1573 too many leptons. This results in very low lepton selection efficiency and poor acceptance in
1574 the higher mass range. As a result much effort has gone into adapting the isolation require-
1575 ments to boosted events.

1576 The χ_{match}^2 tagger could serve as a replacement for the traditional isolation requirements
1577 or as a complement to other methodologies. A novel approach known as mini-isolation (MI)
1578 was developed by the ATLAS $t\bar{t}$ resonance group. The results of a preliminary study of the
1579 efficiency of both of these metholodiges are presented and compared. In addition the χ_{match}^2
1580 tagger performance as a b -tagger in boosted $t\bar{t}$ events is compared to the nominal approach
1581 that relies on the standard MV1 tagger.

1582 7.1 Data samples

1583 This measurement is based on simulated data generated for a Z' with a mass of 1.0, 1.3, 1.6,
1584 2.0, 2.5 and 3.0 TeV. All MC simulation samples were generated using PYTHIA [63] with
1585 CTEQ6LI [72] PDFs. The width of the generated Z' is 3 % of the mass. Non-resonant $t\bar{t}$ events
1586 are simulated with MC@NLO v4.01 [57, 58] interfaced to HERWIG [59] for parton showering
1587 and hadronisation and JIMMY [60] for underlying event simulation.

1588 The analysis is based on the underlying event information created by the simulation soft-

1589 ware. This includes the kinematic information of particles in the event as well as the child-
1590 parent connection between particles. For example the Z' has two daughter particles associated
1591 with it, the top and antitop. The decay chain continues with the W bosons and b -quarks. By
1592 navigating up or down this chain it is possible to ascertain the origin of a given particle. The
1593 truth information represents the state of various particles without the effects of the detector,
1594 that is the p_T of a given truth particle is not affected by detector resolution for example.

1595 7.2 Boosted event topology

1596 In order to perform an effective feasibility study, it is important to understand the signature
1597 left by boosted events in the detector. There are certain expectations regarding the momentum
1598 distribution of the various product particles from the decay of the top as well as their angular
1599 separation. As with the cross-section analysis presented in Chapter 6, this study focuses on
1600 lepton plus jets channel of top quark events.

1601 It is expected for events where the momentum of the top quarks is higher to exhibit
1602 stronger collimation between the W muon and the b -quark. This results in a situation very
1603 similar to that exploited for muon tagging in Section 6 where a muon from the semileptonic
1604 decay of a b -quark emerges from within the b -jet as shown in Figure 7.1. It is thus possible to
1605 use the χ^2_{match} tagger¹ to tag W muons in boosted events. As the tagger is designed to work in
1606 energetically “busy” sectors of the detector, it is ideally suited to probe highly boosted events
1607 where the decay products are collimated.

1608 As can be seen from Figure 7.2 the increase in boost does result in the W muon and b -
1609 quark emerging closer. Note that the fraction of events below the χ^2_{match} tagger requirement
1610 of $\Delta R_\mu^{\text{jet}} < 0.5$ increases with top-quark p_T . Additionally as can be seen in Figure 7.3 the top
1611 p_T distribution peaks at just below half of the mass of the Z' boson, thus the large portion of
1612 the candidate muons in the sample will pass the aforementioned separation requirement. The
1613 decay products of the boosted top quark appear to emerge primarily back to back as seen in
1614 Figure 7.4, while the b -quarks from non-resonant $t\bar{t}$ emerge closer more often.

¹Since signal muons in this analysis have large p_T , the tagger is now referred to as the χ^2_{match} tagger not Soft Muon Tagger to reflect this difference

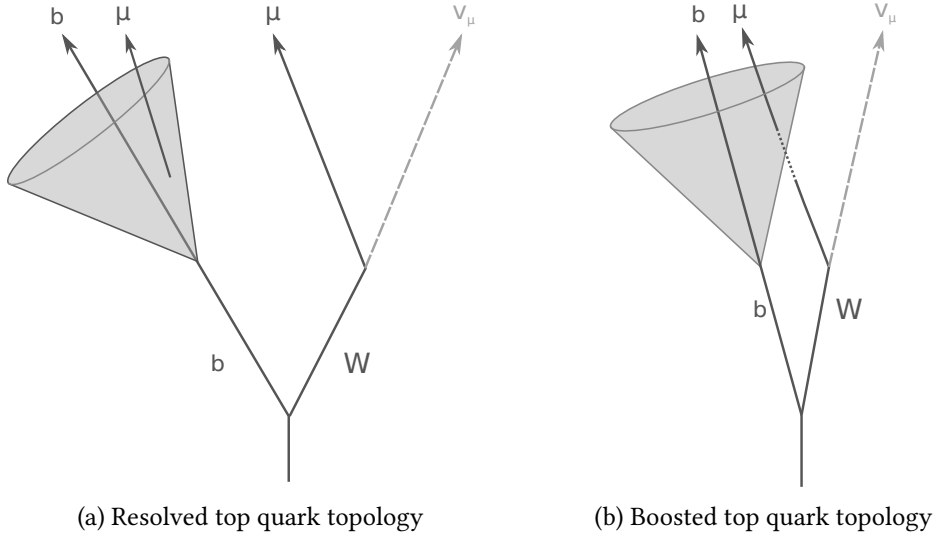


Figure 7.1: Diagrams of the possible configurations of final-state objects in a (a) boosted and (b) non-boosted events.

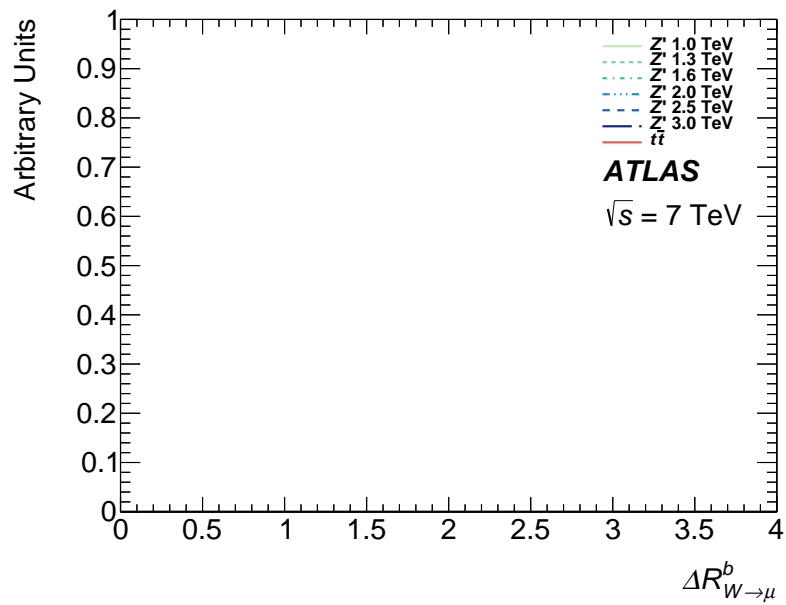


Figure 7.2: The angular separation (ΔR) between the truth W muon and the corresponding b -quark for all examined Z' mass points and non-resonant $t\bar{t}$.

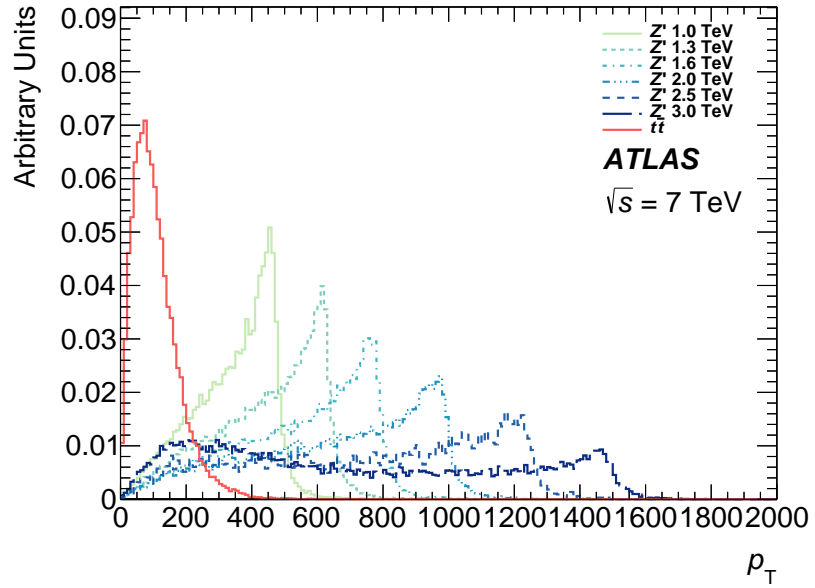


Figure 7.3: The transverse momentum of the top/anti-top quarks in the event for all examined Z' mass points and non-resonant $t\bar{t}$.

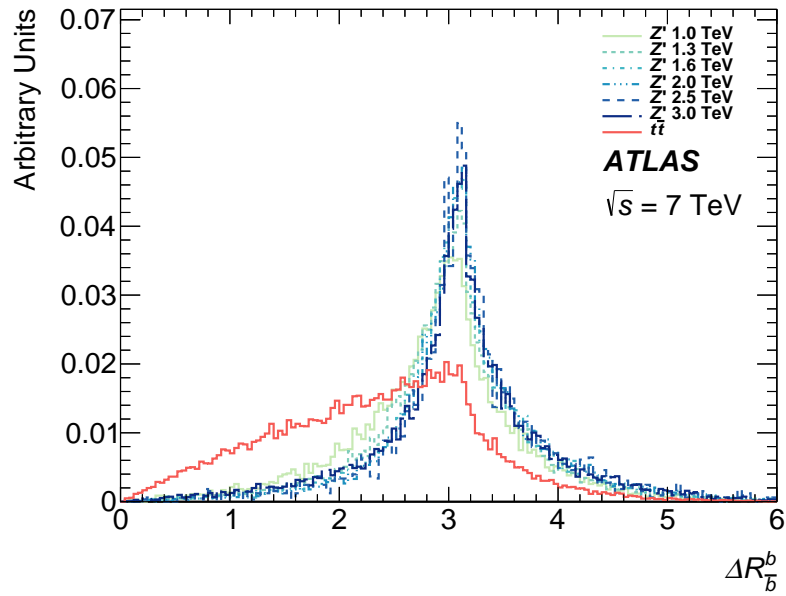


Figure 7.4: The angular separation (ΔR) between the b and \bar{b} in the event for all examined Z' mass points and non-resonant $t\bar{t}$.

1615 **7.3 Signal muon selection**

1616 Part of the object selection used in the top cross-section measurement described in Chapter 5
 1617 and the $t\bar{t}$ resonance analysis is an isolation requirement. However, boosted top events result
 1618 in large collimated jets which include the products of the top quarks. Thus the signal lepton
 1619 can emerge within the cone of the reconstructed jet from the b -quark.

1620 Consequently the muon is not required to be isolated, instead the muon is tagged by the
 1621 χ^2_{match} tagger. Additionally, as explained above, events which exhibit stronger collimation are
 1622 more likely to emerge from particles with higher masses. By requesting the muons be isolated,
 1623 the ability to probe those higher mass events is diminished.

1624 The ATLAS boosted $t\bar{t}$ resonance analysis proposed an alternative variable to replace the
 1625 nominal isolation requirement called mini-isolation (MI). The absolute MI is defined as the sum
 1626 of the measured transverse momenta of all tracks in a cone of size $\Delta R = k_T/p_T^\ell$ around the
 1627 lepton, where k_T is an adjustable scale and p_T^ℓ is the momentum of the lepton in question. This
 1628 study uses the *relative* MI where the absolute value is scaled by the momentum of the lepton
 1629 Rel. MI = MI/ p_T^ℓ . MI adapts to the strong collimation of the top products with increasing
 1630 boost by shrinking the size of the cone for higher boost top quarks.

1631 In this study, the performance of the χ^2_{match} tagger is measured against using the conven-
 1632 tional isolation criteria and MI with $k_T = 10$ and where the lepton is deemed isolated if the
 1633 $\sum p_T$ is less than 5 % of the lepton p_T . The χ^2_{match} tagger operates with the same selection used
 1634 in Chapter 5, the cuts are $|z_0| < 3.0 \text{ mm}$, $|d_0| < 3.0 \text{ mm}$ and finally $\chi^2_{\text{DoF}} < 3.2$. Three sep-
 1635 arate selections are applied, one for the conventional isolation, one for MI and one for χ^2_{match}
 1636 tagger. Each methodology has its own set of muon reconstruction criteria. Both require a
 1637 high- p_T muon ($p_T > 20 \text{ GeV}$) within the pseudorapidity coverage of the ID ($|\eta| < 2.5$) that
 1638 passes the MCP tracking cuts detailed in Appendix E. MI makes use of muons reconstructed
 1639 by the MUID algorithm that pass the so-called *Tight* identification criteria. An additional re-
 1640 quirement on the impact parameter ($|z_0| < 3.0 \text{ mm}$) is used to reduce non-prompt muons. The
 1641 χ^2_{match} tagger uses the STACO combined algorithm for muon reconstruction with no additional
 1642 requirements.

1643 The distribution of pseudorapidity for χ^2_{match} tagged muons, as expected, is similar for all
 1644 $m_{Z'}$ samples as shown in Figure 7.5b. Interestingly, in Figure 7.5a, the average transverse

1645 momentum of the χ_{match}^2 muon increases with $m_{Z'}$ up to 1.6 TeV then stabilizes for higher
 1646 masses. This suggests that the b -quark takes a larger portion of the top quark momentum
 1647 above a certain threshold. As expected the angular separation between the χ_{match}^2 tagged muon
 1648 and the jet in the event decreases with increased $m_{Z'}$ as shown in Figure 7.5c. Finally, the χ_{DoF}^2
 1649 distribution is not affected by changes in $m_{Z'}$ as shown in Figure 7.5d. Thus the efficiency of
 1650 the χ_{match}^2 tagger should be stable through-out the mass range. Similar comments can be made
 1651 with regards to the MI10 muons with regards to their transverse momentum (Figure 7.6a),
 1652 pseudorapidity (Figure 7.6b) and angular separation from the nearest jet (Figure 7.6c). The size
 1653 of the cone used in MI is inversely proportional to the lepton p_{T} . As expected, the cone size
 1654 distributions are much wider with longer tails at low $m_{Z'}$ and more narrow at high $m_{Z'}$ as
 1655 shown in Figure 7.6d.

1656 7.4 Efficiency definition

1657 The efficiency measurement was designed to provide an accurate representation of the perfor-
 1658 mance of the χ_{match}^2 tagger and a fair comparison with mini-isolation. Additional sources of
 1659 inefficiency such as muon reconstruction are separated out into an additional efficiency which
 1660 is also quoted. See Figure 7.7 for a summary of the efficiency measurement.

1661 Firstly, events where a W boson decays into a muon are selected using truth information.
 1662 These events are then used to measure the efficiency. Note that at each stage the denominator
 1663 is the numerator of the previous efficiency. Thus the complete efficiency is given by the product
 1664 of all the efficiency components. This allows for an estimation of the number of W muons that
 1665 would be selected.

1666 First, the truth W muons are matched to STACO/MUID muons if the angular separation
 1667 (ΔR) between them is less than 0.0015. The matching efficiency is defined as:

$$\epsilon_{\text{match}} = \frac{\text{STACO/MUID muons matched to truth } W \text{ muon}}{\text{Truth } W \text{ muons}} \quad (7.1)$$

1668 The selections then diverge and the two sets of reconstruction cuts described earlier are
 1669 applied independently with an efficiency defined as:

$$\epsilon_{\text{reco}} = \frac{\text{STACO/MUID muons that pass reconstruction cuts}}{\text{STACO/MUID muons matched to truth } W \text{ muon}} \quad (7.2)$$

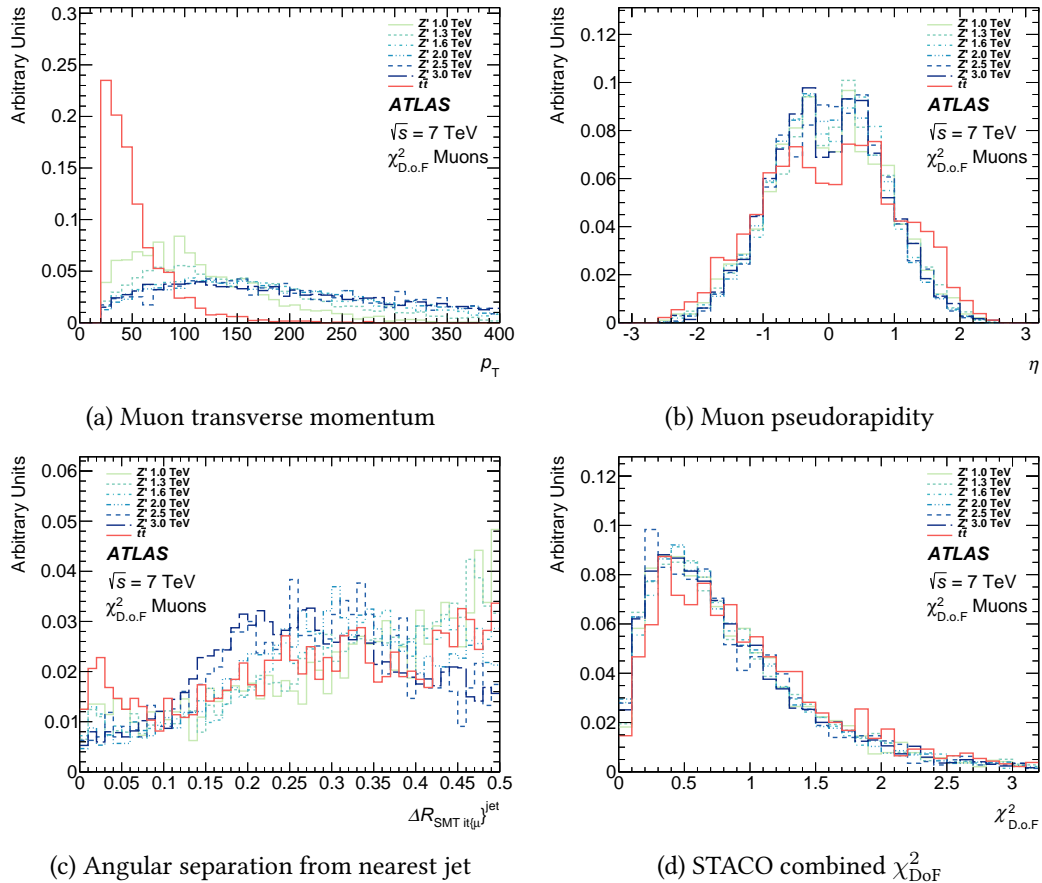


Figure 7.5: Distributions for all tested Z' mass points of (a) the transverse momentum and (b) pseudorapidity of muons which pass the χ^2_{match} tagger selection, the (c) angular separation between those muons and the nearest jet in the event, and (d) the χ^2_{match} used in the selection. All distributions normalized to unit area.

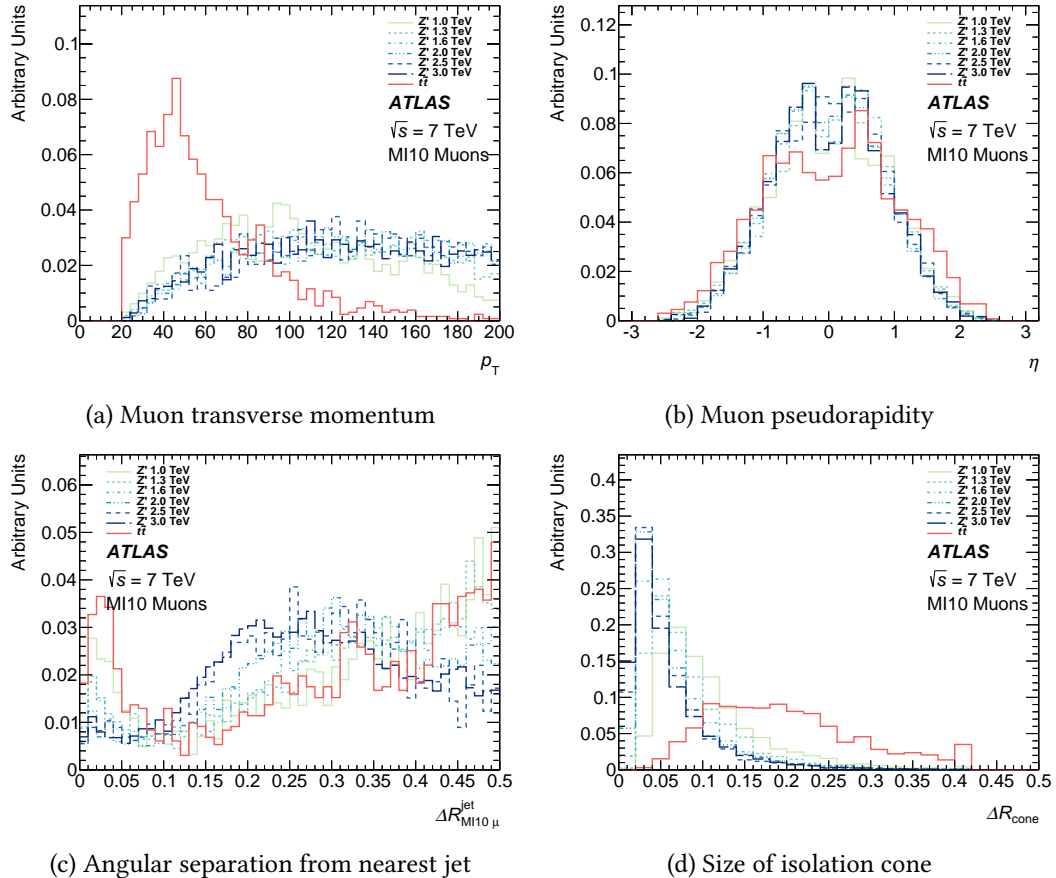


Figure 7.6: Distributions for all tested Z' mass points of (a) the transverse momentum and (b) pseudorapidity of muons which pass the MI10 selection, the (c) angular separation between those muons and the nearest jet in the event, and (d) the cone size used in the selection. All distributions normalized to unit area.

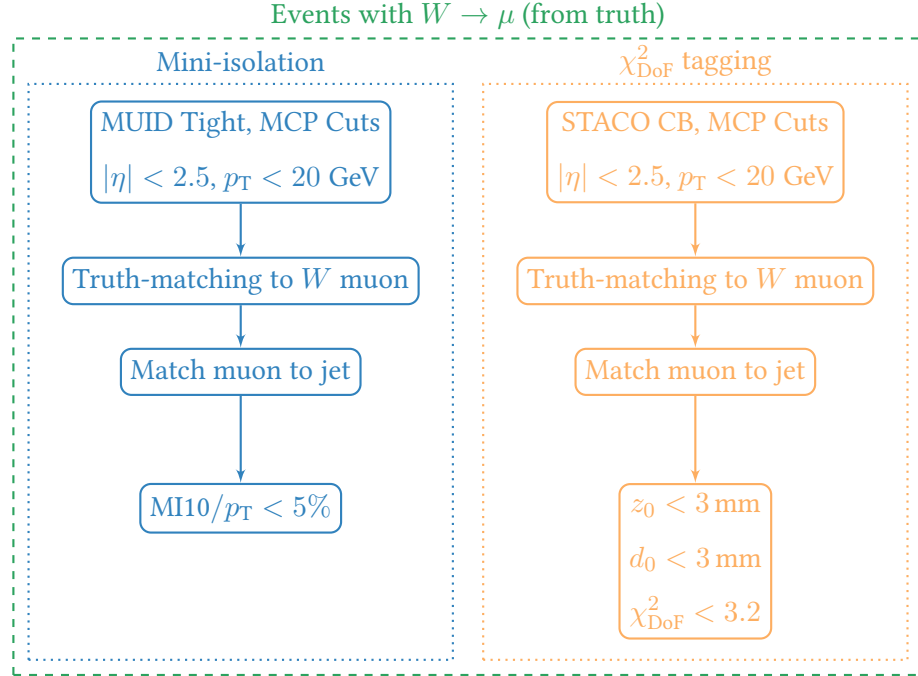


Figure 7.7: Structure of the efficiency measurement including both cutflows.

1670 Next the muons are required to be within $\Delta R < 0.5$ from a jet. The impetus behind the
 1671 analysis is to probe highly boosted events exploiting the capabilities of χ^2_{match} tagging. This
 1672 selection ensures that the muons available for χ^2_{match} tagging are indeed close to a jet. This
 1673 selection also has an efficiency associated with it defined as:

$$\epsilon_{\text{non-iso}} = \frac{\text{Muons with } \Delta R_{\mu}^{\text{jet}} < 0.5}{\text{STACO/MUID muons that pass reconstruction cuts}} \quad (7.3)$$

1674 The final step is the application of either the mini-isolation selection or the χ^2_{match} tagger
 1675 selection discussed above. These selections are associated with the final and most interesting
 1676 sets of efficiencies, defined as:

$$\epsilon_{\chi^2_{\text{match}}/\text{MI10}} = \frac{\text{Muons which pass } \chi^2_{\text{match}}/\text{MI10 selection}}{\text{Muons with } \Delta R_{\mu}^{\text{jet}} < 0.5} \quad (7.4)$$

1677 In the nominal analysis described in [40] muons which are within $\Delta R = 0.1$ of the jet
 1678 would be removed. The goal of the analysis is to exploit the χ^2_{match} tagger to accept additional
 1679 events where the signal muon emerges very close to the jet axis, thus overlap removal ² is not

²True objects may be reconstructed as two different objects, such as an electron and jet. Overlap removal is the

- 1680 traditionally part of the χ^2_{match} tagging selection. Two sets of efficiencies are provided here:
 1681 one without overlap (defined in Eq 7.4) and one with overlap removal, defined below

$$\epsilon_{\chi^2_{\text{match}}/\text{MI10+overlap}} = \frac{\text{Muons which pass the } \chi^2_{\text{match}}/\text{MI10 selection with } \Delta R_{\mu}^{\text{jet}} > 0.1}{\text{Muons with } \Delta R_{\mu}^{\text{jet}} < 0.5} \quad (7.5)$$

1682 7.5 Results

1683 The results of the reconstruction portion of the analysis chains are summarized in Table 7.1 for
 1684 the χ^2_{match} chain and in Table 7.2 for the mini-isolation chain. The matching efficiency (ϵ_{match})
 1685 is stable with respect to Z' mass for both MUID and STACO, meaning that both algorithms
 1686 are able to reconstruct the signal muon irrespective of boost. Within the uncertainty neither
 1687 algorithm appears to be better than other at reconstruction of these muons. The efficiencies
 1688 of both reconstruction selections (ϵ_{reco}) are compatible within uncertainties and appear to be
 1689 slightly lower at low Z' mass, likely due to the p_T requirement on the muon. Finally, the colli-
 1690 mation effect due to increased boost is clearly visible in the non-isolation efficiency. A marked
 1691 increase with Z' mass is noted as the products of the top quarks get pushed closer together.
 1692 Note that the results obtained at $m_{Z'} = 2.5 \text{ TeV}$ suffer from lack of statistics compared to
 1693 the other mass points. Once again, this effect those not appear to affect one reconstruction
 1694 algorithm more than the other and the efficiencies are compatible within uncertainty.

$m_{Z'}$	$N_{\text{muons}}^{\text{STACO}}$	Efficiency [%]		
		$\epsilon_{\text{match}}^{\text{STACO}}$	$\epsilon_{\text{reco}}^{\text{STACO}}$	$\epsilon_{\text{non-iso}}^{\text{STACO}}$
1000	13 722	91.3 ± 0.2	85.5 ± 0.3	20.4 ± 0.4
1300	15 493	92.0 ± 0.2	86.4 ± 0.3	31.8 ± 0.4
1600	13 425	91.9 ± 0.2	87.5 ± 0.3	42.4 ± 0.5
2000	15 260	92.1 ± 0.2	87.9 ± 0.3	51.3 ± 0.5
2500	3308	91.9 ± 0.5	88.1 ± 0.6	57.7 ± 1.0
3000	15 288	91.8 ± 0.2	87.5 ± 0.3	51.4 ± 0.5

Table 7.1: Results of constructing the muon sample used to estimate the efficiency of the χ^2_{match} tagger. Uncertainty is statistical only.

act of selecting the true object from two overlapping reconstructed objects.

$m_{Z'}$	$N_{\text{muons}}^{\text{MUID}}$	Efficiency [%]		
		$\epsilon_{\text{match}}^{\text{MUID}}$	$\epsilon_{\text{reco}}^{\text{MUID}}$	$\epsilon_{\text{non-iso}}^{\text{MUID}}$
1000	13 722	91.7 ± 0.2	86.6 ± 0.3	20.3 ± 0.4
1300	15 493	92.2 ± 0.2	87.6 ± 0.3	31.9 ± 0.4
1600	13 425	92.2 ± 0.2	88.7 ± 0.3	42.2 ± 0.5
2000	15 260	92.5 ± 0.2	88.8 ± 0.3	51.2 ± 0.4
2500	3308	92.2 ± 0.5	89.1 ± 0.7	57.9 ± 0.9
3000	15 288	92.1 ± 0.2	88.5 ± 0.3	51.2 ± 0.4

Table 7.2: Results of constructing the muon sample used to estimate the efficiency of mini-isolation. Uncertainty is statistical only.

1695 The performance of both taggers was studied as a function of the angular separation be-
 1696 tween the muon and the jet (Figure 7.8), and the p_{T} of the muon (Figure 7.9). The χ^2_{match} tagger
 1697 efficiency shows some minor dependence on the angular separation to the jet and as expected
 1698 exhibits a dependence on the p_{T} of the muon. Mini-isolation has a strong dependence on the
 1699 p_{T} of the muon particularly in the low range. The efficiency at high p_{T} plateaus at approxi-
 1700 mately 100 %, due to the mini-isolation cone containing only the muon itself. The decrease in
 1701 efficiency at lower momentum is due to the increase in the cone size and the inclusion of more
 1702 tracks from the nearby jet in the cone. Note that the cone size is larger than the one used for
 1703 the nominal analysis for muons with $p_{\text{T}} < 50$ GeV. The mini-isolation efficiency distribution
 1704 exhibits a strong dependence on $\Delta R_{\mu}^{\text{jet}}$ which varies as a function of top boost in the event.

1705 This effect was stronger during the initial development of the analysis before truth-matching
 1706 was introduced. A possible explanation for the dip was due to the background rejection capa-
 1707 bility of mini-isolation. Muons which are very close to jets most likely come from semileptonic
 1708 decay of b -quarks. These should be rejected as they do not come from the W boson. Despite
 1709 this correction the effect persists. It is possible that the reconstructed muon is being mis-
 1710 matched to the W muon. The matching criteria was tightened to $\Delta R < 0.001$ in an attempt
 1711 to reduce the likelihood of muon mismatching. This had a negligible effect on the shape of the
 1712 MI distribution. As expected changing the value of k_{T} does change the shape of the distribu-
 1713 tion, but does not remove the dip.

1714 An examination of the MI10 cone-size points to the explanation: low- p_{T} muons will result

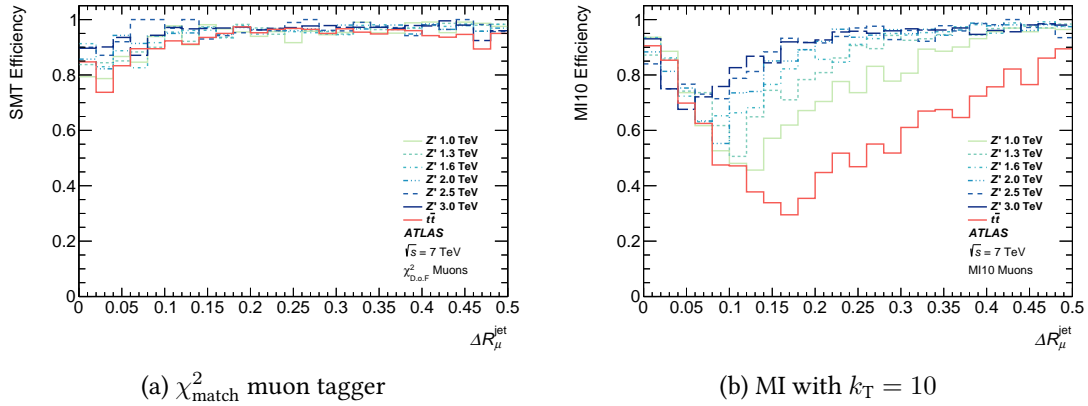


Figure 7.8: Efficiency of MI ($k_T = 10$) and χ^2_{match} tagger as a function of the angular separation between the reconstructed muon and the nearest reconstructed jet. The dip in the MI efficiency at low ΔR is removed in the nominal analysis by cutting at $\Delta R < 0.1$

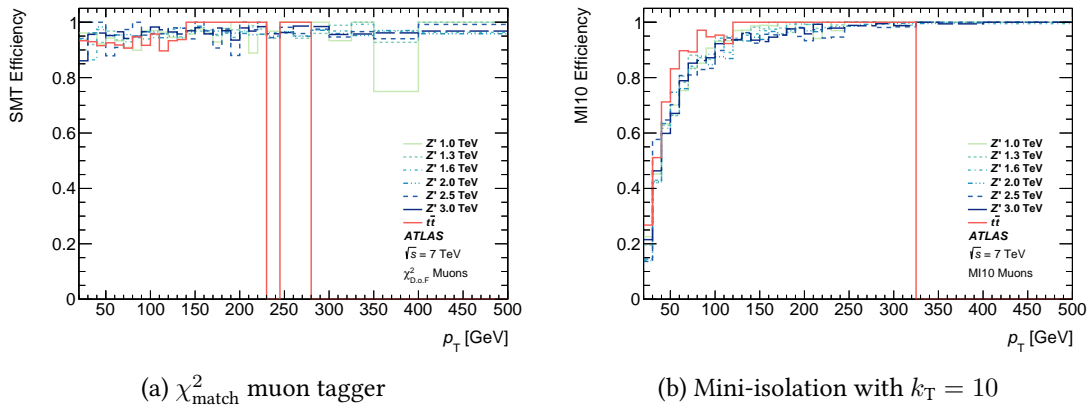


Figure 7.9: Efficiency of mini-isolation ($k_T = 10$) and the χ^2_{match} muon tagger as a function of the transverse momentum of the muon.

1715 in a larger cone with a maximum size of $\Delta R = 0.4$, if these happen to lie near to the jet they
 1716 are very likely to be rejected. The non-resonant $t\bar{t}$ distribution exhibits a wider and lower dip
 1717 in the efficiency. In other words the distance between the jet and the muon do not scale linearly
 1718 with the muon p_T hence at lower boost the jet cone and the muon cone overlap significantly.

1719 The χ^2_{match} tagger efficiency is very high and fairly stable with Z' mass as shown in Ta-
 1720 ble 7.3. The inclusion of the overlap removal decreases the efficiency by approximately 7 %–
 1721 10 % depending on the mass point examined. In comparison, the mini-isolation efficiency is
 1722 lower across the mass range, with and without overlap, but only by 2 %-10 % depending on
 1723 the mass point examined. Crucially, the efficiency of both taggers at higher Z' masses are very
 1724 similar. This means that the gains in acceptance provided by χ^2_{match} is smaller in the $m_{Z'}$ that
 1725 has yet to be experimentally excluded.

$m_{Z'}$ [GeV]	Efficiency [%]			
	$\epsilon_{\chi^2_{\text{match}}}$	ϵ_{MI10}	$\epsilon_{\chi^2_{\text{match}} + \text{overlap}}$	$\epsilon_{\text{MI10+overlap}}$
1000	94.5 ± 0.5	83.1 ± 0.8	80.4 ± 0.8	70.2 ± 1.0
1300	95.7 ± 0.3	89.0 ± 0.5	84.9 ± 0.6	79.4 ± 0.6
1600	95.7 ± 0.3	90.9 ± 0.4	85.8 ± 0.5	82.1 ± 0.6
2000	96.0 ± 0.3	92.0 ± 0.3	87.8 ± 0.4	85.5 ± 0.4
2500	96.2 ± 0.5	92.4 ± 0.7	87.1 ± 0.9	85.1 ± 0.9
3000	96.3 ± 0.2	92.5 ± 0.3	87.6 ± 0.4	85.1 ± 0.4

Table 7.3: Efficiency of selecting a muon by using the χ^2_{match} tagger against MI, includ-
ing the additional acceptance provided by the χ^2_{match} tagger. Uncertainty is statistical
only.

1726 7.5.1 Background

1727 A preliminary examination of the amount of background was performed. This was done on
 1728 the same sample of events but instead of selecting lepton plus jets events, the all-hadronic
 1729 events are used as background. The dominant background for boosted $t\bar{t}$ events is multijet,
 1730 While these events do not perfectly represent the dominant background, namely multijet and
 1731 in particular $b\bar{b}$ production, the lack of any muons from W can provide a suitable preliminary
 1732 substitute.

1733 The lack of an isolation requirement is expected to result in a substantial increase in the
 1734 amount of background selected. Additionally the semileptonic b -decays in $b\bar{b}$ would result in
 1735 muons that the χ^2_{match} tagger will select. The analysis chain described in Section 7.4 is repeated
 1736 on the same sample used however the truth level selection of events with a W muon is reversed,
 1737 thus at truth level both W bosons decay hadronically.

1738 As expected, MI exhibits a low fake rate while maintaining very high signal efficiency (Ta-
 1739 ble 7.4). In comparison, removing the isolation requirement greatly increases the background
 1740 acceptance when using the χ^2_{match} tagger. A full treatment of the background would be required
 1741 to account for the background present.

1742 The increase in signal acceptance does not make this methodology sufficiently advan-
 1743 tageous particularly when considering the large increase in fake rate. An examination of the
 1744 b -tagging potential of the χ^2_{match} tagger is presented in the next section.

$m_{Z'}$ [GeV]	Fake rate [%]		
	$\epsilon_{\chi^2_{\text{match}}}$	ϵ_{MI10}	$\epsilon_{\text{MI10+overlap}}$
1000	92.8	4.10	2.39
1300	92.4	4.77	3.66
1600	91.8	5.46	4.55
2000	91.1	7.07	6.09
2500	90.0	6.40	5.57
3000	90.1	6.59	5.68

Table 7.4: Fake rate of χ^2_{match} tagger, mini-isolation and mini-isolation including overlap removal as measured using all Z' mass points.

1745 7.6 B-tagging potential in boosted events

1746 A study of the b -tagging performance of the SMT tagger was carried out and is presented
 1747 here along with a comparison against the nominal MV1 tagger. The performance is estimated
 1748 in simulation using the Z' samples described earlier. Using truth information, the b -quarks
 1749 from the top decays are identified and then matched to reconstructed anti- k_t jets of cone-size
 1750 $\Delta R = 0.4$. The matching is done by requiring the jet and b -quark lie fairly close to each other
 1751 ($\Delta R_b^{\text{jet}} < 0.3$). These matched jets then tentatively form a pool of jets on which the tagging

$m_{Z'}$ [GeV]	Number of b -quarks from top		$\epsilon_{b \text{ to jet}}$ [%]
	In the event	Matched to a jet	
1000	160 000	133 000	83.5 ± 0.1
1300	180 000	155 000	85.9 ± 0.1
1600	160 000	140 000	87.0 ± 0.1
2000	180 000	158 000	87.9 ± 0.1
2500	40 000	35 200	88.0 ± 0.2
3000	180 000	156 000	86.8 ± 0.1

Table 7.5: Summary of b -quark to jet matching efficiencies for all tested Z' masses. The sample for $m_{Z'} = 2500$ GeV contains a smaller integrated luminosity, than the other samples, hence the lower number of jets.

1752 performance can be measured. This matching procedure has an efficiency associated with it
 1753 defined as

$$\epsilon_{b \text{ to jet}} = \frac{b \text{ quarks with } \Delta R_{\text{jet}}^b < 0.3}{b \text{ quarks from } t \rightarrow Wb} \quad (7.6)$$

1754 The matching efficiency remains above 80 % through-out the tested mass range (Table 7.5),
 1755 and there appears to be a trend of increasing matching efficiency with mass range.

1756 The tagging efficiency can be defined in two ways. The first folds the effect of the low
 1757 $b \rightarrow \mu$ branching-ratio into the final efficiency. This makes the comparison with other taggers
 1758 possible and is denoted by $\epsilon_{\text{Inc. SMT}}$.

1759 The second definition separates the efficiency into two components: firstly, the jet is as-
 1760 sociated with a STACO CB muon by requiring $\Delta R_{\text{jet}}^\mu < 0.5$. The associated efficiency defined
 1761 as,

$$\epsilon_{\mu\text{-match}} = \frac{\text{Number of } b\text{-jets with an associated muon}}{\text{Number of } b\text{-jets}} \quad (7.7)$$

1762 and then both the muon and the jet are required to pass the SMT tagger selection. This step
 1763 has an associated efficiency:

$$\epsilon_{\text{SMT}} = \frac{\text{Number of jets/muons that pass the } \chi^2_{\text{match}} \text{ tagger selection}}{\text{Number of } b\text{-jets with an associated muon}} \quad (7.8)$$

1764 The second definition provides a more apt description of the performance of the SMT tagger
 1765 but makes comparisons with other taggers incorrect. The former definition of the efficiency is

¹⁷⁶⁶ used here to allow for a proper comparison between the MV1 and SMT taggers.

¹⁷⁶⁷ As expected, as the boost increases the distance between the muon and the jet decreases

¹⁷⁶⁸ as shown in Table 7.6. This leads to an increase in the muon-to-jet matching efficiency.

$m_{Z'}$ [GeV]	Jets matched to muon	$\epsilon_{\mu\text{-match}}$ [%]
1000	22 100	17.1 ± 0.3
1300	28 400	18.2 ± 0.2
1600	27 600	20.4 ± 0.2
2000	33 500	20.7 ± 0.2
2500	7540	21.2 ± 0.5
3000	32 800	21.5 ± 0.2

Table 7.6: Results of the muon to jet association in MC simulated inclusive Z' samples.

¹⁷⁶⁹ The tagging yields as well as the overlap yield between the taggers are shown in Ta-
¹⁷⁷⁰ ble 7.7. As expected the MV1 tagger selects the vast majority of the b -jets while the effect
¹⁷⁷¹ of the semileptonic b -decay is also noted in the lower SMT yields.

¹⁷⁷² The SMT tagging efficiency appears to increase with $m_{Z'}$ as shown in Table 7.7. Interest-

¹⁷⁷³ ingly, the performance of the MV1 tagger degrades substantially with increasing $m_{Z'}$ mass.

¹⁷⁷⁴ Also note that the overlap between the MV1 tagger and the SMT tagger decreases with $m_{Z'}$.

¹⁷⁷⁵ This means that using the SMT tagger alongside the MV1 tagger can provide substantial in-

¹⁷⁷⁶ creases in yields at higher Z' masses.

$m_{Z'}$ [GeV]	Number of jets tagged by		
	SMT	MV1	Both
1000	19 600	96 900	14 800
1300	25 000	109 000	18 100
1600	23 900	93 100	16 300
2000	28 300	96 200	17 800
2500	6250	19 800	3690
3000	27 200	89 400	16 200

Table 7.7: Summary of the jet tagging results. The values represent the tagged jets out of the pool of jets matched to b -quarks.

$m_{Z'} [\text{GeV}]$	$\epsilon_{\text{SMT}} [\%]$	$\epsilon_{\text{MV1}} [\%]$	Overlap [%]	Added Acceptance [%]
1000	14.7 ± 0.1	72.7 ± 0.1	75.3	5
1300	16.2 ± 0.1	70.7 ± 0.1	72.4	6
1600	17.2 ± 0.1	66.9 ± 0.1	68.0	8
2000	17.9 ± 0.1	60.9 ± 0.1	63.0	11
2500	17.8 ± 0.2	56.3 ± 0.2	59.0	13
3000	17.4 ± 0.1	57.3 ± 0.1	60.0	12

Table 7.8: Summary of the jet tagging efficiencies. The amount of overlap is shown out of the SMT tagged jets. The added acceptance is the additional number of jets added by using SMT plus MV1 over MV1 only. The uncertainties are statistical only.

1777 The efficiency for both taggers as function of the jet p_T are shown in Figure 7.10. The
 1778 performance of the MV1 tagger is clearly p_T dependant while the SMT tagger is more stable
 1779 with respect to jet p_T

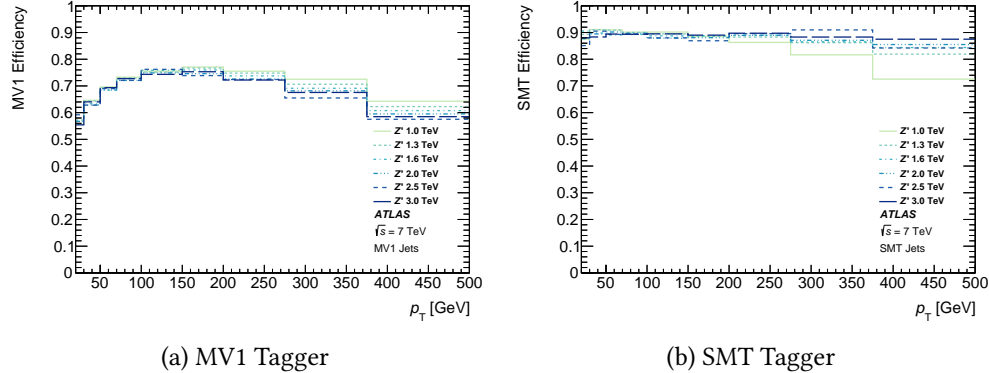


Figure 7.10

1780 In order to truly ascertain the viability of using the SMT tagger in a boosted enviornment
 1781 it is important to conduct a measurement of the fake-rate. As was seen from the calibration
 1782 of the SMT tagger on both 2012 and 2011 data, the efficiency of tagging a soft muon is not
 1783 affected by the isolation of that muon. However additional studies examining the χ^2_{match} SF at
 1784 very-high $E_T^{\text{cone}\Delta R}/p_T^{\text{cone}\Delta R}$ to make sure the SF remain unaffected.

1785 **Chapter 8**

1786 **Conclusions**

Appendices

1787

¹⁷⁸⁸ **Appendix A**

¹⁷⁸⁹ **Electron identification criteria**

¹⁷⁹⁰ Three sets of identification criteria are defined and labelled as loose, medium and tight. The
¹⁷⁹¹ selection criteria include tracking, calorimeter and track-cluster variables as detailed in Ta-
¹⁷⁹² ble A.2.

Category	Description	Variable
Loose		
Acceptance	$ \eta < 2.47$	
Hadronic leakage	In $ \eta < 0.8$ and $ \eta > 1.37$: ratio of E_T in the first layer of the hadronic calorimeter to E_T of the EM cluster	$R_{\text{had},1}$
	In $0.8 < \eta < 1.37$: ratio of E_T in whole hadronic calorimeter to E_T of the EM cluster	R_{had}
Middle layer of the EM	Ratio of energies in 3×7 cells over 7×7 cells	R_η
	Lateral width of the shower	$\omega_{\eta 2}$
Front layer of EM	Total shower width	ω_{stot}
	Energy difference of the largest and second largest energy deposits in the cluster divided by their sum	E_{ratio}
Track quality and track-cluster matching	Number of hits in the pixel detector (> 0)	
	Number of hits in the silicon detectors (≥ 7)	
	$ \Delta\eta $ between the cluster position in the first layer and the extrapolated track (< 0.015)	$\Delta\eta_1$
Medium		
Track quality and track-cluster matching	Number of hits in the b-layer > 0 for $ \eta < 2.01$	
	Number of hits in the pixel detector > 1 for $ \eta < 2.01$	
	Transverse impact parameter $ d_0 < 5$ mm	d_0
	Tighter $ \eta_1 $ cut (< 0.005)	
TRT	Loos cut on TRT high-treshold fraction	
Tight		
Track quality and track-cluster matching	Transverse impact parameter cut $ d_0 < 1$ mm	
	Asymmetric cut on $\Delta\phi$ between the cluster position in the middle layer and the etrapulated track	$\Delta\phi$
	Ratio of the cluster energy to the track momentum	E/p
TRT	Total number of hits in the TRT	
	Tighter cut on the TRT high-threshold fraction	
Conversions	Reject electron candidates matched to reconstructed photon conversions	

Table A.2: caption

1793 **Appendix B**

1794 **Muon identification criteria**

1795 Muon identification criteria are defined for MUID are presented below:

1796 • **Tight:**

- 1797 – Passes MUID Combined selection **OR**
- 1798 – MUID Standalone at $|\eta| > 2.5$ **AND** has atleast three MDT+CSC stations **OR**
- 1799 – MuGirl with extended track **AND** (at least two MDT+CSC stations **OR** less than six MDT+CSC holes on track)

1801 • **Medium:**

- 1802 – Tight **OR**
- 1803 – MuGirl with extended track **OR** $|\eta| < 0.2$ **OR** has at least two muon track segments
1804 **OR**
- 1805 – MuTagIMO at $|\eta| < 0.2$ **OR** has at least two muon track segments

1806 • **Loose:**

- 1807 – Medium **OR**
- 1808 – MuGirl **OR**
- 1809 – MuTagIMO **OR**
- 1810 – MuidStandalone

¹⁸¹¹ **Appendix C**

¹⁸¹² **STACO Combined Covariance**

¹⁸¹³ **Matrix**

1814 **Appendix D**

1815 **List of triggers used in calibration**

1816 The calibration analysis makes use of an OR of the triggers listed below. The triggers fire
1817 based on a set of criteria summarized in the trigger name following the ATLAS trigger nam-
1818 ing convention. The list includes generic single low- p_T muon triggers such as EF_mu6 and
1819 EF_mu15, single high- p_T muons & jets triggers such as EF_mu24_j65_a4tchad and
1820 the specialized J/ψ trigger EF_mu6_Trk_Jpsi_loose.

- 1821 • EF_mu24_j65_a4tchad_EFxe40_tclcw
- 1822 • EF_mu4T_j65_a4tchad_xe60_tclcw_loose
- 1823 • EF_mu24_j65_a4tchad
- 1824 • EF_mu18_tight_e7_medium1
- 1825 • EF_mu4T_j65_a4tchad_xe70_tclcw_veryloose
- 1826 • EF_mu24_j65_a4tchad_EFxe60_tclcw
- 1827 • EF_mu24_tight_b35_mediumEF_j35_a4tchad
- 1828 • EF_mu20i_tight_g5_loose_TauMass
- 1829 • EF_mu6_Trk_Jpsi_loose
- 1830 • EF_mu24i_tight
- 1831 • EF_mu24i_tight_MuonEF

- 1832 • EF_mu24i_tight_MG
- 1833 • EF_mu24i_tight_12muonSA
- 1834 • EF_mu24_tight_3j35_a4tchad
- 1835 • EF_mu24_g20vh_loose
- 1836 • EF_mu40_MSonly_barrel_tight
- 1837 • EF_mu50_MSonly_barrel_tight
- 1838 • EF_mu24_tight_EFxe40
- 1839 • EF_mu24_tight_L2StarB
- 1840 • EF_mu18_medium
- 1841 • EF_mu24_medium
- 1842 • EF_mu24_tight
- 1843 • EF_mu24_tight_MuonEF
- 1844 • EF_mu24_tight_MG
- 1845 • EF_mu24_tight_L2StarC
- 1846 • EF_mu36_tight
- 1847 • EF_mu40_tight
- 1848 • EF_mu20it_tight
- 1849 • EF_mu24_g20vh_medium
- 1850 • EF_mu18_2g10_medium
- 1851 • EF_mu24_muCombTag_NoEF_tight
- 1852 • EF_mu10i_loose_g12Tvh_medium
- 1853 • EF_mu10i_loose_g12Tvh_medium_TauMass

- 1854 • EF_mu18_2g10_loose
- 1855 • EF_mu10i_g10_medium_TauMass
- 1856 • EF_mu20i_tight_g5_medium_TauMass
- 1857 • EF_mu24_tight_3j45_a4tchad
- 1858 • EF_mu24_tight_4j45_a4tchad
- 1859 • EF_mu24_tight_4j35_a4tchad
- 1860 • EF_mu4T
- 1861 • EF_mu6
- 1862 • EF_mu15
- 1863 • EF_mu40_slow_tight
- 1864 • EF_mu60_slow_tight1
- 1865 • EF_mu22_IDTrkNoCut_tight
- 1866 • EF_mu8_4j45_a4tchad_L2FS
- 1867 • EF_mu6_Trk_Jpsi_loose_L2StarB
- 1868 • EF_mu6_Trk_Jpsi_loose_L2StarA
- 1869 • EF_mu24_j65_a4tchad_EFxe40wMu_tclcw
- 1870 • EF_mu24_j65_a4tchad_EFxe60wMu_tclcw
- 1871 • EF_mu6T_2b55_medium_2j55_a4tchad_L1J20_matched
- 1872 • EF_mu24i_tight_muFast
- 1873 • EF_mu4T_L2StarB
- 1874 • EF_mu6_L2StarB
- 1875 • EF_mu15_vbf_L1TAU8_MU10

¹⁸⁷⁶ **Appendix E**

¹⁸⁷⁷ **List of muon combined performance**
¹⁸⁷⁸ **(MCP) cuts**

- ¹⁸⁷⁹ • Require a pixel b-layer hit on the muon EXCEPT where the extrapolated muon track
¹⁸⁸⁰ passed an uninstrumented or dead area of the b-layer.
- ¹⁸⁸¹ • Number of pixel hits + number of crossed dead pixel sensors > 0.
- ¹⁸⁸² • Number of SCT hits + number of crossed dead SCT sensors > 4.
- ¹⁸⁸³ • Number of pixel holes + number of SCT holes < 3.
- ¹⁸⁸⁴ • A successful TRT extension where expected (i.e. in the η acceptance of the TRT). An
¹⁸⁸⁵ unsuccessful extension corresponds to either no TRT hit associated, or a set of TRT
¹⁸⁸⁶ hits associated as outliers. Let $N_{\text{TRT hits}}$ denote the number of TRT hits on the muon
¹⁸⁸⁷ track, $N_{\text{TRT outliers}}$ the number of TRT outliers on the muon track, and $n = N_{\text{TRT hits}} +$
¹⁸⁸⁸ $N_{\text{TRT outliers}}$:
 - ¹⁸⁸⁹ – **Case 1:** $0.1 < |\eta| < 1.9$. Require $n > 5$ and $N_{\text{TRT outliers}} < 0.9n$.
 - ¹⁸⁹⁰ – **Case 2:** $|\eta| \geq 0.1$ or $|\eta| \leq 1.9$. If $n > 5$, then require $N_{\text{TRT outliers}} < 0.9n$.

¹⁸⁹¹ **Appendix F**

¹⁸⁹² **STACO CB reconstruction efficiency**

¹⁸⁹³ Bibliography

- ¹⁸⁹⁴ [1] Luminosity Public Result. <https://twiki.cern.ch/twiki/bin/view/AtlasPublic/LuminosityPublicResults>. Accessed: 2014-06-20.
- ¹⁸⁹⁵
- ¹⁸⁹⁶ [2] ATLAS Collaboration. The ATLAS experiment at the CERN Large Hadron Collider. *Journal of Instrumentation*, 3(08):S08003, 2008.
- ¹⁸⁹⁷
- ¹⁸⁹⁸ [3] A. Schaelicke, T. Gleisberg, S. Hoeche, S. Schumann, J. Winter, F. Krauss, and G. Soff. Event generator for particle production in high-energy collisions. *Progress in Particle and Nuclear Physics*, 53(1):329–338, 2004.
- ¹⁸⁹⁹
- ¹⁹⁰⁰
- ¹⁹⁰¹ [4] ATLAS Collaboration. Commissioning of the ATLAS high-performance b -tagging algorithms in the 7 TeV collision data, Jul 2011.
- ¹⁹⁰²
- ¹⁹⁰³ [5]
- ¹⁹⁰⁴
- ¹⁹⁰⁵ [6] J Blanco, V Boisvert, L Cerrito, N Cooper-Smith, J D Morris, M Rose, G Salamanna, G Snidero, and M Vanadia. Measurement of the top quark pair production cross-section with ATLAS in pp collisions at $\sqrt{s} = 7$ TeV in the single-lepton channel using semileptonic b decays, Mar 2012.
- ¹⁹⁰⁶
- ¹⁹⁰⁷
- ¹⁹⁰⁸ [7] Particle Data Group, J. Beringer, et al. The Review of Particle Physics. *Physical Review D*, 86:010001+, 2012.
- ¹⁹⁰⁹
- ¹⁹¹⁰ [8] Nikolaos Kidonakis. NNLL threshold resummation for top-pair and single-top production. 2012.
- ¹⁹¹¹
- ¹⁹¹² [9] Michał Czakon, Paul Fiedler, and Alexander Mitov. Total top-quark pair-production cross section at hadron colliders through $O(\alpha_S^4)$. *Phys.Rev.Lett.*, 110(25):252004, 2013.
- ¹⁹¹³

- 1914 [10] Blanco, J and Boisvert, V and Cerrito, L and Cooper-Smith, N and Morris, J D and Rose,
 1915 M and Salamanna, G and Snidero, G and Vanadia, M. Calibration of the χ^2_{match} -based
 1916 Soft Muon Tagger algorithm, Jan 2012.
- 1917 [11] B. Odom, D. Hanneke, B. D'Urso, and G. Gabrielse. New Measurement of the Electron
 1918 Magnetic Moment Using a One-Electron Quantum Cyclotron. *Physical Review Letters*,
 1919 97:030801, Jul 2006.
- 1920 [12] ATLAS Collaboration. Observation of a new particle in the search for the Standard Model
 1921 Higgs boson with the ATLAS detector at the LHC. *Physics Letters B*, 716(1):1 – 29, 2012.
- 1922 [13] Serguei Chatrchyan et al. Observation of a new boson at a mass of 125 GeV with the CMS
 1923 experiment at the LHC. *Phys.Lett.*, B716:30–61, 2012.
- 1924 [14] P.A.R. Ade et al. Planck 2013 results. I. Overview of products and scientific results. 2013.
- 1925 [15] D.H. Perkins. *Introduction to High Energy Physics*. Cambridge University Pres, 2000.
- 1926 [16] D. Griffiths. *Introcution to Elementary Particles*. John Wiley & Sons, Inc, 1987.
- 1927 [17] N. Cabibbo. Unitary Symmetry and Leptonic Decays. *Physical Review Letters*, 10:531–533,
 1928 Jun 1963.
- 1929 [18] M. Kobayashi and Toshihide Maskawa. CP-Violation in the Renormalizable Theory of
 1930 Weak Interaction. *Progress of Theoretical Physics*, 49(2):652–657, 1973.
- 1931 [19] Ling-Lie Chau and Wai-Yee Keung. Comments on the parametrization of the kobayashi-
 1932 maskawa matrix. *Phys.Rev.Lett.*, 53:1802, 1984.
- 1933 [20] Lincoln Wolfenstein. Parametrization of the Kobayashi-Maskawa Matrix. *Physical Review
 1934 Letters*, 51:1945–1947, Nov 1983.
- 1935 [21] K. Marathe. *Topics in Physical Mathematics*. Springer, 2010.
- 1936 [22] J. J. Aubert, U. Becker, P. J. Biggs, J. Burger, M. Chen, G. Everhart, P. Goldhagen, J. Leong,
 1937 T. McCorriston, T. G. Rhoades, M. Rohde, Samuel C. C. Ting, Sau Lan Wu, and Y. Y. Lee.
 1938 Experimental observation of a heavy particle j. *Physical Review Letters*, 33(23):1404–1406,
 1939 1974.

- 1940 [23] J. H. Christenson, J. W. Cronin, V. L. Fitch, and R. Turlay. Evidence for the 2π decay of
1941 the K^{*0} meson. *Physical Review Letters*, 13(4):138–140, 1964.
- 1942 [24] Steven Weinberg. A model of leptons. *Physical Review Letters*, 19(21):1264–1266, 1967.
- 1943 [25] Sheldon L. Glashow. Partial-symmetries of weak interactions. *Nuclear Physics*, 22(4):579
1944 – 588, 1961.
- 1945 [26] Abdus Salam. Weak and Electromagnetic Interactions. *Conf.Proc.*, C680519:367–377, 1968.
- 1946 [27] G. Arnison et al. Experimental observation of isolated large transverse energy electrons
1947 with associated missing energy at $\sqrt{s} = 540 \text{ GeV}$. *Physics Letters B*, 122(1):103 – 116,
1948 1983.
- 1949 [28] S. W. Herb, D. C. Hom, L. M. Lederman, J. C. Sens, H. D. Snyder, J. K. Yoh, J. A. Appel,
1950 B. C. Brown, C. N. Brown, W. R. Innes, K. Ueno, T. Yamanouchi, A. S. Ito, H. Jostlein, D. M.
1951 Kaplan, and R. D. Kephart. Observation of a Dimuon Resonance at 9.5 GeV in 400 GeV
1952 Proton-Nucleus Collisions. *Physical Review Letters*, 39:252–255, Aug 1977.
- 1953 [29] CDF Collaboration. Observation of Top Quark Production in $p\bar{p}$ Collisions with the Col-
1954 lider Detector at Fermilab. *Physical Review Letters*, 74:2626–2631, Apr 1995.
- 1955 [30] D0 Collaboration. Search for High Mass Top Quark Production in $p\bar{p}$ Collisions at $\sqrt{s} =$
1956 1.8 TeV. *Physical Review Letters*, 74:2422–2426, Mar 1995.
- 1957 [31] ATLAS Collaboration. Search for top pair candidate events in ATLAS at $\sqrt{s}=7 \text{ TeV}$, Jul
1958 2010.
- 1959 [32] CMS Collaboration. Selection of top-like events in the dilepton and lepton-plus-Jets chan-
1960 nels in early 7 TeV Data, 2010.
- 1961 [33] Johann H. Kuhn, A. Reiter, and Peter M. Zerwas. Z Decays to Top Quarks. *Nuclear Physics*,
1962 B272:560, 1986.
- 1963 [34] M. Aliev, H. Lacker, U. Langenfeld, S. Moch, P. Uwer, et al. HATHOR: HAdronic Top and
1964 Heavy quarks crOss section calculatoR. *Comput.Phys.Commun.*, 182:1034–1046, 2011.

- 1965 [35] Matteo Cacciari, Michal Czakon, Michelangelo L. Mangano, Alexander Mitov, and Paolo
 1966 Nason. Top-pair production at hadron colliders with next-to-next-to-leading logarithmic
 1967 soft-gluon resummation. *arXiv:1111.5869 [hep-ph]*, 2011.
- 1968 [36] Combination of ATLAS and CMS results on the mass of the top-quark using up to 4.9 fb^{-1}
 1969 of $\sqrt{s} = 7 \text{ TeV}$ LHC data, Sep 2013.
- 1970 [37] O.W. Greenberg. CPT violation implies violation of Lorentz invariance. *Phys.Rev.Lett.*,
 1971 89:231602, 2002.
- 1972 [38] ATLAS Collaboration. Measurement of the mass difference between top and anti-top
 1973 quarks in pp collisions at $\sqrt{s} = 7 \text{ TeV}$ using the ATLAS detector. *Phys.Lett.*, B728:363–
 1974 379, 2014.
- 1975 [39] CMS Collaboration. Measurement of the mass difference between top and antitop quarks.
 1976 *JHEP*, 1206:109, 2012.
- 1977 [40] ATLAS Collaboration. Search for $t\bar{t}$ resonances in the lepton plus jets final state with
 1978 ATLAS using 4.7 fb^{-1} of pp collisions at $\sqrt{s} = 7 \text{ TeV}$. *Physical Reviews D*, D88(1):012004,
 1979 2013.
- 1980 [41] Lyndon Evans and Philip Bryant. Lhc. *Journal of Instrumentation*, (08):S08001.
- 1981 [42] The ATLAS Collaboration. Luminosity determination in pp collisions at $\text{sqrt}(s)=7 \text{ tev}$
 1982 using the atlas detector at the lhc. *The European Physical Journal C*, 71(4), 2011.
- 1983 [43] ATLAS detector and physics performance: Technical Design Report, 1, 1999.
- 1984 [44] M. Aharrouche and ATLAS Electromagnetic Barrel Calorimeter Collaboration. Energy
 1985 linearity and resolution of the atlas electromagnetic barrel calorimeter in an electron
 1986 test-beam. *Nuclear Instruments and Methods in Physics Research Section A: Accelerators,*
 1987 *Spectrometers, Detectors and Associated Equipment*, 568(2):601–623, 2006.
- 1988 [45] M. A. Dobbs, S. Frixione, E. Laenen, K. Tollefson, H. Baer, E. Boos, B. Cox, R. Engel,
 1989 W. Giele, J. Huston, S. Ilyin, B. Kersevan, F. Krauss, Y. Kurihara, L. Lonnblad, F. Maltoni,

- 1990 M. Mangano, S. Odaka, P. Richardson, A. Ryd, T. Sjostrand, P. Skands, Z. Was, B. R. Webber, and D. Zeppenfeld. Les houches guidebook to monte carlo generators for hadron collider physics. *arXiv:hep-ph/0403045*, 2004.
- 1993 [46] S. Agostinelli, J. Allison, K. Amako, et al. GEANT4—a simulation toolkit. *Nuclear Instruments and Methods in Physics Research Section A: Accelerators, Spectrometers, Detectors and Associated Equipment*, 506(3):250 – 303, 2003.
- 1996 [47] ATLAS Collaboration. Electron reconstruction and identification efficiency measurements with the ATLAS detector using the 2011 LHC proton-proton collision data. 2014.
- 1998 [48] Electron efficiency measurements with the ATLAS detector using the 2012 LHC proton-proton collision data, Jun 2014.
- 2000 [49] B Resende. Muon identification algorithms in ATLAS, Sep 2009.
- 2001 [50] R Nicolaïdou, L Chevalier, S Hassani, J F Laporte, E Le Menedeu, and A Ouraou. Muon identification procedure for the ATLAS detector at the LHC using Muonboy reconstruction package and tests of its performance using cosmic rays and single beam data. *Journal of Physics: Conference Series*, 219(3):032052, 2010.
- 2005 [51] Matteo Cacciari, Gavin P. Salam, and Gregory Soyez. The Anti-k(t) jet clustering algorithm. *JHEP*, 0804:063, 2008.
- 2007 [52] Wahid Bhimji, Andy Buckley, Philip Clark, Robert Harrington, Victoria Martin, and ATLAS Collaboration. Jet energy measurement with the ATLAS detector in proton-proton collisions at $\sqrt{s} = 7$ TeV. *The European Physical Journal C - Particles and Fields*, C73:2304, 2013. CERN-PH-EP-2011-191.
- 2011 [53] ATLAS Collaboration. Jet energy measurement and its systematic uncertainty in proton-proton collisions at $\sqrt{s} = 7$ TeV with the ATLAS detector. 2014.
- 2013 [54] ATLAS Collaboration. Performance of the ATLAS Secondary Vertex *b*-tagging Algorithm in 7 TeV Collision Data, Jul 2010.
- 2015 [55] ATLAS Collaboration. Measurement of the Mistag Rate with 5 fb^{-1} of data collected by the ATLAS Detector, Mar 2012.

- 2017 [56] Matthew Rose. *Development of a new Soft Muon Tagger for the Identification of b quarks, applied to a Top Quark Pair Production Cross Section Measurement, using the ATLAS Detector at CERN*. PhD thesis, Royal Holloway, University of London, 2013.
- 2018
2019
- 2020 [57] Stefano Frixione and Bryan R. Webber. Matching NLO QCD computations and parton shower simulations. *JHEP*, 0206:029, 2002.
- 2021
- 2022 [58] Stefano Frixione, Paolo Nason, and Bryan R. Webber. Matching NLO QCD and parton showers in heavy flavor production. *JHEP*, 0308:007, 2003.
- 2023
- 2024 [59] G. Corcella, I. G. Knowles, G. Marchesini, S. Moretti, K. Odagiri, P. Richardson, M. H. Seymour, and B. R. Webber. Herwig 6.5: an event generator for hadron emission reactions with interfering gluons (including supersymmetric processes). *Journal of High Energy Physics*, 2001(01):010–010, 2001.
- 2025
2026
2027
- 2028 [60] J.M. Butterworth, Jeffrey R. Forshaw, and M.H. Seymour. Multiparton interactions in photoproduction at HERA. *Z.Phys.*, C72:637–646, 1996.
- 2029
- 2030 [61] Michelangelo L. Mangano, Fulvio Piccinini, Antonio D. Polosa, Mauro Moretti, and Roberto Pittau. ALPGEN, a generator for hard multiparton processes in hadronic collisions. *Journal of High Energy Physics*, 2003(07):001, 2003.
- 2031
2032
- 2033 [62] Borut Paul Kersevan and Elzbieta Richter-Was. The Monte Carlo event generator AcerMC versions 2.0 to 3.8 with interfaces to PYTHIA 6.4, HERWIG 6.5 and ARIADNE 4.1. *Comput.Phys.Commun.*, 184:919–985, 2013.
- 2034
2035
- 2036 [63] Torbjorn Sjostrand, Stephen Mrenna, and Peter Skands. Pythia 6.4 physics and manual. *Journal of High Energy Physics*, 2006(05):026–026, 2006.
- 2037
- 2038 [64] Background studies for top-pair production in lepton plus jets final states in $\sqrt{s} = 7\text{TeV}$ ATLAS data, 2010.
- 2039
- 2040 [65] ATLAS Collaboration. Measurement of the charge asymmetry in top quark pair production in pp collisions at $\text{sqrt}(s) = 7 \text{ tev}$ using the atlas detector. *The European Physical Journal C*, 72(6), 2012.
- 2041
2042
- 2043 [66]

- 2044 [67] ATLAS Collaboration. Measurement of the top quark pair production cross-section with
2045 ATLAS in the single lepton channel. *Physics Letters B*, 711(3–4):244 – 263, 2012.
- 2046 [68] A search for $t\bar{t}$ resonances in the lepton plus jets final state with ATLAS using 14 fb^{-1} of
2047 pp collisions at $\sqrt{s} = 8\text{ TeV}$, May 2013. Not published in the proceedings.
- 2048 [69] Serguei Chatrchyan et al. Search for Z' resonances decaying to $t\bar{t}$ in dilepton+jets final
2049 states in pp collisions at $\sqrt{s} = 7\text{ TeV}$. *Phys.Rev.*, D87:072002, 2013.
- 2050 [70] Serguei Chatrchyan et al. Search for anomalous $t\bar{t}$ production in the highly-boosted all-
2051 hadronic final state. *JHEP*, 1209:029, 2012.
- 2052 [71] CMS Collaboration. Search for $t\bar{t}$ resonances in semileptonic final state, 2013.
- 2053 [72] J. Pumplin, D.R. Stump, J. Huston, H.L. Lai, Pavel M. Nadolsky, et al. New generation of
2054 parton distributions with uncertainties from global QCD analysis. *JHEP*, 0207:012, 2002.

2055 Todo list

2056	Described the radiative corrections to higgs mass and the hierarchy problem.	20
2057	Add plot of pt for SMT muon and W muons	75
2058	Talk about other possible models	132